HUGHES

ELECTRON DYNAMICS DIVISION

FINAL REPORT

HIGH EFFICIENCY TRAVELING WAVE TUBE DEVELOPMENT FOR SPACE COMMUNICATIONS

PREPARED FOR

NATIONAL AERONAUTICS AND SPACE ADMINISTRATION
LEWIS RESEARCH CENTER
21000 BROOKPARK ROAD
CLEVELAND, OH 44135

CONTRACT NO. NAS 3-24897

FINAL REPORT

HIGH EFFICIENCY 20 GHz TRAVELING WAVE TUBE DEVELOPMENT FOR SPACE COMMUNICATIONS

PREPARED FOR

NATIONAL AERONAUTICS AND SPACE ADMINISTRATION
LEWIS RESEARCH CENTER
21000 BROOKPARK ROAD
CLEVELAND, OH 44135

NASA CR-187160
CONTRACT NO. NAS 3-24897

OCTOBER 1991

HUGHES AIRCRAFT COMPANY
ELECTRON DYNAMICS DIVISION
3100 WEST LOMITA BOULEVARD
P.O. BOX 2999
TORRANCE, CA 90509-2999

TABLE OF CONTENTS

LIST OF ILLUSTRATIONS

LIST OF ILLUSTRATIONS (CONTINUED)

LIST OF TABLES

1.0 PROGRAM OVERVIEW

1.1 INTRODUCTION

The primary objective of this multiyear effort was to develop and demonstrate a 75 watt, 20 GHz, high efficiency traveling wave tube (TWT). A secondary objective was to accomplish this by incorporating all of the latest technology for improving efficiency into a single TWT design. Key efficiency enhancement features were: a diamond supported helix, a helix dynamic velocity taper, and a multistage textured graphite collector. Since the TWT was developed for satellite communication systems, high reliability and long life were also priority considerations in the tube design. The TWT developed on this program is Hughes model 953H.

The baseline for the 953H was the 918HA TWT, developed under NASA contract number NAS 3-23345. The 918HA produced 70 watts of output power with 48 percent overall efficiency at 20 GHz. An efficiency of 48 percent is remarkable at K-band frequencies, but incorporating the latest efficiency enhancement features, the 953H TWT attained a new efficiency benchmark of 54.6 percent.

1.2 PROGRAM GOALS

The key goals of the program were:

a. Produce 75 watts output from 17.7 to 20.2 GHz.

b. Demonstrate 60 percent overall efficiency.

c. Develop a diamond supported helix circuit with good electrical/thermal characteristics.

d. Incorporate a dynamic velocity tapered output circuit pitch for efficiency enhancement.

e. Incorporate a multistage depressed collector with textured graphite stages for efficiency enhancement.

f. Fabricate and test two proof-of-concept TWTs.

1.3 PROGRAM ACCOMPLISHMENTS

Major accomplishments on the program were the following:

a. The 953H TWT demonstrated over 75 watts of CW power from 17.7 to 20.2 GHz.

b. Measured an overall efficiency of 54.6 percent, which is a new high at this frequency range.

c. Developed a low-loss diamond circuit with excellent thermal capabilities. The diamond circuit assembly implements a newly developed cold compression technique[1] which eliminates high temperature diamond contamination. A diamond circuit fabricated with this new technique measured a circuit loss of approximately 0.2 dB/inch, several times lower than a typical helix circuit.

d. Developed and implemented a technique of thermally testing the diamond circuit using a wire cathode in the center of the helix. Results of test circuits showed the diamond circuit assembly had excellent thermal transfer characteristics. TWTs incorporating diamond circuits confirmed the above by producing power outputs in excess of 100 watts CW with no signs of degradation or RF power fade.

e. Successfully incorporated a dynamic velocity tapered (DVT) helix in the output circuit section of the TWT. This technique increases the beam conversion efficiency by maintaining synchronization of the circuit phase velocity with the beam velocity.

f. Designed and fabricated a four-stage collector with textured graphite electrodes. The first three stages sort and collect the spent electron beam while the fourth stage is a collector spike which operates at cathode potential. Its primary function is to improve electron collection of the other electrodes. Textured graphite improve the collector efficiency by reducing secondary electrons.

g. Fabricated and tested three proof-of-concept TWTs. The first tube demonstrated diamond circuit assembly feasibility and power handling capability. The second tube demonstrated the 54.6 percent overall efficiency with 100 watts at RF power. Improved beam conversion efficiency by a refined DVT helix was demonstrated by the third tube, however, a shorted collector stage sacrificed the tube's overall efficiency performance.

---

1. Hughes patented.

2.0 DIAMOND ROD TECHNOLOGY

2.1 INTRODUCTION

In a helix type TWT, dielectric material is used to support the helix and provide a thermal path from the helix to the barrel. The dielectric support material, however, undesirably alters the electric field pattern of the RF wave on the helix, reducing the field strength inside the helix where the electron beam-wave interaction takes place. Thus, to optimize the beam-to-RF conversion efficiency, it is most desirable to use a low dielectric constant material and a minimum amount of material to support the helix.

Diamond is an attractive helix support material due to its low dielectric constant, high compressive strength, and high thermal conductivity. Because of these features, it is possible to fabricate a very thin diamond support rod for the helix which is one-half the cross sectional thickness of other dielectric support material such as, boron nitride or beryllia oxide. Diamond support rods as thin as 0.005 inches have been successfully fabricated and tested in tubes. The thin diamond support rod has resulted in considerably reduced dielectric loading and improved beam-to-RF conversion efficiency.

Test measurements and comparison of dielectric loading and cold loss were made on two similar helix circuits, one supported by 0.005 inch wide diamonds and the other supported by 0.020 inch wide beryllia. The significantly lower dielectric loading of the diamond supported circuit, measured from 17 to 22 GHz, can be seen on the normalized phase velocity curve shown in Figure 2-1. Referring to the figure, a dielectric loading factor (DLF) of 1.0 represents the absolute minimum circuit loading. The diamond supported helix has a DLF of 0.85 in comparison to a value of 0.73 for the beryllia supported helix. Thus, the diamond supported helix, in comparison to the beryllia supported helix, will have much higher interaction impedances.

In addition to the significantly lower dielectric loading of the diamond supported helix, circuit cold loss comparisons for this circuit are shown in Figure 2-2. In this figure, signal strength as a function of distance are shown. This measurement was performed by inserting and then slowly withdrawing a coaxial probe through the center of the helix. The relative power coupled to the probe was measured and recorded as a function of helix length. In the top of the figure is the data for the diamond supported circuit and on the bottom is the one for the beryllia supported helix. At a frequency of 20 GHz, the diamond supported helix circuit measured losses of 0.2 dB/in; substantially less than the beryllia circuit at 1.5 dB/in.

2.2 PAST EXPERIENCE

On a past TWT development program, NASA Contract No. NAS3-23345, the gem quality (Type II.A.) diamonds were manufactured into 0.010 inch wide rectangular segments with a

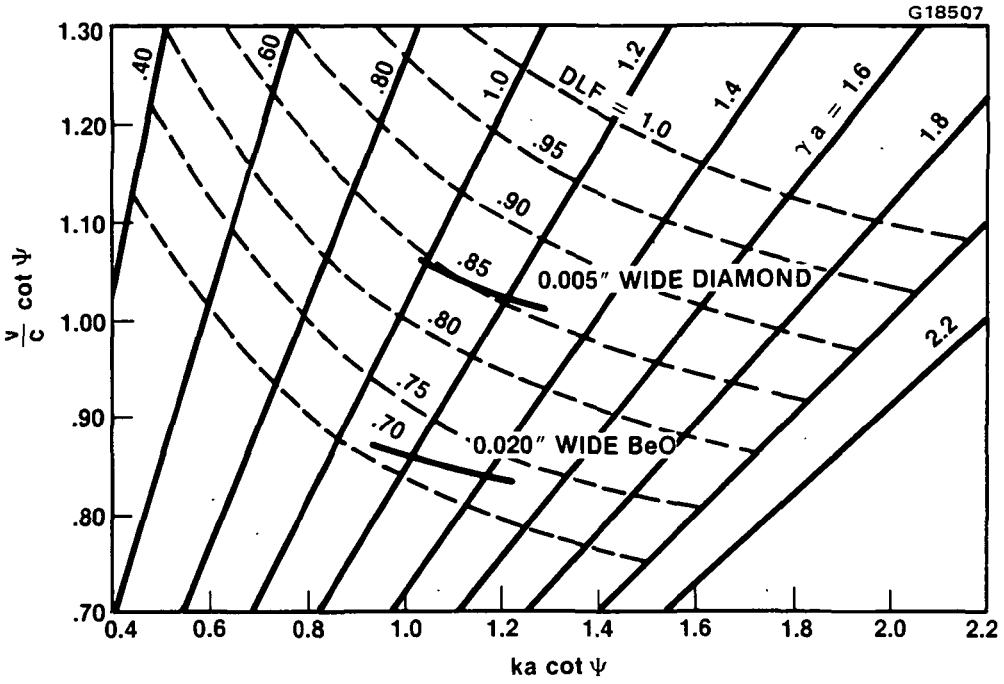

Figure 2-1 Normalized phase velocity curves comparing helices supported by 0.005" wide diamond and 0.020" wide beryllia.

height of 0.030 inches, and lengths that varied from 0.120 to 0.200 inches. These diamond segments were fabricated into a 3-inch long composite rod by diffusion bonding the diamonds to a molybdenum backing strip using a zirconium-copper alloy strip sandwiched in between. High pressures were required during bonding, which was performed above 700°C in an inert atmosphere. The molybdenum strip provided the stiff mechanical support needed to hold the 15 to 20 diamond segments in a continuous line, simulating a long thin diamond rod. Figure 2-3 shows the diamond supported helix assembly with the diamond segments bonded to the molybdenum backing strip. Three of these composite diamond rods were used to support the helix and a heat-shrink technique was used to expand and contract the barrel, clamping the helix and rod assembly in place.

A disadvantage of this technique is that fabrication occurs at temperatures where amorphous carbon forms on the diamond surfaces if exposed to a reactive atmosphere. Since carbon is lossy and undesirable in the circuit output gain section, extreme care must be taken to keep the bonding environment clean and free of active elements. The process, therefore, is complex and costly.

Another problem with this diamond rod fabrication technique is that the helix circuit was thermally limited in power handling capability. A tube incorporating the composite diamond

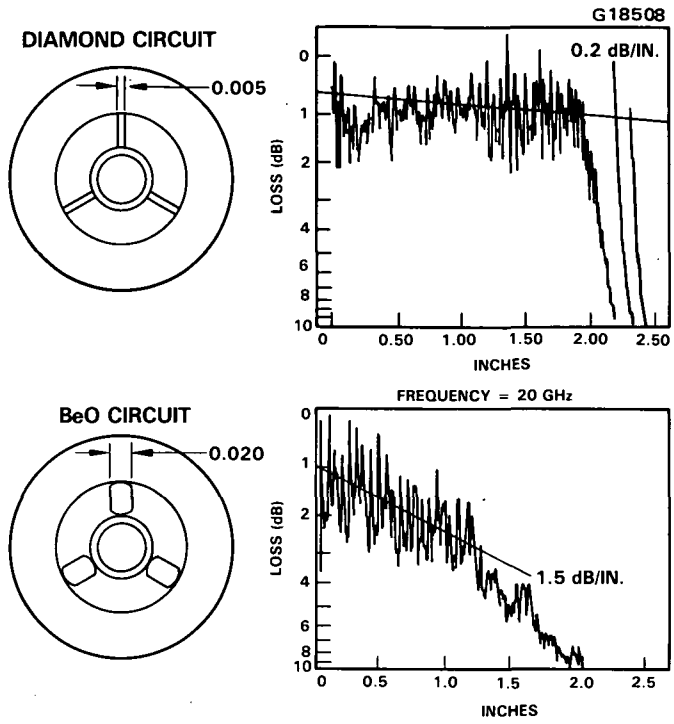

Figure 2-2 Circuit cold loss measurements on the diamond and beryllia supported helix circuits.

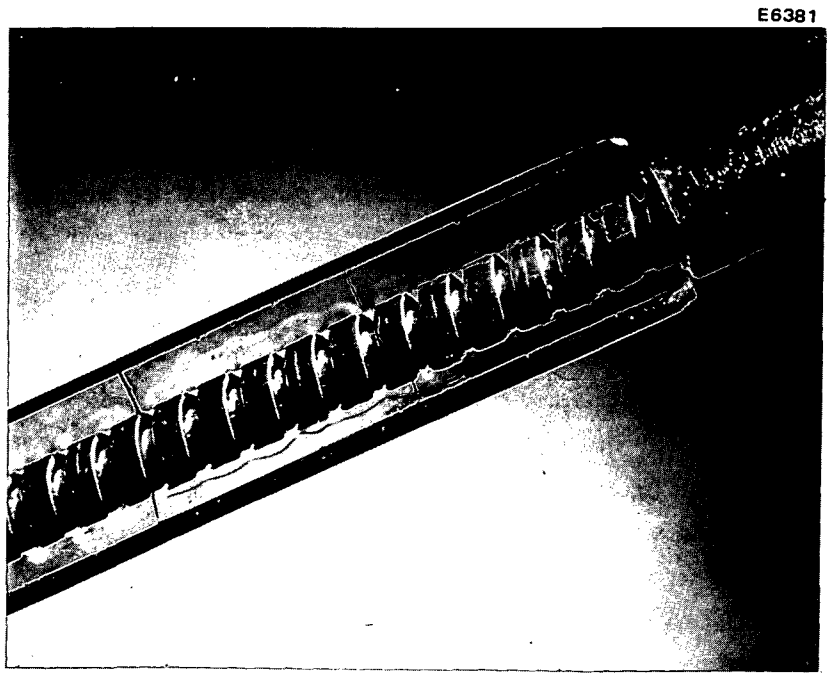

Figure 2-3 Diamond supported helix assembly using old fabrication technique.

rods was fabricated and tested. An improvement in circuit efficiency was demonstrated due to the reduced dielectric loading of diamonds. However, at RF output levels of about 40 watts, a power fade or decrease in power occurred due to overheating of the output circuit. Analysis and tests later indicated that the zirconium copper alloy strip that was used to diffusion bond the diamonds and molybdenum strip, plastically deformed during high power operation. Consequently, the thermal interfaces between the helix and diamond support rods degraded causing the power fade.

2.3 NEW METHODS

The diamonds used in this program are 0.005 inches thick and 0.030 inches high. Such small, translucent parts are difficult to work with. However, a technique has been developed at Hughes Aircraft Company that facilitates circuit manufacturing and resolves problems experienced in the past. The technique consists of a special fixture that holds the diamond segments in place and allows the diamonds to be glued directly onto the helix, eliminating the need for a metal backing strip.

This holding fixture was not only used for the assembly of diamonds onto the helix, but also for the formation of loss patterns on the diamond rods. These low reflection loss patterns isolate the input and output gain sections and are needed for TWT stability. Usually pyrolytic carbon is deposited on helix support rods, but due to the high temperatures involved, titanium carbide (TiC) was selected as the lossy material. TiC was deposited with an automated magnetron system at very low temperatures while a metal mask was placed over the diamonds to achieve the desired loss pattern.

Once the attenuation patterns were sputtered and measured, three diamond rods were glued onto the helix with lucite. After curing, the metal holding fixture was removed and the helix and diamond rod assembly was placed in a copper sleeve as shown in Figure 2-4. Note that the metal strip found in Figure 2-3 has been eliminated.

The diamond circuit assembly implements a newly developed cold compression technique which eliminates heat shrinking and the high temperatures associated with that process. This cold compression technique encapsulates the helix and diamond support assembly firmly in place with great pressure on all interfaces. The pressure applied can be precision controlled and the technique is amenable to very small helix circuits which operate up to 60 GHz. Cold compression offers several other advantages but the most significant advantage is that the entire process is performed at room temperature; eliminating the chances of carbon contamination from either lucite or diamond carburization.

After the process of cold compression is complete, the lucite holding the diamond segments to the helix is chemically removed. Figure 2-5 shows the cross section of the diamond

E6382

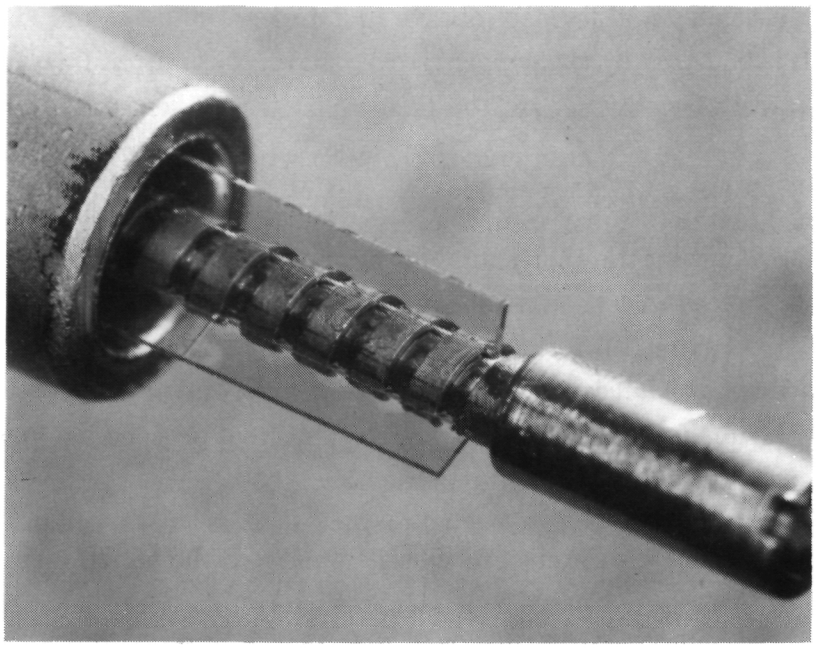

Figure 2-4 Diamond supported helix assembly using new fabrication technique.

E6383

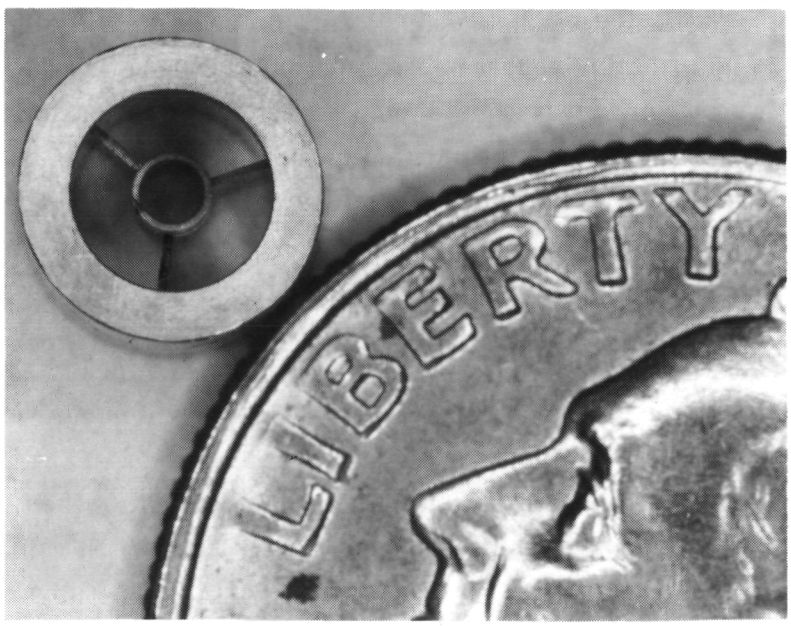

Figure 2-5 Cross section of diamond supported helix assembly.

supported helix assembly and its size relative to a dime. The helix and diamond rod assembly which is enclosed by the copper sleeve is then press fitted into a precision honed integral PPM barrel assembly.

2.4 CIRCUIT THERMAL TESTER

A technique for evaluating the thermal handling capability of the RF circuit mechanical assembly was integrated into the breadboard development efforts. This experimental technique simulates actual TWT operating conditions by heating the helix structure via electron bombardment. The circuit thermal testing was done in parallel and entirely independent of the analytical effort, allowing evaluation of prospective mechanical designs without constructing a complete vacuum assembly.

Construction of the thermal test circuits closely simulated the actual circuit mechanical configuration. All subsequent processing steps which could affect the circuit mechanical properties of an actual TWT such as a 500°C bakeout exhaust were also included in the thermal test circuit fabrication process. In the experiment, the RF structure is heated by electrons emitted off an oxide coated wire cathode. The helix temperatures are derived by measuring the voltage drop across the helix and calculating the resistivity. The test configuration is shown on Figure 2-6. Under full power operation, the TWT is expected to generate 7.5 watts (27 W/in) of thermal power over the last quarter inch of the helix. This dissipated power represents both RF losses and helix interception of the electron beam. Temperature measurements were recorded at various input power levels with the baseplate mounting cradle maintained at a constant 50°C. After a peak input power level was reached (i.e., 30 W/in), a 16 hour minimum thermal soak period followed. The entire circuit was then cycled down to the constant baseplate temperature of 50°C. The procedure was repeated and helix temperatures were compared to the previous values. An increase in the helix temperature deviating from prior results indicated degrading thermal interfaces within the helix structure. If the helix temperature maintained consistent readings between successive runs, the peak input power level was then incrementally increased.

The initial circuit mechanical design included non-bonded 0.005 inch wide diamond supports and a cold compressed copper sleeve. Helix temperature measurements were repeatable up to 34 W/in of peak input power. However, at a peak input power level of 42 W/in, the helix temperature began to slightly increase with time. A detailed plot of the thermal test results is shown on Figure 2-7. From the graph, the heat shrunk Beo circuit could handle K-band operation with 100 W of output power but the diamond circuits operated much cooler due to a better conduction path. Although the 0.005 inch cold compressed diamond/copper sleeve circuit was stable at the expected load of 30 W/in, the desire for a larger margin-of-safety motivated the design and construction of a lightly modified thermal test circuit.

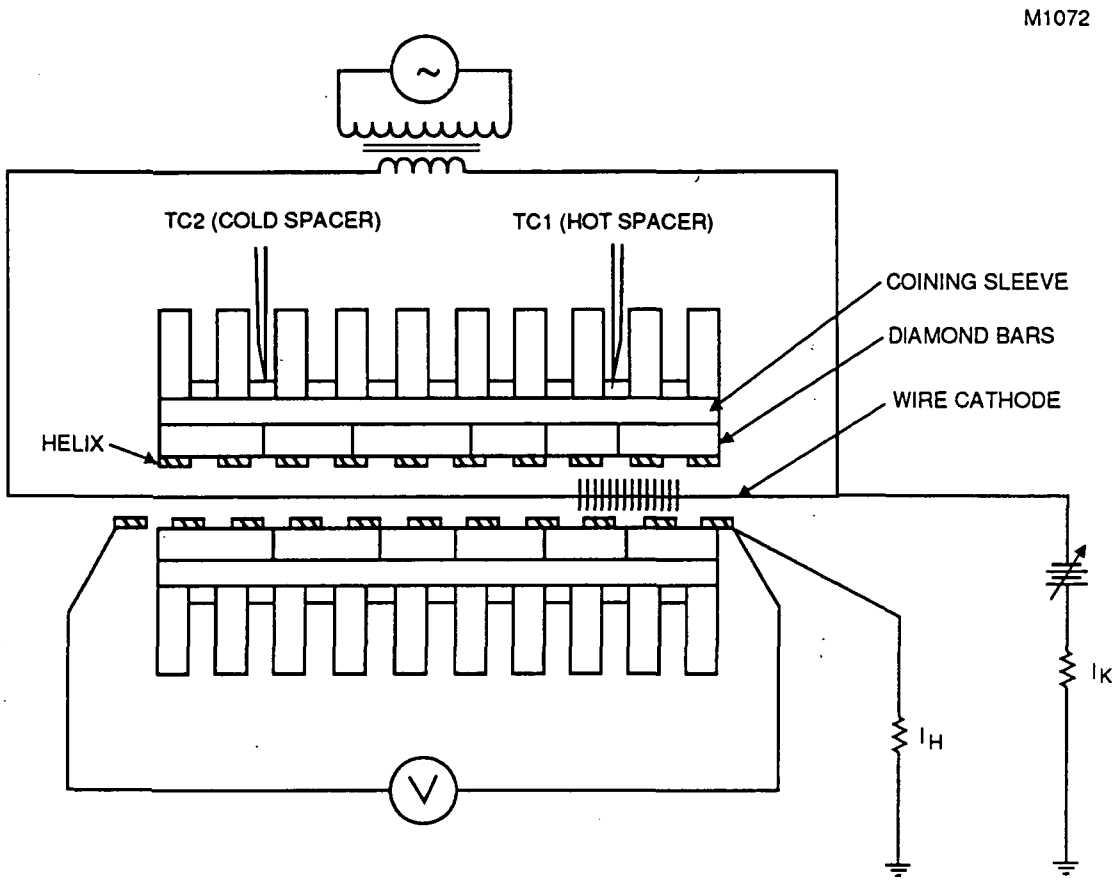

Figure 2-6 Thermal test configuration.

The RF circuit mechanical design was modified to replace the sleeve material from copper to dispersion strengthened copper (also known as GlidCop). Advantages of GlidCop are (1) nearly an eightfold increase in yield strength over annealed copper, and (2) at least an order of magnitude improvement in the secondary creep rate. The nominal sacrifices in the electrical and thermal conductivity properties of GlidCop have insignificant effects on circuit performance. The test results obtained from the 0.005 inch diamond/GlidCop coining sleeve are also plotted on Figure 2-7. Temperatures were stable up to peak input powers of 45 W/in with no signs of degradation. The temperature measurements were lower than those results obtained from the copper sleeve thermal test circuit.

Based on these test results, the improved mechanical properties afforded by the GlidCop material allow higher interface pressures to be maintained over time. As a result, sleeve material for the output circuit was changed to GlidCop.

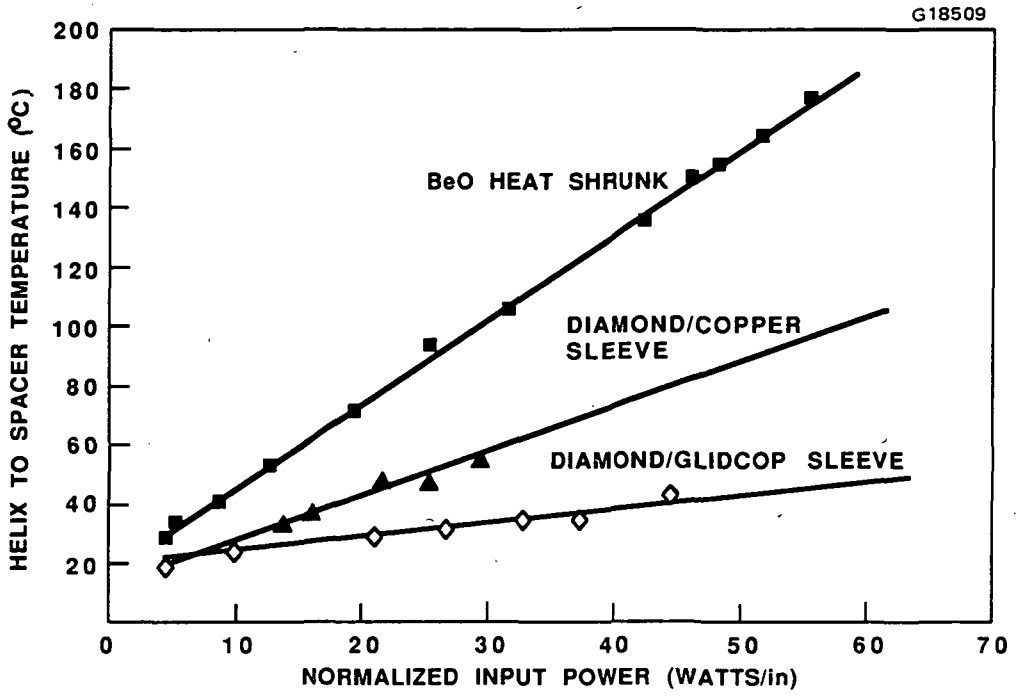

Figure 2-7 Helix temperature comparison.

2.5 DIAMOND CIRCUIT MECHANICAL ANALYSIS

The objective of the mechanical analysis was to investigate the thermal/structural integrity of the diamond supported output circuit, and in so doing, aid in the circuit component design. This was accomplished by predicting the operating helix temperature. A circuit structural analysis was conducted to evaluate the pressures and contact areas at the helix-to-diamond and diamond-to-sleeve interfaces. Outputs of the structural model were then inputted into a two-dimensional thermal model. A maximum helix temperature limit of 300°C was imposed upon the design. Both coining sleeve material alternatives, copper and GlidCop, were analyzed.

Initial boundary conditions for the structural model as depicted in Figure 2-8 were (1) all circuit components at 500°C which will be experienced during bakeout, and (2) the coining sleeve completely stress-free. The temperature was subsequently stepped down to a temperature of 25°C. The expected operating temperatures were then applied and the resulting pressures and contact areas were computed.

Estimates for long term operation predicted a peak of 220°C for the copper sleeve and 255°C for the GlidCop sleeve, both below the design limit of 300°C. However, a direct comparison between the two materials cannot be made because very conservative material property estimates were used for the GlidCop sleeve in comparison to the copper sleeve design due to

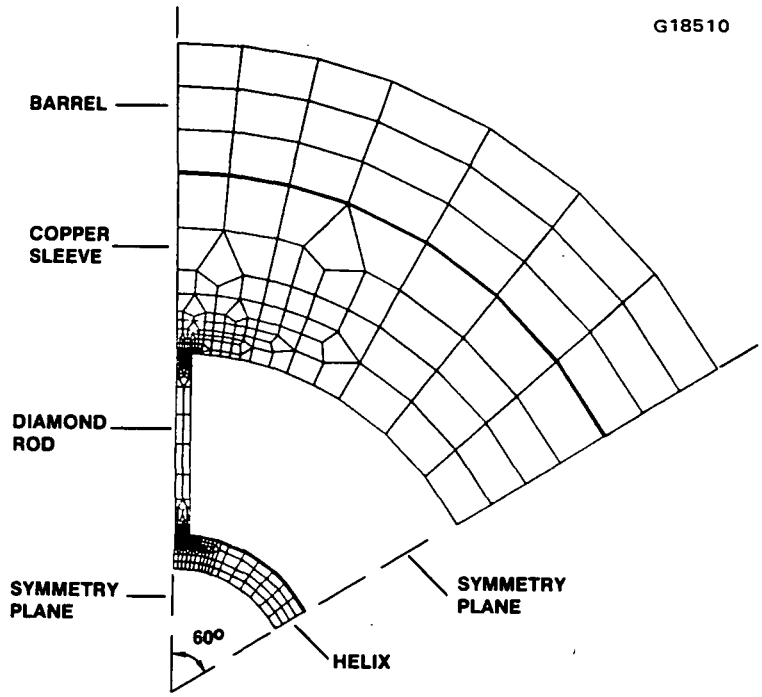

Figure 2-8 Finite element model of the 953H circuit assembly.

a lack of material property data for GlidCop. A detailed report on the analysis procedure and results is found in Appendix A.

2.6 LOSS PATTERNS USING TIC SPUTTERING

As mentioned earlier, a lossy section separates the output from the input circuit for TWT stability. In the past, diamonds bonded to a metal backing strip were attenuated using a cylindrical titanium carbide (TiC) target in a magnetically enhanced diode sputtering system. The loss pattern was generated by varying the speed of the diamond rod structure through the annular deposition region. This system could not be used on the non-bonded diamond sections due to the fixture required to hold the diamond sections together. Instead, an automated magnetron sputtering system was used to deposit TiC on the diamonds. This system provided a significant improvement in controlling the plasma input power over the diode sputtering equipment, allowing the sputtering conditions to be easily reproduced. A mask positioned between the target and the diamonds was designed to generate the desired loss pattern.

Figure 2-9 represents the mask design used to form the loss pattern on SN-1 and SN-2 TWTs. This design relied on "overspray" forming the gradual decrease in loss. The transition from shallow to deep attenuation however was not smooth enough, as is evidenced by the high output VSWR experienced in SN-2. SN-1 would have resulted in high output VSWR but an excessive amount of coating masked the problem (details regarding SN-1 are

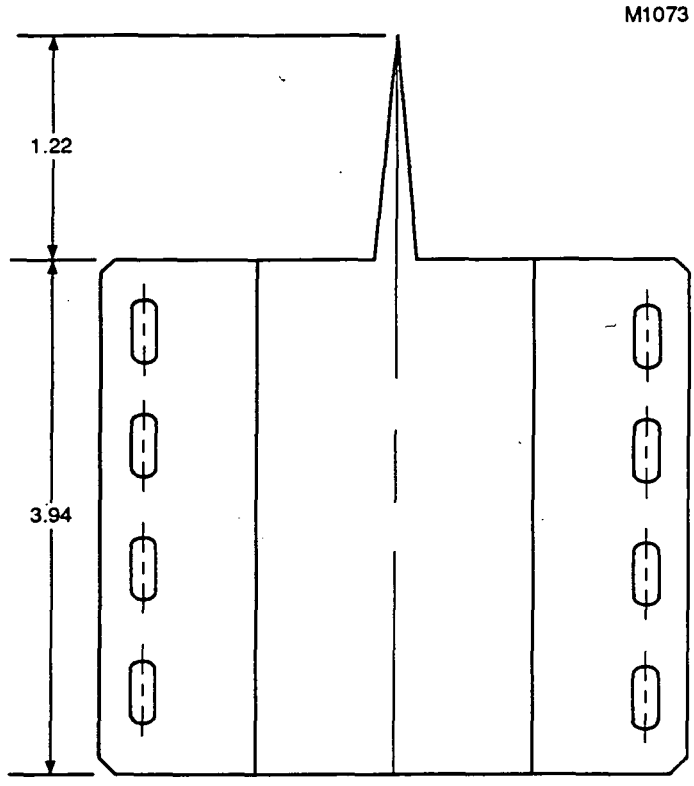

Figure 2-9 Attenuation mask.

found in Section 4.2). A new mask was designed for SN-3 and an illustration is found in Figure 2-10. In this design, the precision machined radius gave the gradual change in attenuation. For additional control, the mask was made in two sections then welded together using an optical technique as shown in Figure 2-11. A 5 mil wire was placed at the top, simulating the 5 mil wide diamonds and the length of the gap gave the desired slope change.

Cold loss measurements of this circuit confirmed that the new method produced a smoother loss pattern transition. Unfortunately, SN-3 was unstable making it difficult to measure VSWR. Oscillations in the output circuit were caused not by VSWR, but by an inadvertent increase in the clean length which occurred when the circuit was reworked. Further details regarding SN-3's construction and circuit rework can be found in Section 4.2.

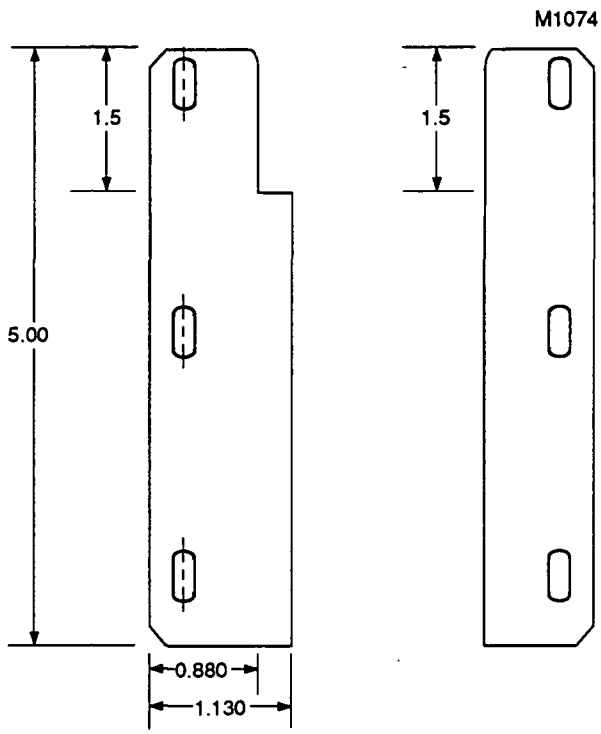

Figure 2-10 Improved attenuation mask.

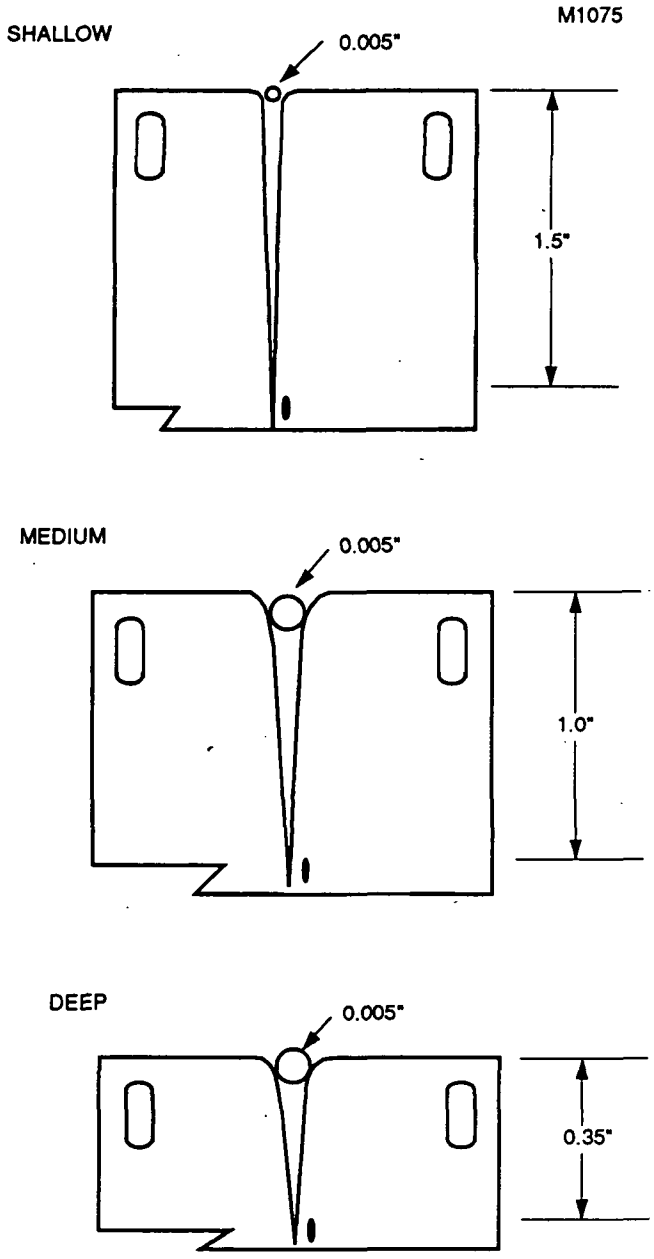

Figure 2-11 Welding instructions.

3.0 TWT DESIGN

3.1 DESIGN APPROACH

The primary objective of this TWT development effort was high overall efficiency. Other objectives considered important were high power capability and low signal distortion. To satisfy the primary objective and achieve a reliable design, the design approach was to use the 918H as the baseline design. The 918H is a 20 GHz, 50 watt helix type space TWT that was developed for NASA under Contract No. NAS53-23345. The 918H, as well as this tube design, was based upon a low beam perveance approach. As is well known, for low perveance designs, beam conversion efficiency are reduced due to lower space charge effects. However, higher overall tube efficiencies can be realized through effective recovery of the spent electron beam energy. This is one technique for efficiency enhancement; the other efficiency enhancement techniques were concerned with the interaction circuit.

One of the circuit efficiency enhancement techniques in the TWT design was to increase the circuit interaction impedance and reduce circuit losses by reducing the dielectric loading of the helix support rods. This was accomplished by utilizing very thin sections of diamond which support the helix at the critical output area.

A second circuit efficiency enhancement technique was the incorporation of a velocity tapered helix in the large signal region. This technique increases the beam conversion efficiency by maintaining synchronization of the circuit phase velocity with the beam velocity. The taper is also designed for operation near synchronous voltage which ensures low signal distortion. This type of velocity taper design approach was developed by Dr. H. Kosmahl, formerly of NASA Lewis Research Center. Known commonly as a dynamic velocity taper or DVT, this efficiency enhancement technique also provides improved amplitude linearity near saturation.

The third technique for efficiency enhancement utilized was to maximize the recovery of the spent beam by incorporating a four-stage depressed collector with graphite electrodes. Due to its material properties, graphite decreases the amount of back-streaming electrons which reduces the power losses of the spent beam in the collector.

Thus, these three efficiency enhancement techniques when used in conjunction with the low beam perveance approach should result in a TWT with high overall efficiencies. This was supported by analysis that demonstrated that power losses in the collector can be reduced by using a low beam perveance design approach. In addition, although lower perveance designs generally result in lower beam efficiencies, the velocity taper and high impedance diamond circuit provide sufficient improvement to more than offset any beam efficiency reduction.

In the scaling process, from the 918HA to the 953H, considerations were made for the efficiency enhancement techniques just described in the tube design. For example, since a high impedance diamond circuit was used in the design, a higher beam conversion efficiency was used in the computations. The results of these computations are summarized in Table 3-1, which shows design features for the 953H as well as the 918H.

The following sections will describe the efficiency enhancement techniques that are used in the 953H and then the electron gun and PPM designs will also be discussed.

3.2 RF CIRCUIT DESIGN

A two-section input circuit is used in the 953H TWT. The two sections are used because of the high gain requirement for the TWT and each section will be short enough so that backward-wave oscillation (BWO) problems will not be encountered. Since the input circuit provides only gain and is quite long; the lower impedance beryllia supported helix circuit is

TABLE 3-1
953H DESIGN FEATURES

Parameter	918HA (Baseline Design)	953H
Frequency (GHz)	17.7 - 21.2	17.7 - 20.2
Gun Perveance (μP)	0.065	0.053
Operating Voltage (kV)	-10.7	-9.7
Cathode	Type M	Type M
r_{95} (minimum)	0.0101"	0.0082"
Helix diameter (2a)	0.047"	0.47"
Helix tape size	0.007" x 0.020"	0.006" x 0.015"
Helix support material	Beryllia	Diamond IIA
Helix support size	0.020" x 0.037"	0.005" x 0.030"
Collector stages	4 current collecting stages plus a spike	3 current collecting stages plus a spike
Collector electrode material	TiC coating on copper	POCO graphite
Magnetic Field (G)	2700	3500
$\lambda \rho / L$	5.00	3.25

used. This approach was chosen primarily for cost effectiveness. A cross sectional drawing of the 953H input circuit assembly is shown in Figure 3-1.

Figure 3-2 shows the cross sectional drawing of the 953H output circuit assembly. As discussed previously, this helix circuit uses very thin diamond support bars which results in high interaction impedances and low circuit losses.

3.3 VELOCITY TAPERED HELIX

The output RF circuit incorporates a DVT helix. The principal objective behind the DVT is to optimize the interaction process between the traveling RF circuit wave and the electron beam. By maintaining synchronization of the circuit and electron beam phase velocities throughout the entire circuit length, the transfer of kinetic energy is maximized.

A measure of the synchronization between the RF circuit wave and electron beam is indicated by Pierce's velocity parameter. In the small signal region of the circuit, the bunched electron beam is well defined. Here, the small signal gain and the velocity parameter can be accurately determined. When the beam enters the large signal gain region, the electrons exponentially transfer their kinetic energy to the RF wave as a function of axial

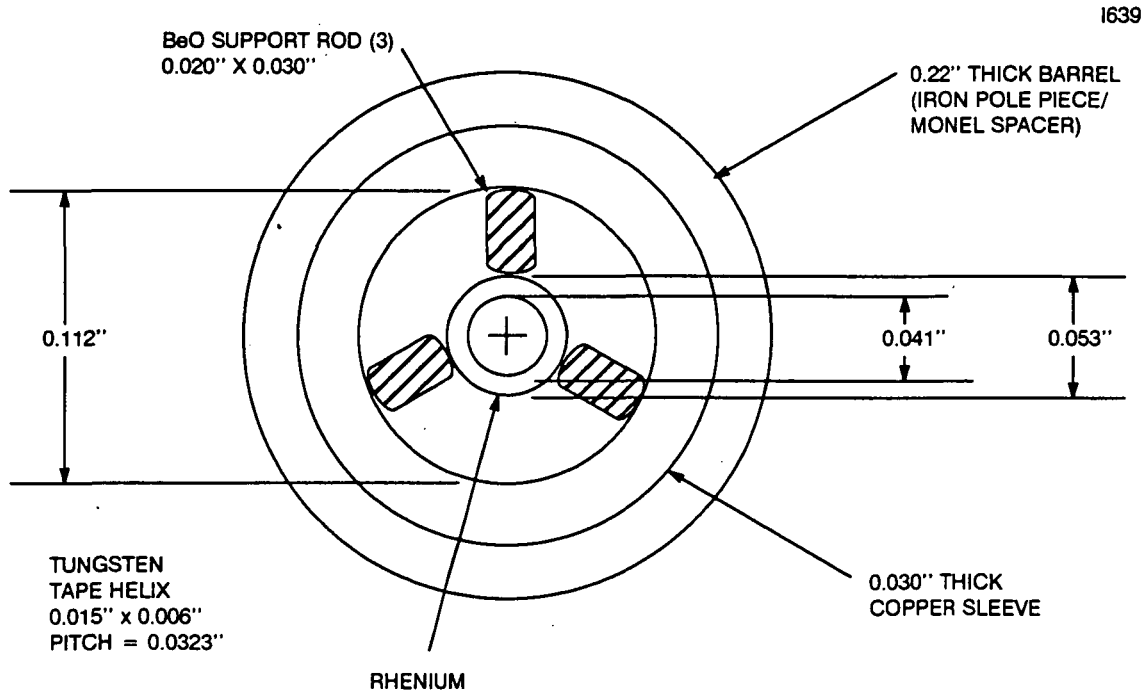

Figure 3-1 Cross-section of the 953H input circuit assembly.

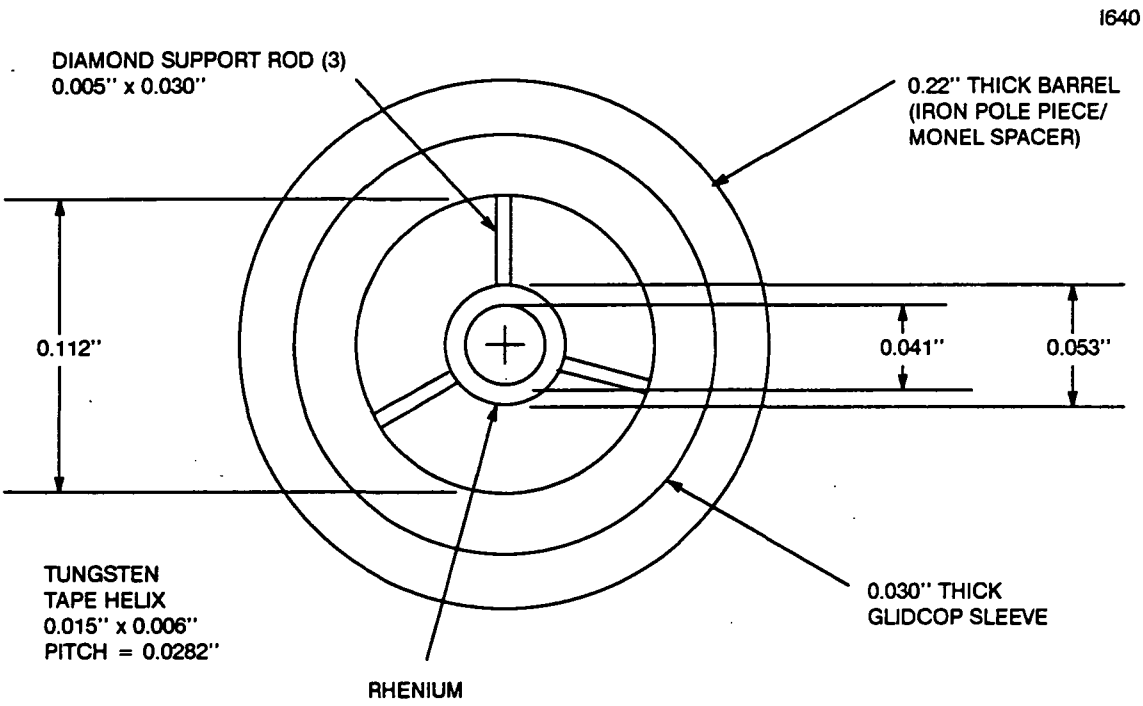

Figure 3-2 Cross-section of the 953H output circuit assembly.

distance. At the transition from small signal to large signal, the taper is initiated. The velocity parameter as a function of distance is maintained close to zero by exponentially decreasing the helix pitch as the electron beam velocity decreases.

3.3.1 Comparison Between Computed and Measured DVT Designs

Figure 3-3 shows the helix pitch profiles for the three breadboard TWTs that were built and tested during this development program. As seen in the figure, the input circuit section for the TWTs are quite long and this occurs because the input is made into two sections for the high gain requirement. The two active input sections are electrically isolated by attenuators and each of them are quite short for BWO stability.

In the output circuit, a section which precedes the DVT section has been denoted as the driver section. The driver section pitch for the first two breadboard tubes was chosen for 0 percent over-voltaging. Also note in Figure 3-3, that the first two breadboard tubes used linearly tapered DVT circuits with tapered pitches of 12 and 11 percent, respectively. The linear tapered DVT circuits were initially used since computations at that time indicated that linear tapered helix was equivalent to an exponential design and that no additional efficiency could be achieved with the exponential taper. That conclusion however, was based

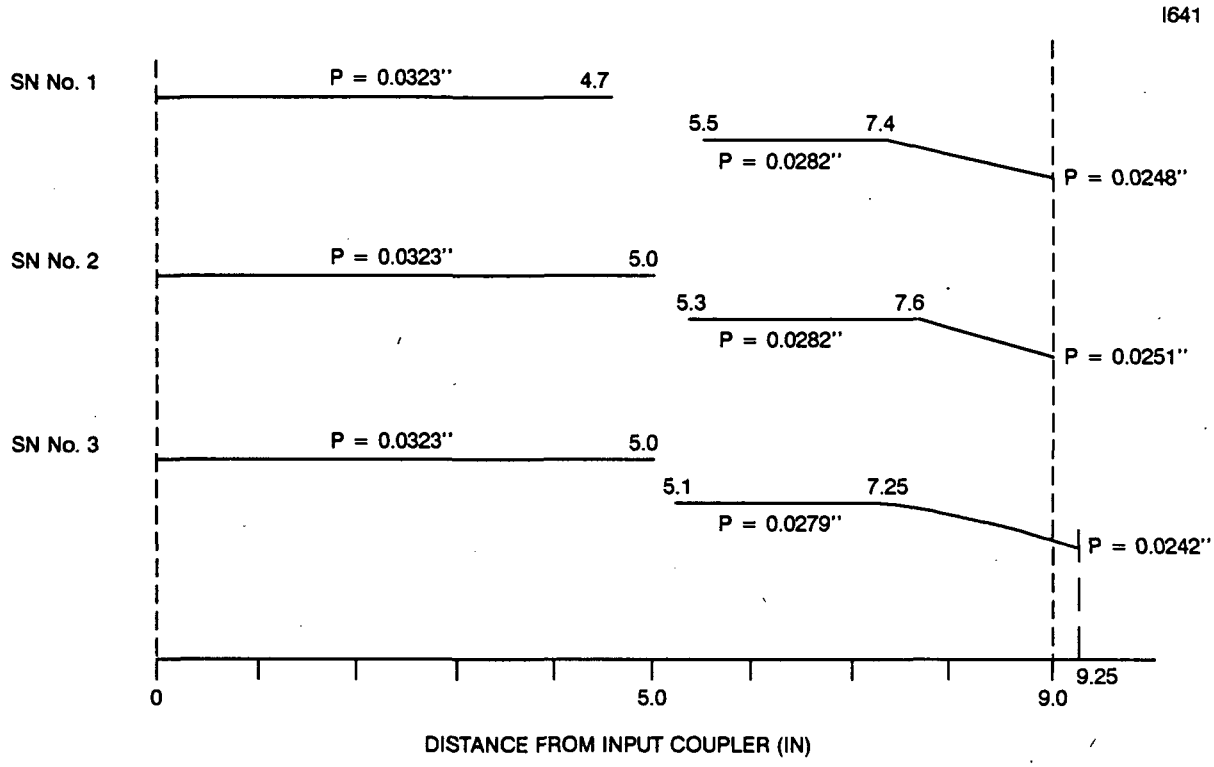

Figure 3-3 953H helix pitch profiles.

on computer runs that utilized an incorrect beam size. The incorrect beam size problem will be addressed when discussing SN-2.

Step function approximations of the actual measured loss patterns for the input circuits for the three breadboard tubes are shown in Figure 3-4. In Figure 3-5 is the actual measured output loss for the three tubes.

3.3.1.1 Breadboard TWT SN-1 – The objectives of this breadboard TWT were to evaluate the first-cut RF design and the thermal and RF power handling capability of the diamond supported helix structure. SN-1 achieved three milestones: (1) over 75 watts of output power across the band, (2) long-term thermal stability at 100 watts of RF power, and (3) freedom from any backward wave oscillation.

At the original design voltages of 9700 volts on the cathode and 51 mA of cathode current, the power output and saturation gain were quite low. The power output was 20 watts, corresponding to a 4 percent beam efficiency versus a predicted value of 19 percent. Saturated gain was 30 dB in comparison to a 48 dB expected gain. Further testing revealed that the low power and gain were due to a manufacturing problem where an excessive amount of loss was deposited on the diamond rods. The output attenuator loss was five

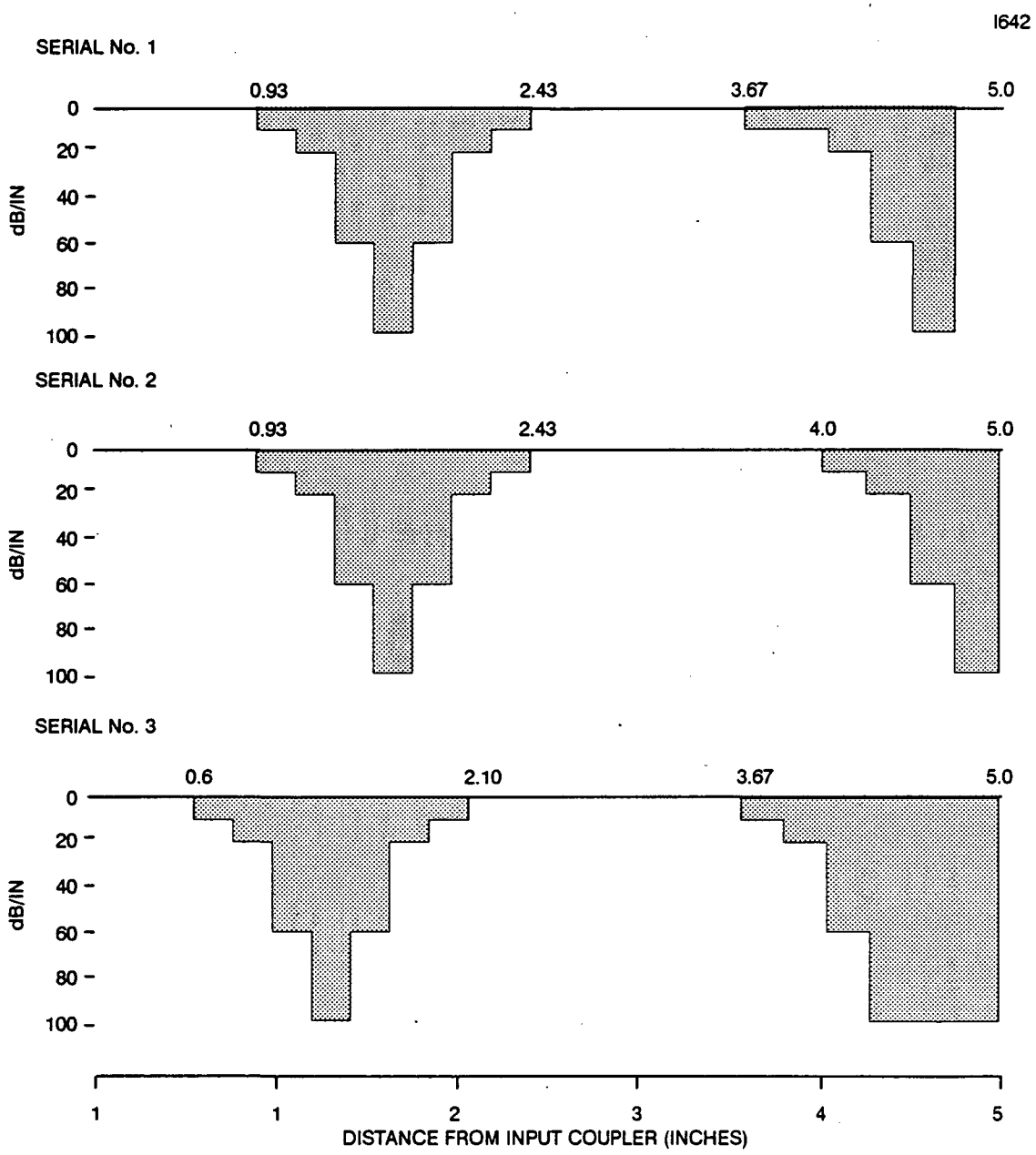

Figure 3-4 953H input circuit loss patterns.

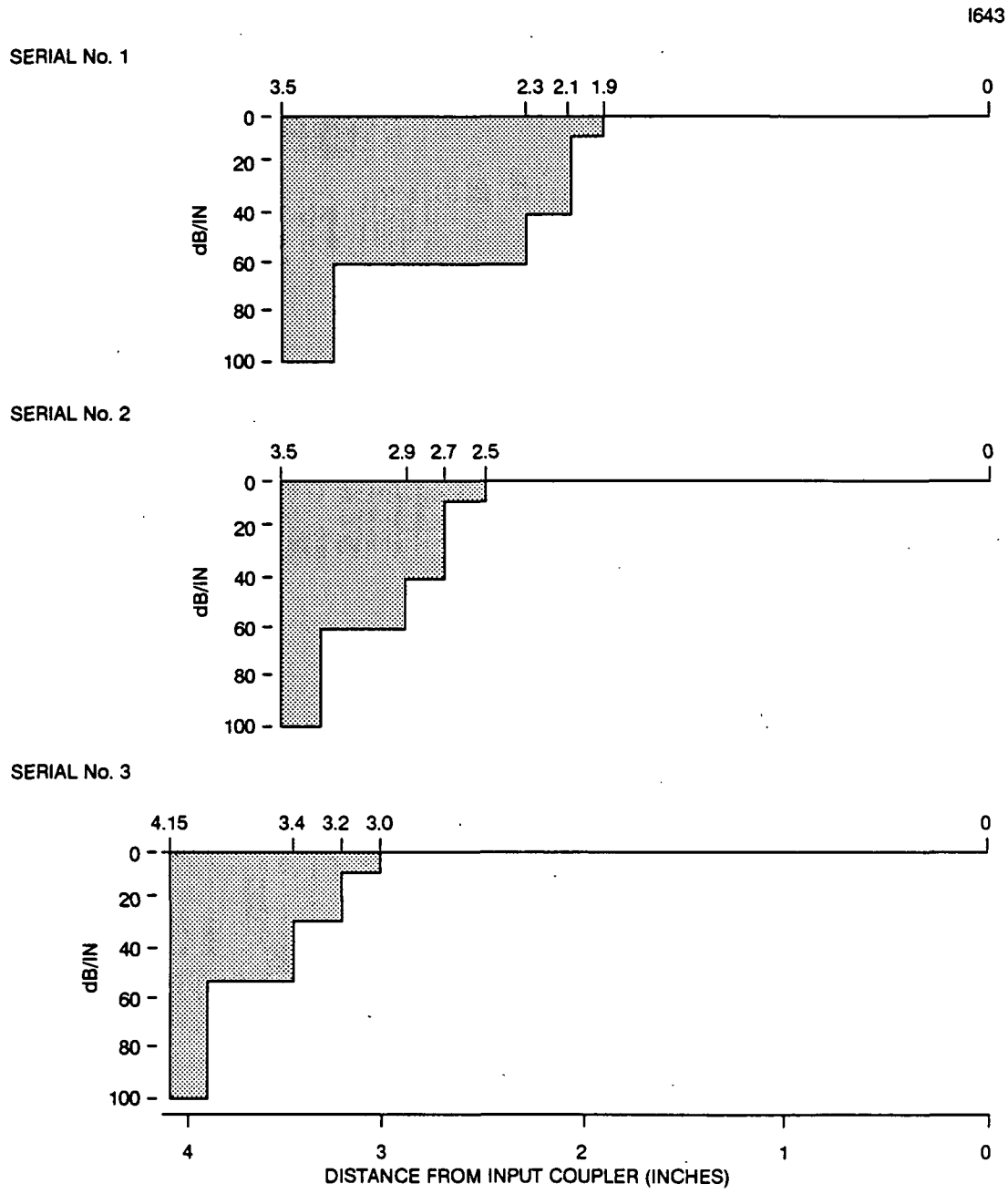

Figure 3-5 953H output circuit loss patterns.

times greater than required. This attenuator pattern resulted in a very short output circuit section, hence, poor beam efficiency and low gain occurred.

3.3.1.2 Breadboard TWT SN-2 – This tube achieved the highest overall efficiency recorded for a K-band TWT; 54.6 percent. The overall efficiency goal of 60 percent however, was not met because the basic efficiency was 16.9 percent instead of the expected 20 percent. A thorough review of the design process revealed that the circuit had been designed using an improper beam size.

In the DVT code, balanced flow is based upon the Brillouin equation given by:

$$r = \frac{0.462 * [\ (V_o) * (P_o)\ ]^{.5}}{(B_{pk})}$$

where:

	r	is beam radius in inches
	V_o	is beam voltage in volts
	P_o	is beam perveance in micropervs
	B_{pk}	is peak magnetic field in gauss

Thus, for a given beam voltage, beam perveance and peak magnetic field, the beam radius is defined by the above equation to achieve balanced flow. If the beam size used is not consistent with the above equation, then a large amount of rippling will occur in the electron beam. The amount of rippling would depend upon how deviant the inputted beam radius was from the balanced flow condition.

Historically, the DVT code was ran by using the actual beam voltages, beam perveances and the peak magnetic fields. The beam radius that was then inputted in these cases were then calculated using the above equation and this beam radius has been defined as the "non-thermal" beam radius. When the DVT code was operated in this manner, good agreement between calculation and measured data occurred.

Unfortunately, in the early phase of the 953H development program, an incorrect beam size, not consistent with the above equation, was used in the computations. The incorrect beam size corresponded to a beam radius which encompasses 95 percent of the thermal electron beam. In this case, the magnetic field was not consistent with the beam size because the Brillauin equation was not used. Computer results predicted 20 percent basic efficiency and no indication of a problem was apparent. A revision, however, was made to the DVT program which plots the electron beam. From these plots severe beam rippling and large circuit beam interception were exhibited. Also, when the DVT code was operated in this

manner, the computations indicated no differences in calculated efficiencies between linear and exponential tapers. Once the discrepancy between predicted and measured beam efficiency was understood the design for breadboard No. 3 was performed. For general information, Table 3-2 contains the design parameters as entered into the DVT code for each of the TWTs.

3.3.1.3 Breadboard TWT SN-3 – As just explained, a thorough review of the previous design process revealed that the circuits had been designed using an improper beam size. Computations were then repeated and results indicated that up to 19 percent basic efficiency could be achieved with a linear taper DVT, but the designs in each case proved to be unstable when evaluated for BWO stability. Exponential taper designs thus were re-explored. Computations then showed that using the correct design parameters resulted in a 3 percent point improvement in the exponential taper over the linear tapered design.

The helix circuit design shown in Figure 3-3 for breadboard No. 3 has a 13.3 percent exponential taper over 2.0 inches in length. Figure 3-6 illustrates projected basic efficiency for the same exponential taper at different clean or driver circuit lengths. The new output circuit incorporated 0.7 inches of clean length before the taper starts corresponding to a 20 percent basic efficiency. A second curve is found in Figure 3-6 described as "JHELIX PREDICTION". This curve represents computer results using the Hughes large signal program which behaves similar to the DVT code. The JHELIX code was used to increase confidence in the selected helix design and thus increase the probability of meeting or

TABLE 3-2
DVT DESIGN PARAMETERS

Design Parameter	SN-1 and 2	SN-3
f (frequency of operation, GHz)	18.95	18.95
a (mean helix radius, inch)	0.024	0.024
b/a (beam fill factor)	0.346	0.131
B_o (peak centerline magnetic flux density, Tesla)	0.3600	0.3600
V_o (beam voltage, kV)	9.7	9.7
I_o (beam current, mA)	51.0	57.0
Output interaction impedance at radius a (ohms)	47.8	52.34
V/C (normalized phase velocity)	0.191563	0.185174
L_M (magnetic period)	0.28	0.28

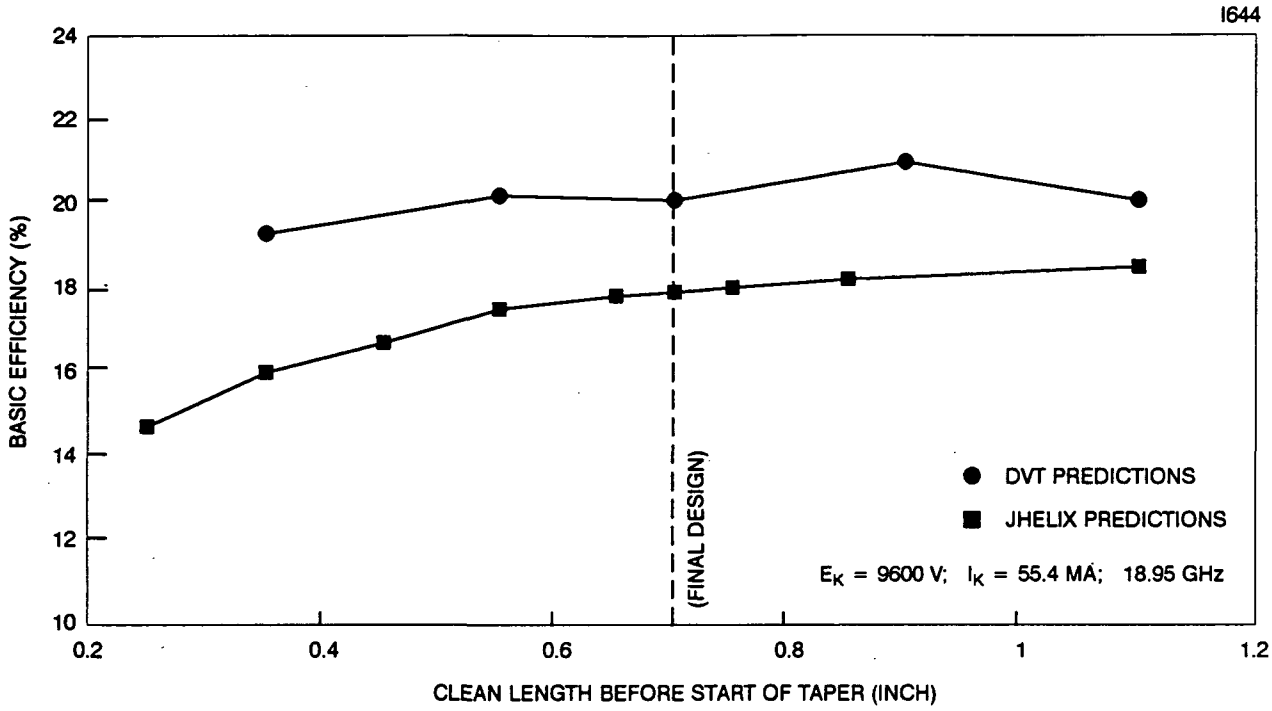

Figure 3-6 953H BB3 final design/efficiency versus clean length.

exceeding the 60 percent efficiency goal. The design for the TWT was also evaluated for BWO stability and resulted in greater than 2 to 1 margin, as depicted in Figure 3-7.

SN-3 exhibited a 17 percent basic efficiency, which was three percent lower than the DVT program predicted and one percent lower than GHELIX. Historically at Hughes, the GVT program has had very good correlation between predicted and actual TWT results, but to make a conclusion about either code, additional units would have to be built. Not only can a sample of one be misleading but SN-3 had some problems that could be masking true power capabilities. SN-1 and SN-2 showed very good output power stability, on the other hand SN-3 exhibited a 0.2 dB degradation in output power with time. SN-3's construction was different than the previous two units. The antenna that RF couples into the output window and also provides a thermal interface from the helix to the barrel was not properly brazed in place due to an incorrect material issue. Normally, the antenna sleeve is brazed to the antenna and the barrel as shown in Figure 3-8. When the sleeve was brazed in place for SN-3, the resulting joint was very poor. The sleeve was locked in place but visual inspection showed that the braze material had not flown properly. Further inspection revealed that the sleeve was not made of monel as designed but of stainless steel. The stainless steel sleeve oxidized in the wet hydrogen atmosphere, preventing the braze material from adhering to the sleeve. To assure good contact the antenna sleeve was laser welded in place but, from

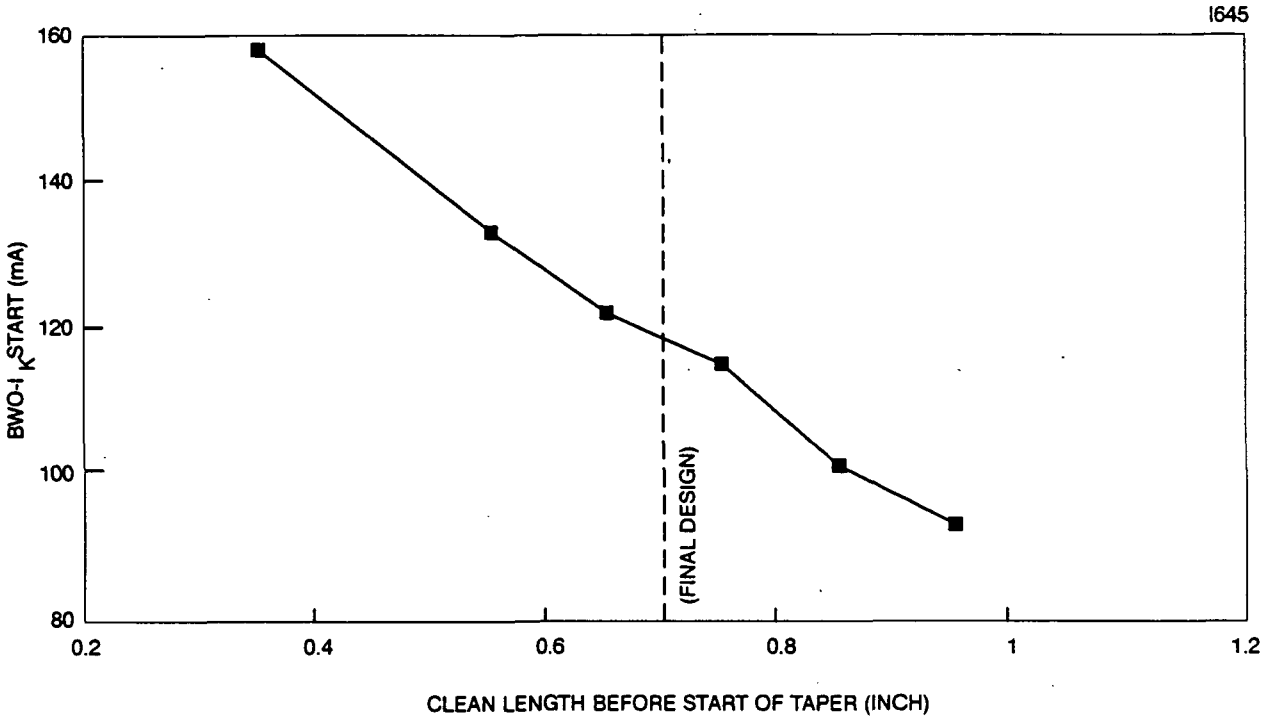

Figure 3-7 953H SN3/clean length versus BWO starting current.

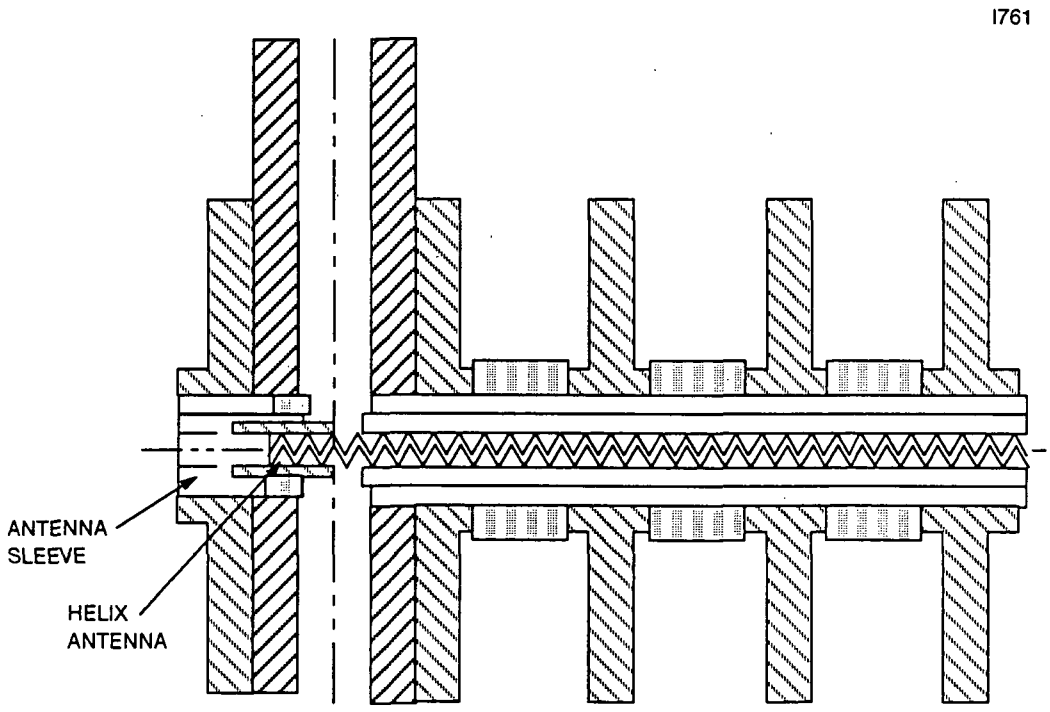

Figure 3-8 Helix to barrel thermal path.

SN-3's performance the interface proved to be a poor thermal path from the helix to the barrel. The output circuit could not be rebuilt due to end of contract restrictions.

3.4 MULTISTAGE GRAPHITE COLLECTOR

The multistage graphite collector, as depicted in Figure 3-9, consists of four voltage depressed stages. The mechanical design features internally isolated electrodes which allow the outer shell to be grounded. The outer shell is electrically isolated from the electrodes by a single ceramic cylinder. Once the graphite electrodes are located properly, the assembly is brazed in a vacuum furnace using an active metal braze.

The first three stages sort and collect the spent electron beam according to the kinetic energy of the electrons entering the collector. Electrons with low kinetic energy levels are collected at the front stages of the collector while electrons with higher energy levels enter deeper into the collector and are collected on the back stage. The fourth stage is a collector spike which operates at cathode potential and collects only those few electrons which have gained rather than lost energy from the RF interaction process. The primary function of the spike, however, is not to collect electrons but to improve the collection of electrons on the third stage by suppressing secondary electrons that are generated at the collecting surfaces of the third stage. In general, the higher the collector stages can be voltage depressed

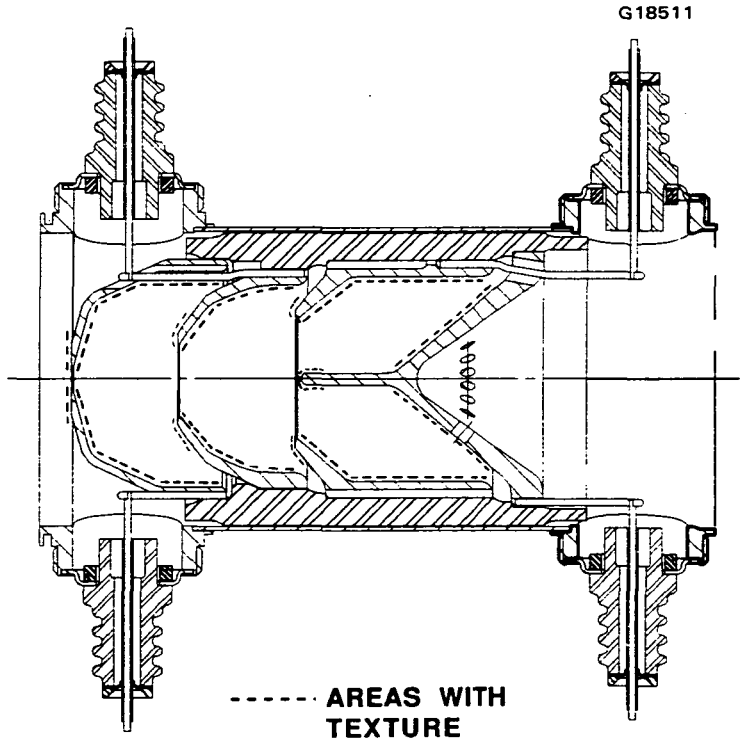

Figure 3-9 Cross section of a four-stage POCO collector.

without generating undesirable back-streaming electrons, the greater the recovery of spent beam energy. This reduces the TWT dc power consumption and thereby increases the TWT overall efficiency.

Back-streaming electrons increase the thermal loading of the output circuit and reduce TWT overall efficiency. Therefore, minimizing these electrons is one of the objectives in good collector design. Isotropic graphite was selected as the electrode material because of its low reflected primary electron yield index and secondary electron emission ratio. The reflected primary electron yield index is two to five times lower than copper and the secondary electron emission ratio is about one-half. These key properties of graphite significantly reduce back-streaming electrons and typically improve overall TWT efficiency by three to four percentage points. Ion-texturing the critical surfaces of the graphite electrodes further improves the overall TWT efficiency by about one percentage point.

Figure 3-10 shows electron trajectories in the collector region for the 953H TWT using a DVT circuit operating at 20.2 GHz. This computation was performed using the Herrmannsfeldt electron trajectory code. The collector operation at 20.2 GHz is shown since this corresponds to the worst case where the spent electron beam energy distribution "knee voltage" has its minimum value. At lower frequency, the "knee voltage" increases and the collector efficiency improves. These characteristics are shown in Table 3-3 where predicted overall efficiency for the final design 953H are tabulated. The efficiency values shown in this table are presented as a function of operating frequency: Note that the overall efficiency is predicted to have a minimum value of 58.6 percent at 20.2 GHz.

3.5 ELECTRON GUN

The baseline design for the 953H electron gun was also taken from the 918H TWT. The electron gun uses a normal Pierce type electrode for beam formation to achieve the desired electron beam dimensions. Table 3-4 lists the electron gun design parameters for the 953H TWT and, for comparison, the 918H characteristics are also shown. The r_{95} beam radius is defined as that radius which encompasses 95 percent of the thermal electron beam current. The r_0 beam radius corresponds to Herrmann's thermal beam radius and is that radius which has constant current density across its cross section; this distribution represents the space charge forces of the thermal electron beam. The PPM magnetic focusing parameters for the 953H shown in Table 3-3 will be discussed in the next subsection. The cathode current loading used in the electron gun is 0.7 A/cm^2 and with the cathode operating at 960 $^{\circ}C$ brightness, life in excess of well over 10 years can be conservatively projected.

Figure 3-11 shows the thermal beam profile of the 953H electron gun. The beam radius corresponding to the r_0 and r_{95} beam are as previously defined. The $r_{99.5}$ beam profile

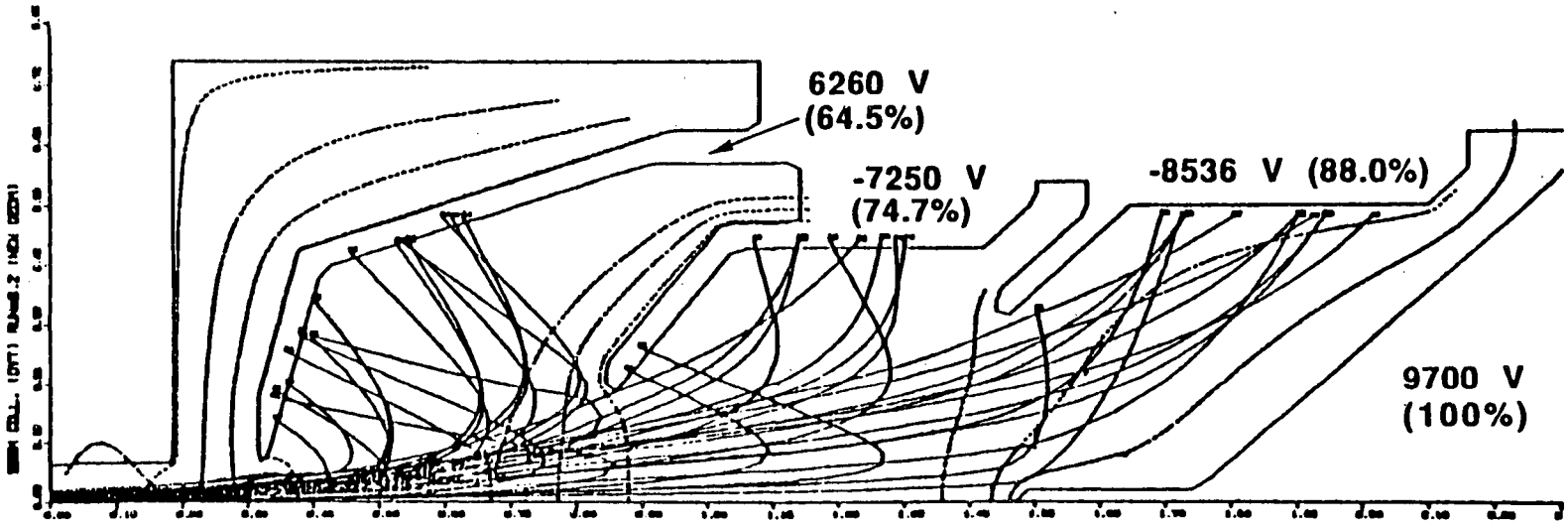

Figure 3-10 Electron trajectories in the collector region for the 953H using a DVT circuit.

TABLE 3-3
953H FINAL TWT DESIGN PREDICTED OVERALL EFFICIENCY

η \ FREQ GHz	17.70	18.95	20.20
η_C	0.917	0.908	0.888
η_E	0.198	0.198	0.201
η_{CKT}	0.90	0.90	0.90
η_{INT}	0.02	0.02	0.02
η_{OV}	0.630	0.615	0.586

$$\eta_{OV} = \frac{\eta_E \cdot \eta_{CKT}}{1 - \eta_C + \eta_C (\eta_E + \eta_{INT})}$$

η_C = Collector Efficiency

η_E = Electronic Efficiency

η_{CKT} = Circuit Efficiency

η_{INT} = Circuit Interception

η_{OV} = Overall Efficiency

TABLE 3-4
ELECTRON GUN DESIGN PARAMETERS

Description	Units	918H	953H
Cathode Voltage	V	-10,750	-9,700
Cathode Current	mA	72.5	51.0
Beam Perveance	P	0.065	0.053
r_{95} (Minimum)	Inches	0.0100	0.0083
r_0 (Minimum)	Inches	0.0076	0.0050
Beam Filling Factor (r_{95}/a)	—	0.42	0.35
Peak Axial Magnetic Field	Gauss	2700	3600
Magnetic Period	Inches	0.220	0.290
λ p/Lm	—	5.00	3.25
r_{95} (Maximum)	Inches	0.0136	0.0117
Δ r_0 (Ripple)	Inches	0.0032	0.0033

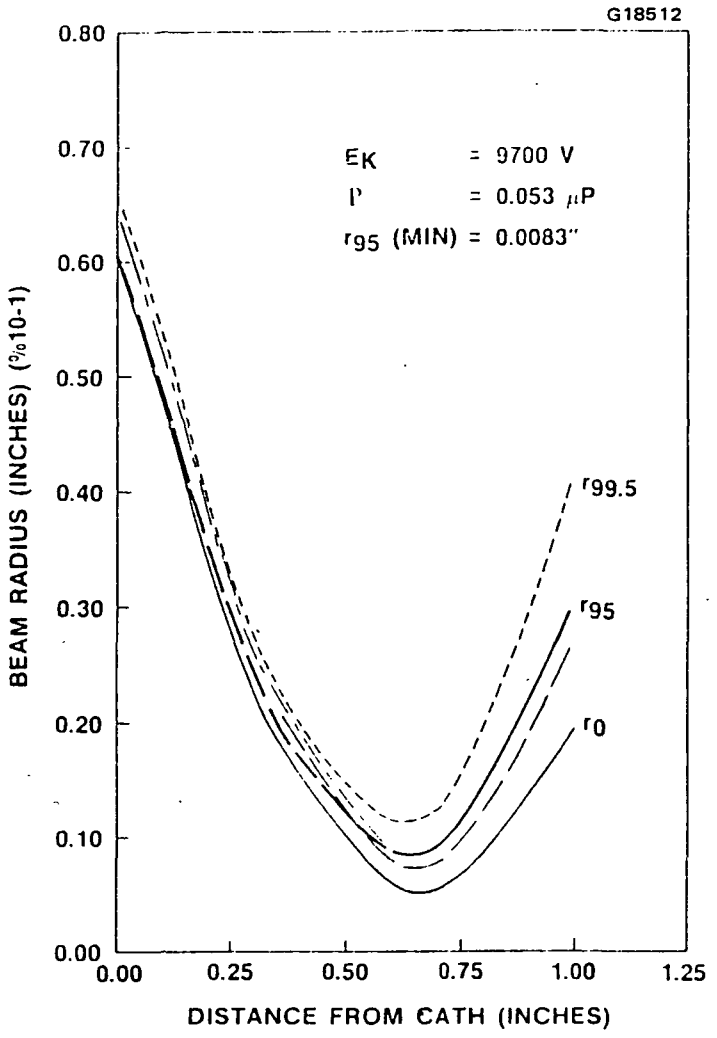

Figure 3-11 953H gun thermal beam profile.

corresponds to the beam radius which contains 99.5 percent of the electron beam current. Figure 3-12 shows beam trajectories from the cathode into the PPM focusing field region. Note in the figure the well behaved electron trajectories and the maximum values are all within the inner diameter of the helix radius.

3.6 PPM DESIGN

As shown in Table 3-4, the 953H electron beam is focused using a PPM design with a peak field of 3600 gauss. The PPM magnet period is 0.290 inches, thus resulting in a plasma-wavelength to magnet period ratio of 3.25. This is a conservative value for the plasma-wavelength to magnet period ratio and was so chosen to assure excellent beam containment. The PPM stack uses samarium-cobalt magnets which are temperature compensated so that

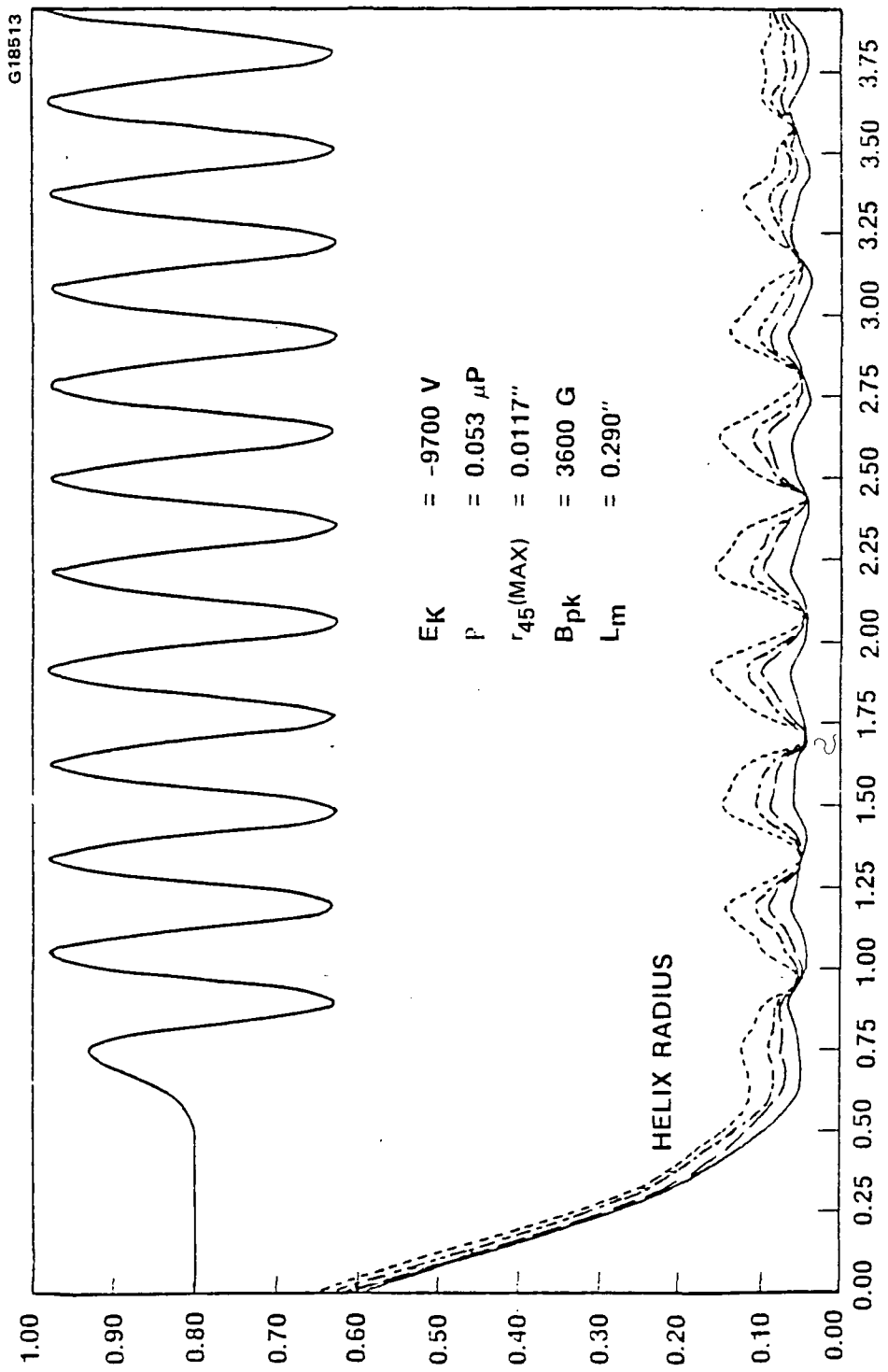

Figure 3-12 Electron trajectories from the cathode into the PPM focusing field region for the 953H TWT.

the magnetic field changes by only 0.025 percent/°C. Figure 3-13 is a plot of peak magnetic field and pole piece flux as a function of the PPM magnet outer diameter. Note that to achieve a peak magnetic field of 3600 gauss, the pole piece flux density will be 14 kilogauss. To minimize the external leakage field while raising the internal magnetic field, the pole piece outer diameter has been undercut relative to the magnet outer diameter. Also listed in the figure are other PPM magnet stack design details for the 953H such as pole piece inside diameter, thickness, gap and magnet thickness.

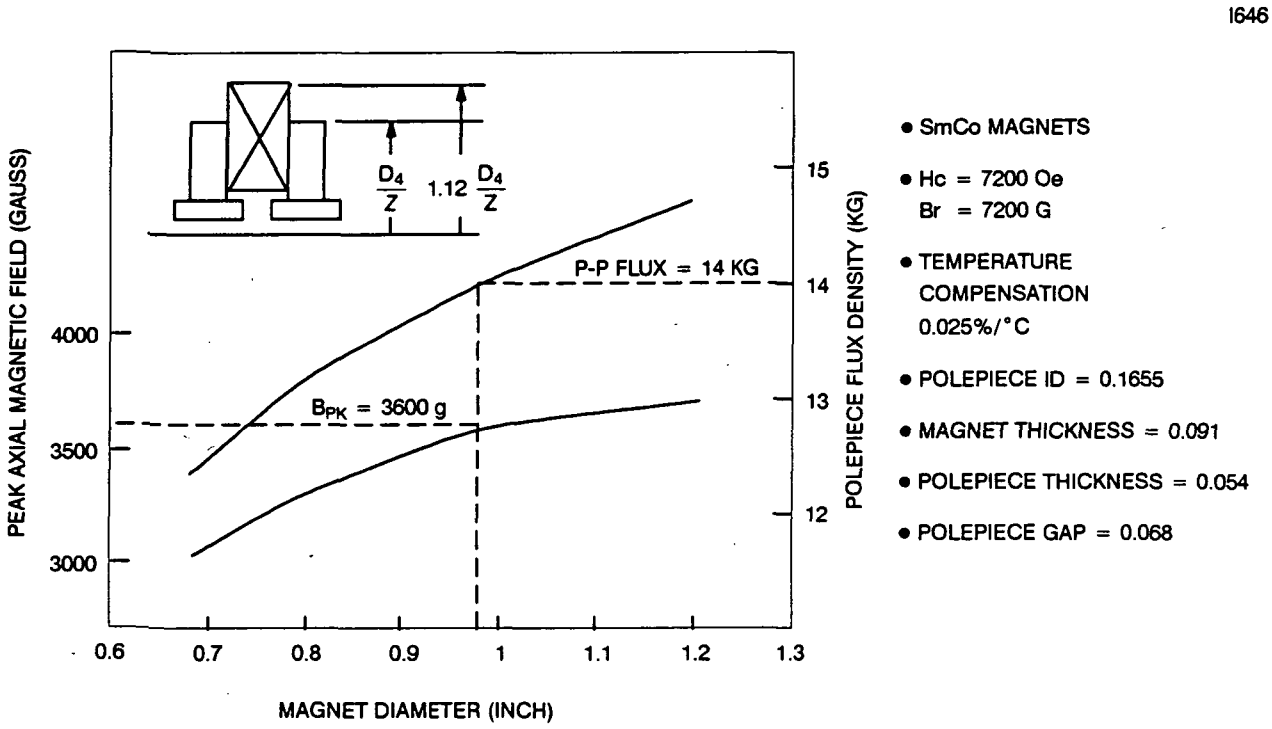

Figure 3-13 Peak magnetic field and flux density versus magnet outer diameter.

4.0 TWT CONFIGURATION

4.1 INTRODUCTION

As depicted in the TWT's cross-sectional view found in Figure 4-1, the 953H mechanical gun design utilizes internally isolated electrodes which allow the outer shell to be grounded. This design eliminated the need for high voltage potting material and the associated problems. The inner gun is a stacked brazed assembly which has demonstrated high performance under adverse shock and vibration conditions. Direct helix-to-waveguide coupling was employed to minimize RF losses. In this design an antenna, or metal cylinder brazed to the helix provides the coupling mechanism to a half height waveguide. The four-stage collector also utilized internally isolated electrodes allowing the shell to be grounded. The grounded shell along with conservative voltage stresses significantly contributed to the overall reliability of the TWT.

Three vacuum assemblies were built under this program. Each assembly had a slightly different configuration and Table 4-1 lists the major differences between each TWT.

4.2 CONFIGURATION BY SERIAL NUMBER

SN-1's Vacuum Assembly was completed in March of 1988. Testing of this unit revealed that there was an insufficient amount of output gain. Investigation into this problem suggested that an excessive amount of TiC was sputtered onto the diamonds in the process of creating the desired loss patterns. Loss measurements were performed on the composite diamond rods using a slotted line fixture. The fixture is made up of a helix circuit with a longitudinal slot in the outer conductor through which a probe on a carriage is inserted. The loss relative to position along the helix is then obtained by moving the carriage along the slot and reading the power coupled into the probe. The differences in the fixture circuit and the 953H design however were not accounted for. Thus, five times the expected loss was deposited on the diamond support rods. For SN-2, the problem of excessive loss was eliminated by applying the appropriate correction factors. Figures 3-4 and 3-5 in the previous section illustrate the approximate attenuation patterns for each breadboard TWT.

The original DVT design assumed non-realistic loss patterns; 5 dB/in loss under the attenuator pattern and an abrupt increase to 100 dB/in. The DVT program assumes a perfectly matched circuit, but in an actual TWT this loss pattern would create a large mismatch and, consequently, a large amount of reflected power. To better simulate real hardware a more practical pattern was entered into the DVT program and the optimal helix pitch was recomputed and incorporated into SN-2. This accounts for the small change in the helix profiles found in Figure 3-3. The input length increased by 0.3 inch and the output helix by 0.2 inch.

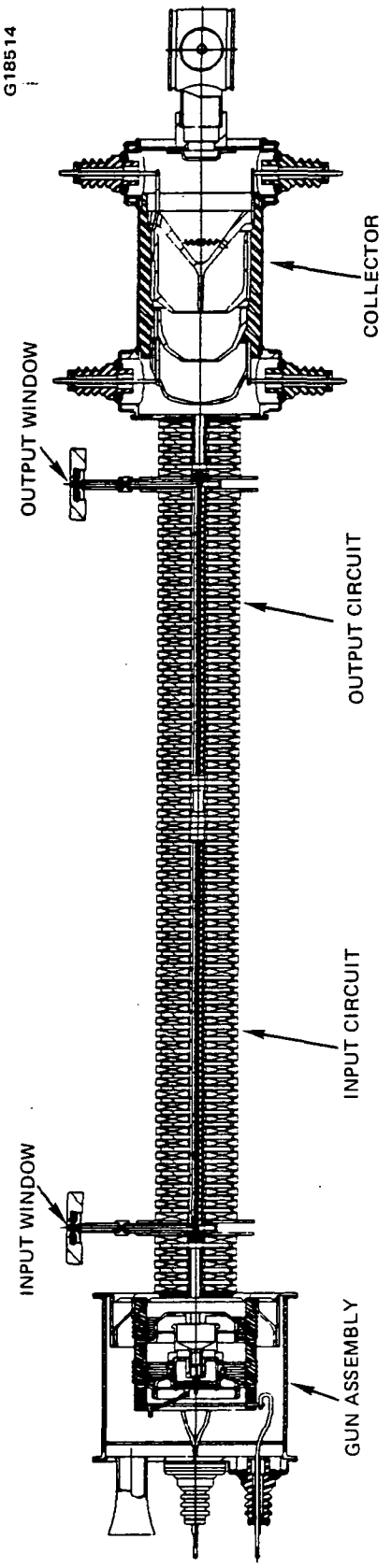

Figure 4-1 953H TWT final vacuum assembly.

TABLE 4-1
SUMMARY OF TWT CONFIGURATION

Assembly	SN-1	SN-2	SN-3
Gun	918 Baseline	No Change	No Change
Input Circuit			
Helix Support Material	BeO	BeO	BeO
Helix Pitch (Inch)	0.0323	0.0323	0.0322
Helix ID (Inch)	0.041	0.041	0.041
Helix OD (Inch)	0.053	0.053	0.053
Output Circuit			
Helix Support Material	Diamond	Diamond	Diamond
Helix Pitch (Inch)	Linear Taper	Linear Taper	Exponential Taper
Taper Length (Inch)	1.6	1.4	2.0
Total Clean Length (Inch)	1.9	2.5	3.0
Helix ID (Inch)	0.041	0.041	0.041
Helix OD (Inch)	0.053	0.053	0.053
4-Stage Poco Collector			
Textured	No	Yes	Yes
4th Stage Spike Length (Inch)	0.422	0.172	0.172

Based on the DVT program's most recent spent beam prediction for SN-2, the collector design was re-evaluated using the Hermannsfeldt program. After several iterations it was concluded that although a reduction in the first stage to collector face distance was not advantageous, reducing the fourth stage spike by 0.25 inch would improve overall efficiency. Consequently, SN-2's fourth stage spike length was reduced relative to SN-1.

The collector electrodes in all three TWTs were fabricated from POCO graphite. POCO is an isotropic graphite material, manufactured by POCO Graphite, Inc. As explained in the design section, isotropic graphite was chosen to reduce back-streaming from the collector. In addition, to further reduce secondary electron emission the electrodes in SN-2 and SN-3 were textured. Texturing is a process where a random array of spires (a few microns in size) are created by ion bombardment. Secondaries are emitted as the primary beam electrons

collide with the electrode surface but due to the geometry of the spires the secondaries are repeatedly intercepted by other electrons.

In summary, the following changes were made from SN-1 to SN-2:

- output circuit gain length increased 0.6 inch
- helix taper length was reduced 0.2 inch
- collector spike length decreased 0.3 inch
- POCO stages textured

SN-2 had very good RF performance, but the goal of 60 percent overall efficiency was not met. Historically at EDD, the DVT program had predicted one to two percent points lower than actual TWT results. In this case, the DVT program prediction was on the average seven percent higher than actual TWT results. Review of the input parameters used to design SN-1 and SN-2's DVT helix revealed an incorrect beam size. After the appropriate corrections were made to the DVT program, SN-3's output helix was redesigned. Details regarding the circuit design problem are found in Section 3.3.1.2.

SN-2's RF performance (43 dB of gain and 54.6 percent overall efficiency) confirmed that the excessive loss found in SN-1's output circuit was eliminated by applying the appropriate correction factors. However, the high loss in SN-1 masked a second problem. The loss pattern produced by the TiC sputtering fixture was too abrupt. Specifically, the transition from the shallow loss pattern to the deep pattern was not smooth. The abrupt change in slope created a reflection or mismatch which was amplified through regeneration affects. The problem surfaced as high ripple in the cold VSWR data for the output circuit.

It was decided to repair the output circuit. This allowed verification of the circuit redesign effort in a timely fashion and at a reasonable cost to the program. In addition, the alternative to rework SN-2 with a new output circuit at a later date was still a possibility. The network entailed the addition of lossy material onto the diamond attenuation pattern. Aguedag, which is an agueous colloidal suspension of graphite, was applied to the diamond rod with a very small custom made brush. The ripple was not eliminated but the amplitude was substantially reduced. As expected, a higher than normal VSWR did result in SN-2, but the TWT was stable.

Only the output helix design was changed from SN-2 to SN-3 as follows:

- helix taper from linear to exponential
- taper length increase of 0.6 inch

Unfortunately the following unintended changes were also made:

- input circuit gain length decreased
- output circuit gain length increased 0.5 inch

The increased attenuation in the input circuit is not understood. Destructive physical analysis of the input circuit is necessary to positively identify the cause, but it appears that the rods were not cut correctly. This problem could have been prevented if the input BeO rods had been measured after the final cut. The output circuit, on the other hand, experienced an increase in gain length. This change was made inadvertently during the output circuit rework and it could have been avoided if a new set of diamond rods had been used. In addition, the loss measurement equipment should be modified to set a constant "zero" reference level.

When constructing an output circuit, the longest diamond sections were always placed at the end of the composite diamond support rod. This was done because of the high stress concentration at either end of the circuit. SN-1's and SN-2's end diamonds were about 0.28 to 0.35 inch long. Due to a limited amount of diamonds, SN-3 was constructed with diamonds that were at the most 0.17 inch long. SN-3 was assembled and coined into a glidcop sleeve uneventfully. Unfortunately, when the initial cold matching began the three end diamonds on the window side became dislodged. The combination of shorter diamonds and slight flaring in the inner diameter of the glidcop sleeve (caused by honing) allowed the diamonds to come loose. Due to a lack of parts the output circuit was reworked instead of fabricating an entirely new circuit. Rework entailed potting the entire circuit and cutting it open in such a manner that the diamonds sections could be salvaged. The diamonds were removed one at a time and reset on the bonding fixture but an error was made causing the 0.5 inch increase in clean length.

There was high confidence on SN-3's output helix design, but the increased clean length caused oscillations which made the tube unstable. To correctly evaluate that circuit a new vacuum assembly should be built.

5.0 TWT Test Results

Salient test results were (1) the demonstration of long term thermal stability of the diamond circuit and (2) an all time high of 54.6 percent overall efficiency at K-band frequencies. The thermal stability was demonstrated on two breadboard type vacuum assemblies. Output power of 100 W was stable with no degradation, even after extended operation, confirming the RF and thermal capability of the 5-mil diamond supported helix circuit.

The 54.6 percent overall efficiency can be compared to 48.2 percent; the maximum recorded efficiency in the past. This new high was achieved at about 10 kV with a gun perveance of 0.059 microperv. Saturated gain was 42 dB, electronic efficiency was 16.8 percent, and AM/PM was 2.7°/dB.

5.1 SERIAL NUMBER 1

Specific test results by Serial Number (SN) are listed in Table 5-1. The first model as shown on Table 5-1 achieved only a 44 percent overall efficiency due to a low electronic efficiency. The low electronic efficiency was caused by an excessive amount of loss. This lack of gain or high loss in the output section resulted in low output power due to inadequate modulation of the beam. Without proper beam modulation optimal energy transfer does not occur. The electrons transfer energy to the growing forward wave but, additional interaction area (clean length) is needed to maximize beam interaction. The effect of insufficient output gain is further illustrated by Figure 5-1. Efficiency and gain are plotted against beam current and as gain is increased efficiency increases rapidly. Overall and basic efficiency for SN-1 are then plotted versus frequency in Figure 5-2. Figure 5-3 lists the specific operating voltages

TABLE 5-1
SUMMARY OF BREADBOARD TWT TEST RESULTS AT 17.7 GHz

Description	Goal	SN 1	SN 2	SN 3
Cathode Voltage (kV)	9.7	9.78	10.05	10.04
Cathode Current (mA)	51.0	87.0	61.2	65.8
Output Power (W)	94.0	101.0	103.7	112.0
Gain (dB)	40.0	39.0	43.0	33.0
Beam Efficiency (%)	19.0	11.9	16.8	17.0
Overall Efficiency (%)	60.0	44.0	54.6	48.7

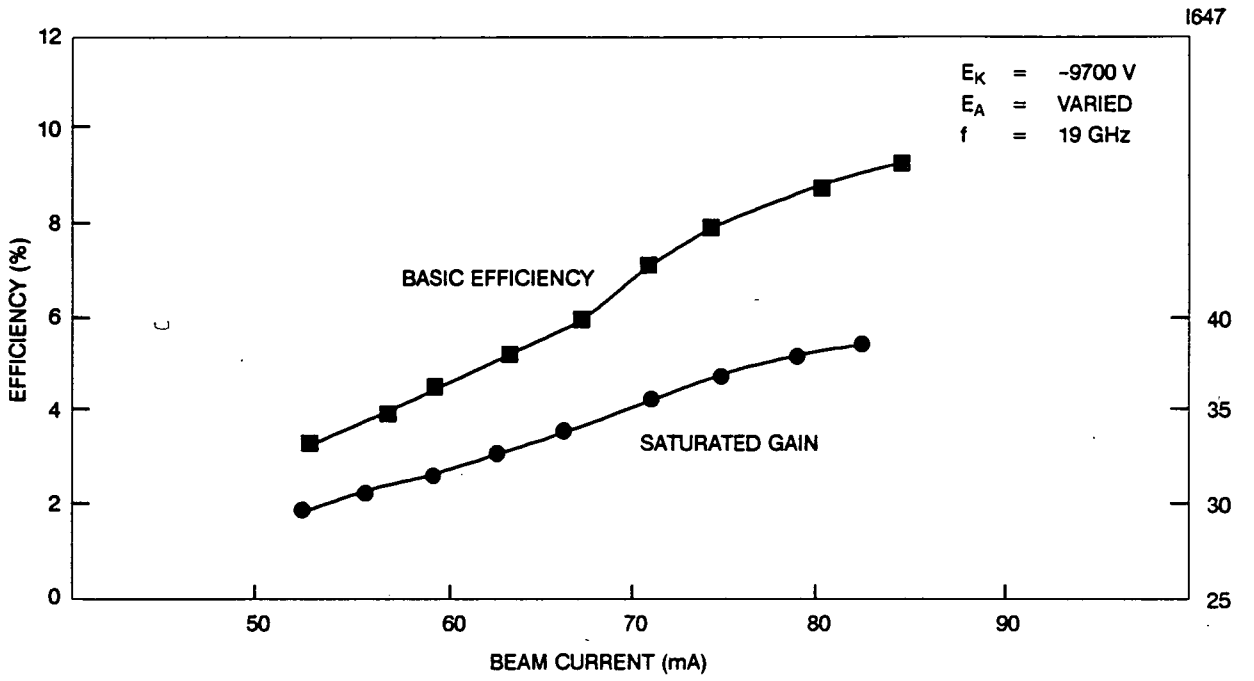

Figure 5-1 953H Breadboard TWT SN-1 effect of insufficient output gain.

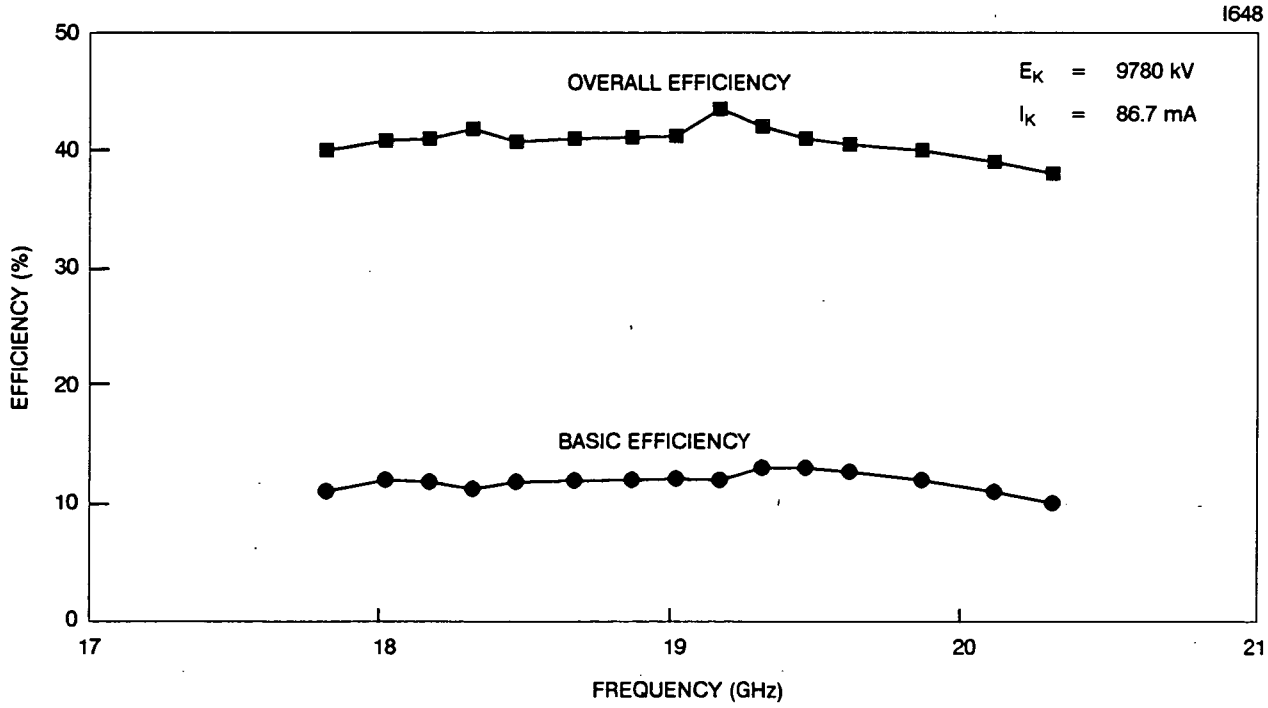

Figure 5-2 953H Breadboard TWT SN-1.

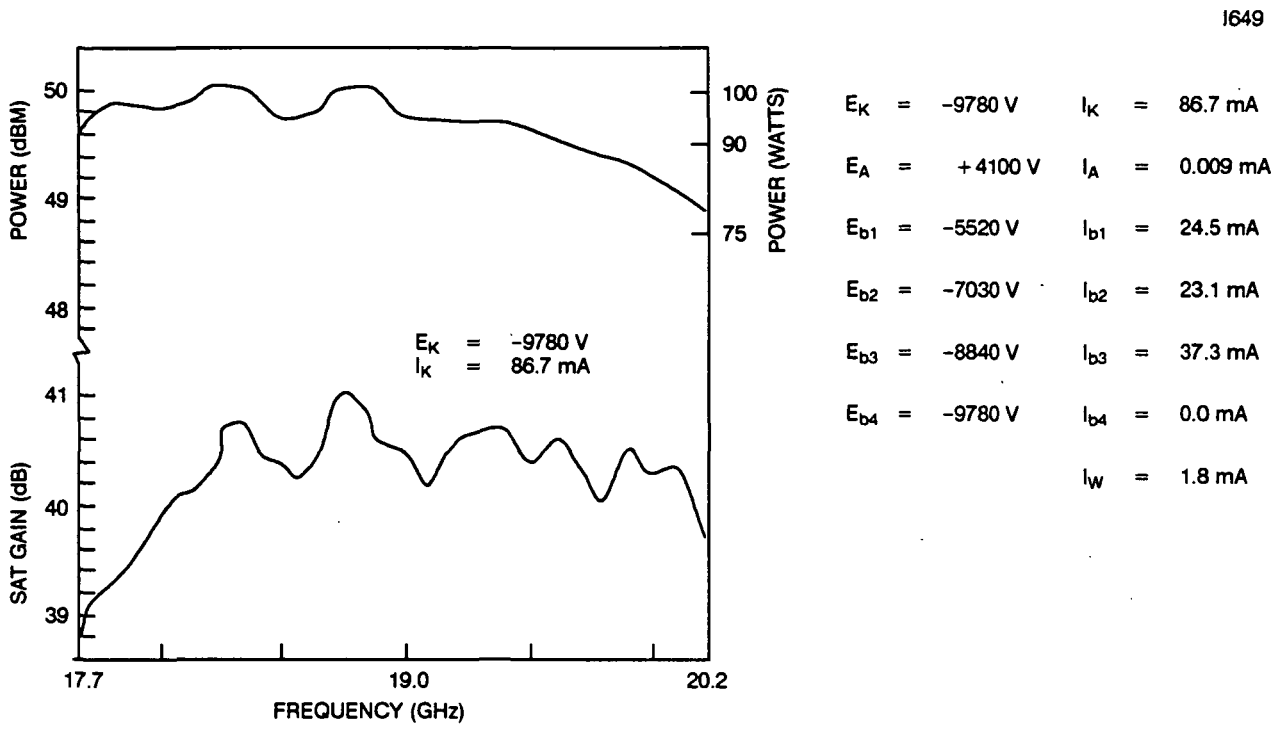

Figure 5-3 953H TWT SN1 output power and gain characteristics.

and currents next to a plot of saturated output power and saturated gain. SN-1 achieved 100 W of output power and was operated at this power level for an extended period of time with no degradation.

SN-1's test performance can be summarized as follows:

- Good beam transmission
- Stable BWO free operation
- Thermal and RF stability in a diamond circuit at 100 watts CW power output
- 75 watts CW power across desired frequency band
- Output circuit section required more gain to boost efficiency
- Highest overall efficiency achieved was 44 percent

5.2 SERIAL NUMBER 2

The significant change from SN-1 to SN-2 was an increase in the clean length. As is evident from Table 5-1 and Figure 5-4, both the electronic efficiency and the overall efficiency

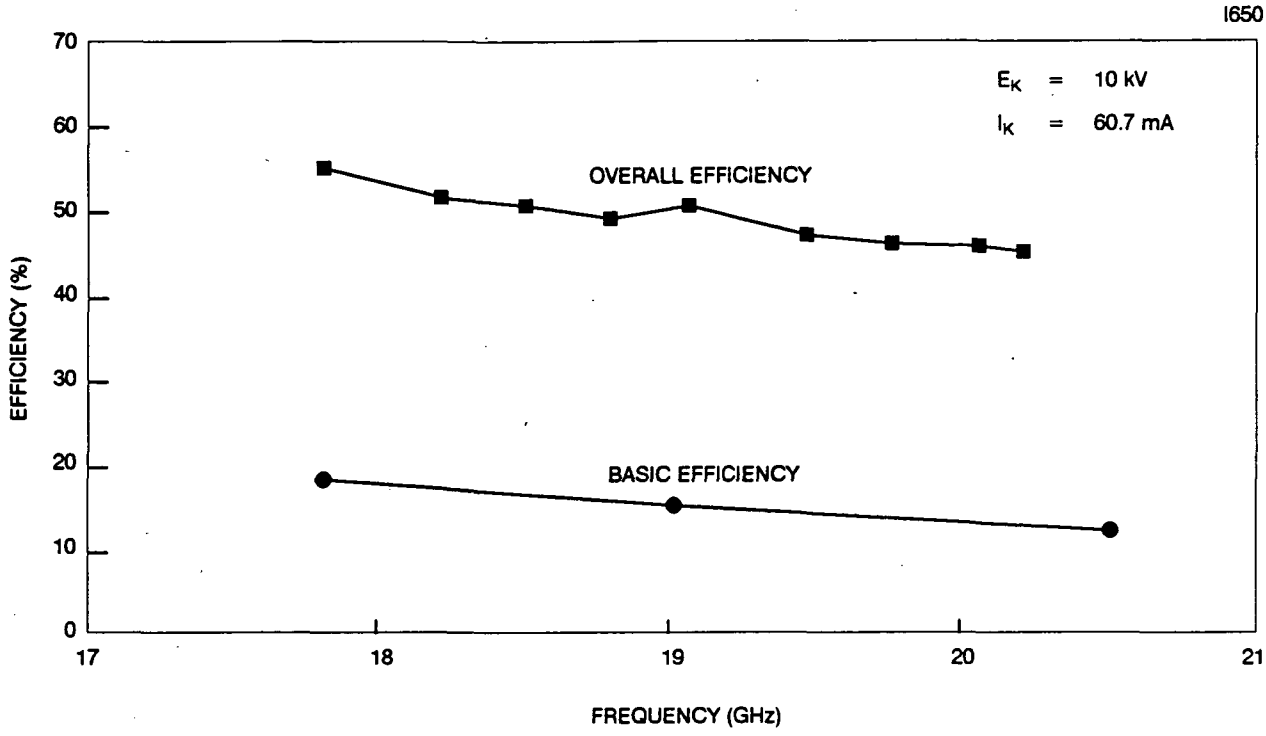

Figure 5-4 953H TWT SN-2 efficiency characteristics.

improved considerably. The operating voltages and currents for SN-2 are found in Figure 5-5. From the plot of saturated power and gain versus frequency. It is evident that the highest efficiency is at 17.7 GHz. A reduction in the shield diameter for SN-3 would have centered performance. However, a new output helix was already being incorporated and in order to clearly evaluate the new DVT design it was decided not to introduce other variables.

The overall efficiency achieved was exceptional for SN-2 but the 60 percent goal was not met. The design process was reviewed and an error in the DVT model was isolated. After the computer model was revised the DVT program predictions closely correlate with SN-2's measured performance. To ascertain the optimum output clean length, electronic efficiency versus beam current was also taken on SN-2. From the data in Figure 5-6 it was concluded that additional clean length was needed to maximize the basic efficiency.

SN-2's test performance can be summarized as follows:

- Good beam transmission
- Thermal and RF stability of diamond circuit at 104 watts CW power
- Highest power and efficiency at 17.7 GHz (tube band centered low)

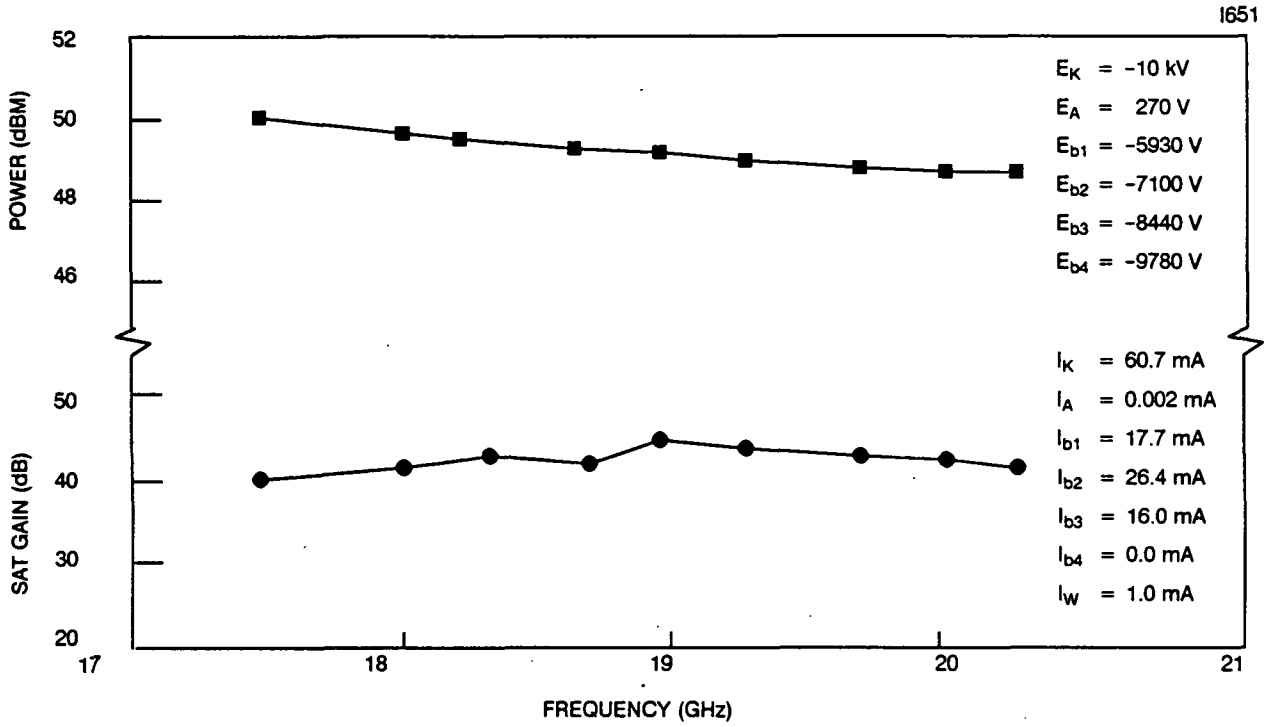

Figure 5-5 953H TWT SN-2 output power and gain characteristics.

- High small signal gain ripple (output attenuator pattern too abrupt)
- Circuit efficiency increased further by increasing output gain
- Highest efficiency achieved was 54.6 percent

5.3 SERIAL NUMBER 3

Using the improved DVT model, SN-3's helix design was then optimized and should have reached 20 percent electronic efficiency. SN-3, however, resulted in 17 percent electronic efficiency, as is illustrated in Figure 5-7 where efficiency is plotted versus frequency. Oscillations in the output circuit also were present at small signals which made the evaluation more difficult. The oscillations were caused by an excessive amount of clean length, a result of circuit rework. Details regarding the operating voltages and currents for SN-3 are found in Figure 5-8 along with a plot of saturated power and gain.

SN-3 had low resistance between the second and third stage electrodes, approximately 6 MΩ. The collector was X-rayed in efforts to ascertain the problem, but the resolution was poor and no conclusions could be made. In preparing SN-2 for shipment to NASA, it was discovered that the previously low current leakage recorded in the collector had increased to SN-3's level. The leakage was definitely not there from when SN-2 was being tested. SN-1

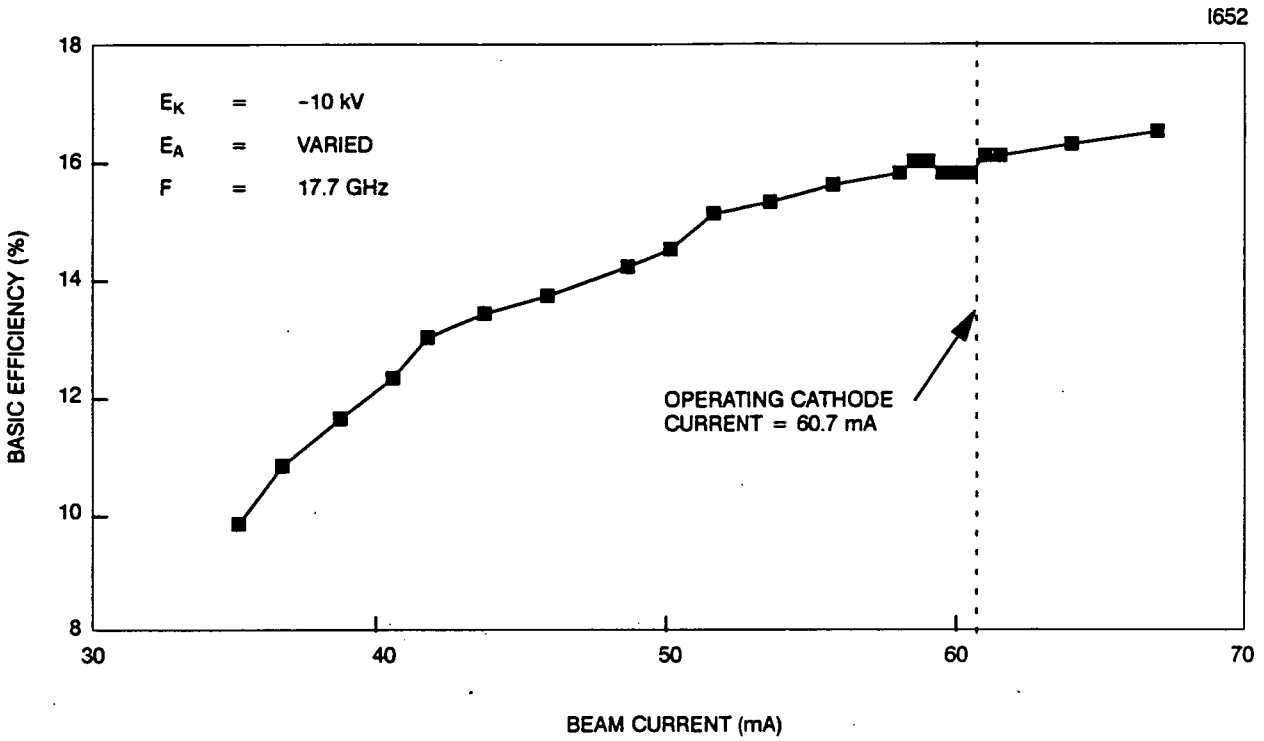

Figure 5-6 953H TWT SN-2 basic efficiency versus beam current.

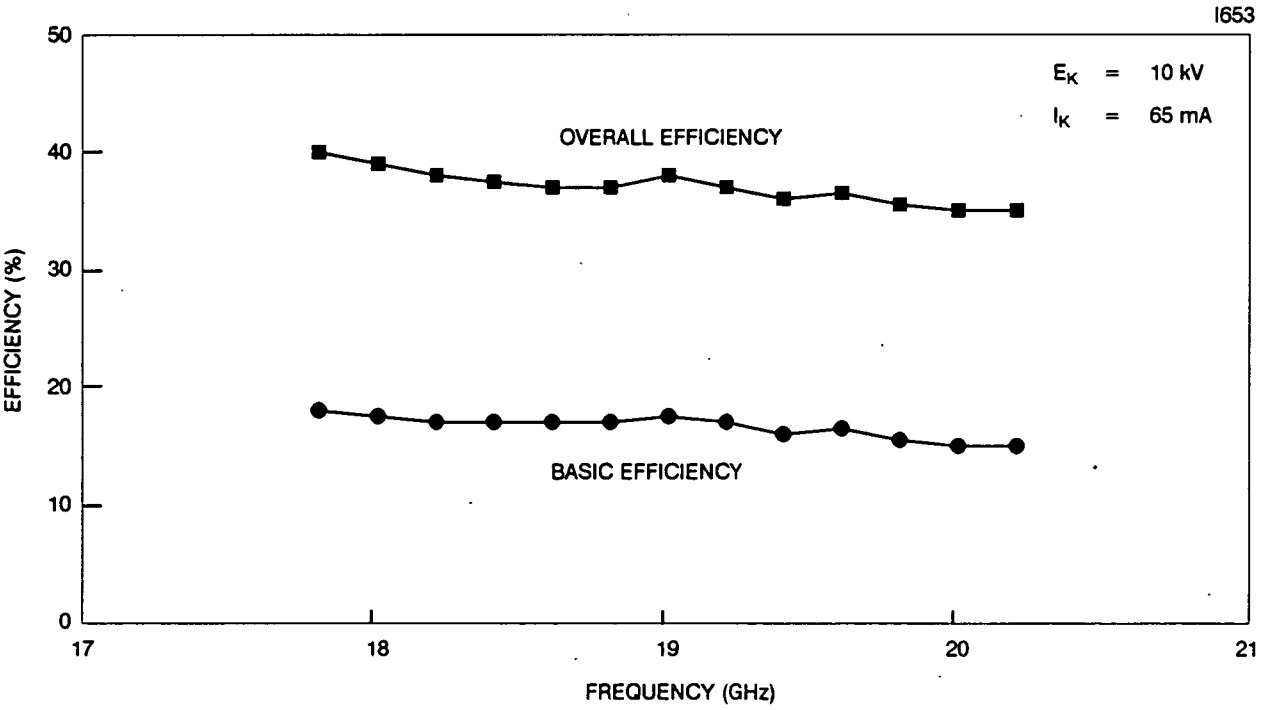

Figure 5-7 953H TWT SN-3 efficiency characteristics.

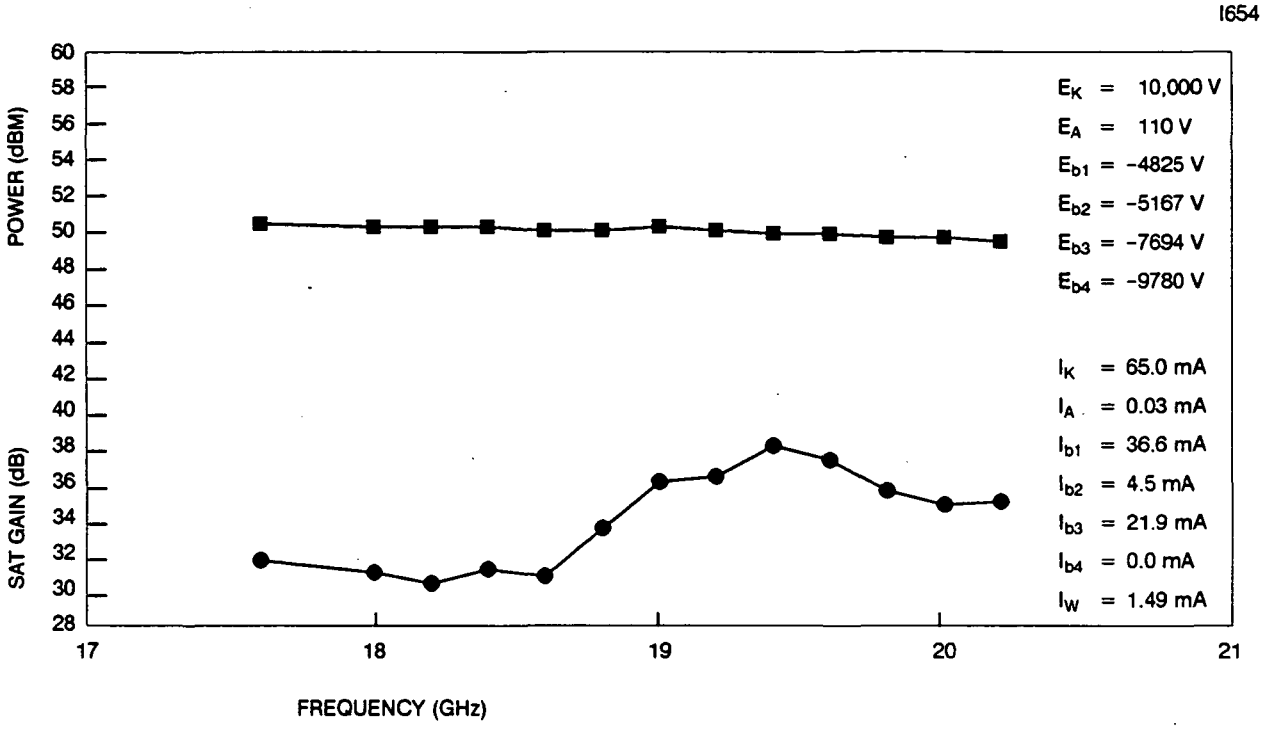

Figure 5-8 953H TWT SN-3 output power and gain characteristics.

was also retested but no change in the leakage current was detected. Whether it is significant that both SN-2 and SN-3 had textured electrodes is not known. However, there is concern with the spires possibly breaking or collapsing and forming a leakage path.

In conclusion, SN-3's performance can be summarized as follows:

- Good beam transmission
- Thermal stability of diamond circuit at 112 watts CW power
- 75 watts CW power across desired frequency band
- Highest electronic efficiency was 17 percent
- Low overall gain (input gain too low)
- Output unstable at small signal (output gain too high)
- High leakage current (6 mA) after bakeout between third and fourth collector stages affected overall efficiency
- Highest efficiency achieved was 48.7 percent

6.0 CONCLUSIONS AND RECOMMENDATIONS

6.1 CONCLUSIONS

The 953H TWT achieved an overall efficiency of 54.6 percent, which is a new benchmark in TWT technology for K-band devices. This high efficiency was obtained by utilizing state-of-the-art technologies. Technology areas included circuit design (Dynamic Velocity Tapers), materials (diamond, graphite, dispersion hardened copper), processes (electron beam sputtering), new assembly techniques (cold compression circuits), and highly improved finite element analyses (mechanical, thermal, and electrical). These technologies were integrated into a single TWT design for the first time under this program.

Manufacturing techniques developed have significantly advanced diamond rod technology. A newly developed cold compression technique for assembling the helix circuit replaced heat shrinking and the eliminated high temperatures associated with the process. This helix design demonstrated excellent thermal capabilities by handling in excess of 100 watts of CW power, at 20 GHz. This technique has not only proven successful in eliminating power fade problems experienced in the past, but will also open the door to other helix support material that can only be manufactured in small segments.

To further illustrate the accomplishments of this program, Table 6-1 shows a comparison of similar K-band TWTs and the efficiency improvements that have occurred due to recent TWT technology advancements. The first column lists results for a K-band TWT with uniform helix pitch and beryllia support rods. In the second column, incorporation of the Dynamic Velocity Tapered (DVT) helix improved beam conversion efficiency by almost 5 percent (from 7.3 to 12.2 percent). The third column, an additional 4.7 percent (from 12.2 to 16.9 percent) has been gained using diamond support rods. Overall efficiency also influenced by the collector design improved substantially in each case.

6.2 RECOMMENDATIONS

Additional units should be built to determine the true performance capabilities of SN-3's configuration. SN-3's exponential tapered helix produced a higher basic efficiency than SN-2's linear tapered design, thus overall efficiency for the final configuration should be higher than 54.6 percent. The leakage current in the SN-3's collector prevented verification of the overall efficiency.

Considering the exorbitant cost of segmented diamond support rods, other types of materials should be investigated to support the helix. Possibilities include cubic boron nitride, Beramic Z, or possibly, utilization of diamond deposition to form a long hollow rod.

TABLE 6-1
TWT EFFICIENCY IMPROVEMENTS

Parameter	1984	1985	1986
	918HA* Uniform Pitch Helix, Beryllia Supports	918HA* DVT Helix, Berryllia Supports	953H** DVT Helix Diamond Supports
Cathode Voltage	10.8 kV	9.74 kV	10.05 kV
Cathode Current	71.7 mA	61.9 mA	61.2 mA
Saturated Output Power	56.2 W	73.3 W	103.7 W
Saturated Gain	40.0 dB	44.6 dB	42.0 dB
Beam Conversion Efficiency	7.3%	12.2%	16.9%
Overall TWT Efficiency	42.5%	48.2%	54.6%

1656

*Five-stage TiC coated copper collector

**Four-stage poco collector

Sixty percent efficiency can be achieved with the 953H design. However, additional refinements may be needed. For example, a potential design improvement is to explore other velocity tapered helix configurations, such as the GVT. Recently, GVT designs at Hughes have produced higher basic efficiencies than the DVT in addition to exhibiting very good correlation between predicted and measured TWT performance. Another area for improvement is the multi-stage collector. The present 953H collector configuration is the first-cut design. Potentially the collectors efficiency can be improved by optimizing the electrode geometry and position. Lastly, the structural integrity or shock resistance of textured graphite (spires) should be investigated.

APPENDIX A

953H TRAVELING-WAVE TUBE

DIAMOND CIRCUIT MECHANICAL ANALYSIS

953H TRAVELING-WAVE TUBE DIAMOND CIRCUIT MECHANICAL ANALYSIS

CONTRACT NO. NAS3-24897

NOVEMBER 1988

PREPARED BY: Kirk Norenberg 9-7-88
K. A. NORENBERG DATE
MEMBER OF THE TECHNICAL STAFF
MECHANICAL ENGINEERING

APPROVED BY: M. Filler 9-9-88
M. FILLER DATE
PROJECT MANAGER
MECHANICAL ENGINEERING

APPROVED BY: R.N. Tamashiro 9-9-88
R. N. TAMASHIRO DATE
PROGRAM MANAGER
SPACE TUBE AND DEVELOPMENT DEPARTMENT

HUGHES AIRCRAFT COMPANY
ELECTRON DYNAMICS DIVISION
3100 WEST LOMITA BOULEVARD
P.O. BOX 2999
TORRANCE, CA 90509-2999

Page Intentionally Left Blank

TABLE OF CONTENTS

LIST OF ILLUSTRATIONS

LIST OF TABLES

1.0 INTRODUCTION

The design of the output circuit of the 953H TWT is distinguished from others by the use of diamond support rods. This output circuit will be assembled by a coining technique, a relatively new alternative to the heatshrink assembly process. A combined structural and thermal analysis has been performed to investigate the fabrication procedure and to determine the temperature distribution in the output circuit during operation. The predicted temperatures are used to judge the ability of the design to handle the required thermal loads. The primary design limit requires that the peak helix temperature must be below 300°C. This criterion is very conservative and was chosen to ensure good electrical performance of the circuit.

Two cross-sectional views of the output circuit are shown in Figures 1 and 2. The helix has a pitch of 0.0276 inch except over the last 1.60 inches of the circuit, where it linearly decreases to 0.0243 inch at the helix termination. The helix is made of a tape 0.015 inch wide and 0.006 inch thick. Each support rod is composed of segments that are typically 0.150 inch long (0.118 minimum). Each segment is 0.030 inch high and 0.005 inch wide. The sleeve is 0.030 inch thick. The original design called for a copper sleeve, but the use of GlidCop was also analyzed. GlidCop is a dispersion-strengthened copper consisting of high purity copper and a very small percentage of aluminum oxide.

The ANSYS finite element computer code was used for this analysis. Several steps were performed to determine the temperature distribution. A structural analysis was used to predict the contact areas and pressures at the helix/rod and rod/sleeve interfaces. Empirical data was used to find the thermal interface coefficients associated with the pressures. The contact areas and interface coefficients were used as inputs to a thermal analysis of the circuit. The resulting temperatures were used to revise the structural analysis. These steps were repeated until the results of the thermal analysis agreed with the temperature inputs to the structural analysis.

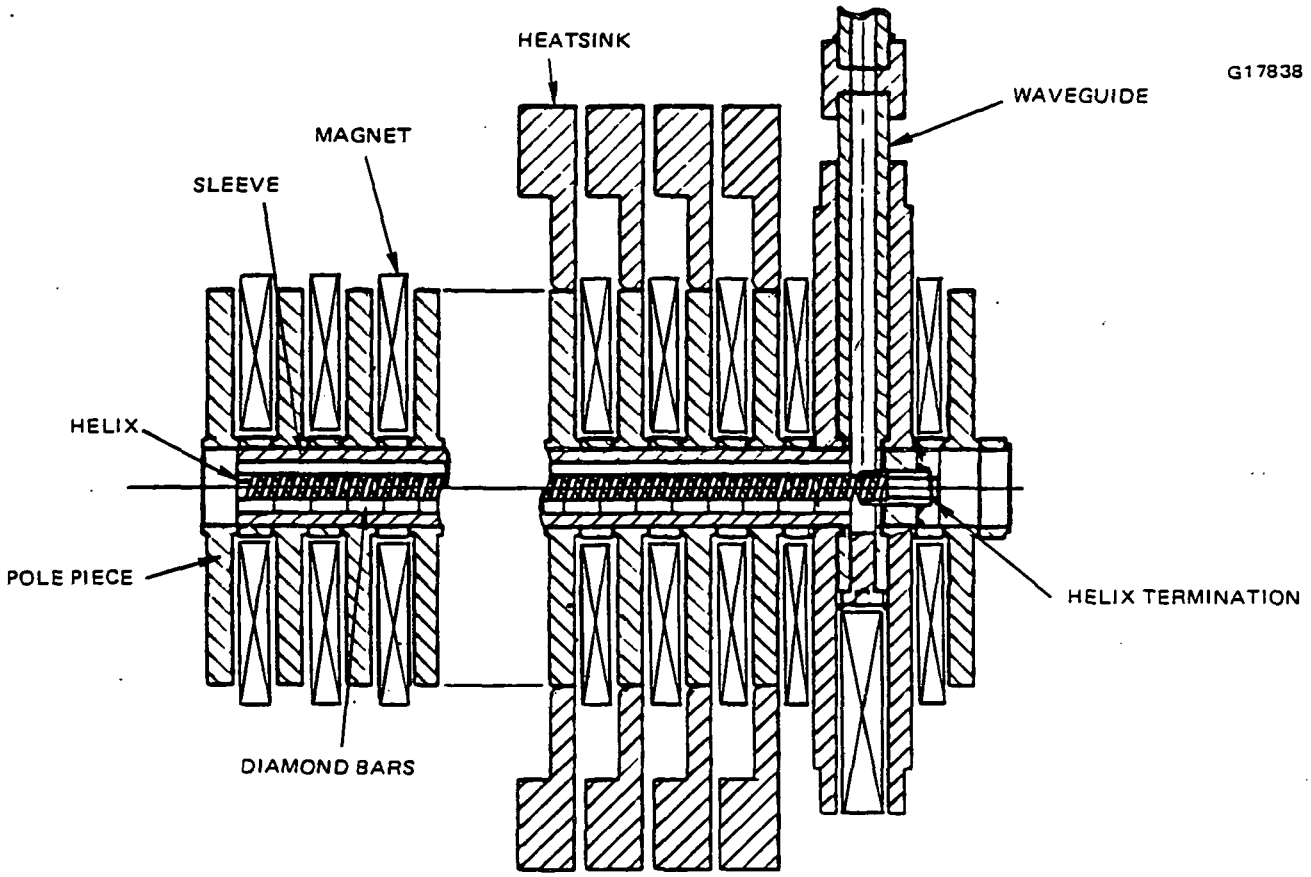

Figure 1 Cross section of 953H output circuit (top view).

G17839

NOTE: DRAWING IS NOT TO SCALE.

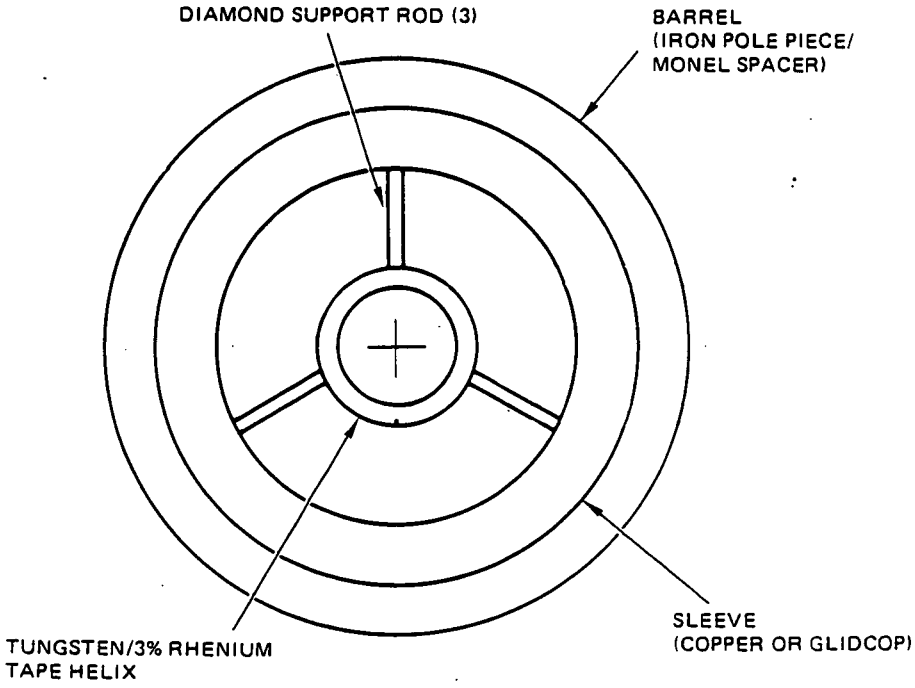

Figure 2 Cross section of 953H output circuit (axial view).

2.0 STRUCTURAL ANALYSIS

The first phase of the structural analysis was the investigation of the coining procedure. The next phase began with the analysis of the bakeout process during which the vacuum assembly is held at 500°C for two to three days. This was followed by an analysis of the initial operating condition.

The physical phenomena associated with coining, bakeout, and operation are very complicated and would be best simulated with a three-dimensional (3–D) finite element model. However, this was not feasible because of the limitation of the computing resources available at HEDD. Therefore, a two-dimensional (2–D) model was used for all phases of the structural analysis (Figure 3). The model consists of 634 nodes and 565 elements. Close-ups of the helix/rod and rod/sleeve interfaces are shown in Figures 4 and 5. A 60-degree slice with tangential constraints on the edges was modeled to take advantage of the symmetry of the assembly. (The treatment of the asymmetry of the helix is discussed in later sections.) These symmetry boundary conditions have the effect of preventing slippage at the interfaces. This constraint is reasonable since the rod is expected to grab and dig into the helix coating and sleeve. The copper coating on the helix was assumed to be 0.0003 inch thick. The barrel was represented by a combination of electrolytic iron and Monel 404 with an outer diameter approximately the same size as that of the spacer. The gold plating on the outer diameter of the sleeve was not treated as a separate material.

The finite element formulations used in this analysis are based on small strain and small displacement conditions. The von Mises yield criterion and the Prandtl-Reuss flow equations were used to govern plasticity. Bilinear stress-strain curves were used for the metallic components. Initially, the kinematic hardening rule was used for all of the metals. However, it became necessary to switch to the isotropic hardening rule for the sleeve and helix coating during the coining analysis. This is further discussed in the next section. The initial stress method was used to solve the nonlinear equations associated with plasticity. This method involves iterative modification of the load vector while the stiffness matrix remains unchanged.[1]

The material properties used in the structural analysis are given in Table 1. The properties for pure tungsten were used for the tungsten alloy. The thermal expansion coefficient for GlidCop was taken as the average of reported data and assumed to be constant with temperature. The temperature-dependence of the GlidCop stress-strain curve was assumed to be the same as that of copper. The ratios between the tangent modulus and elastic modulus for the metals were chosen to correspond to approximately 5 percent strain.

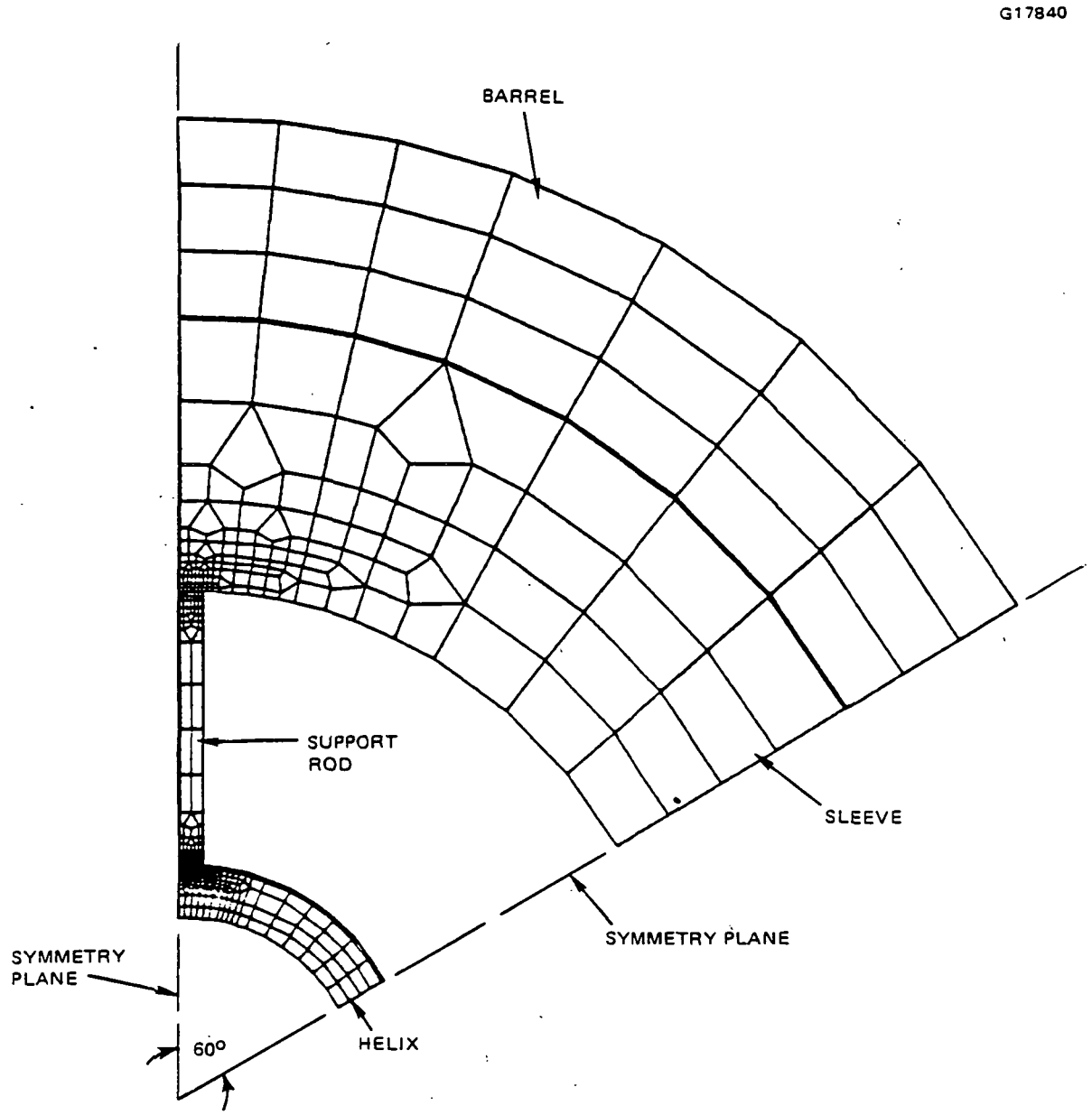

Figure 3 2-D finite element model of the 953H output circuit.

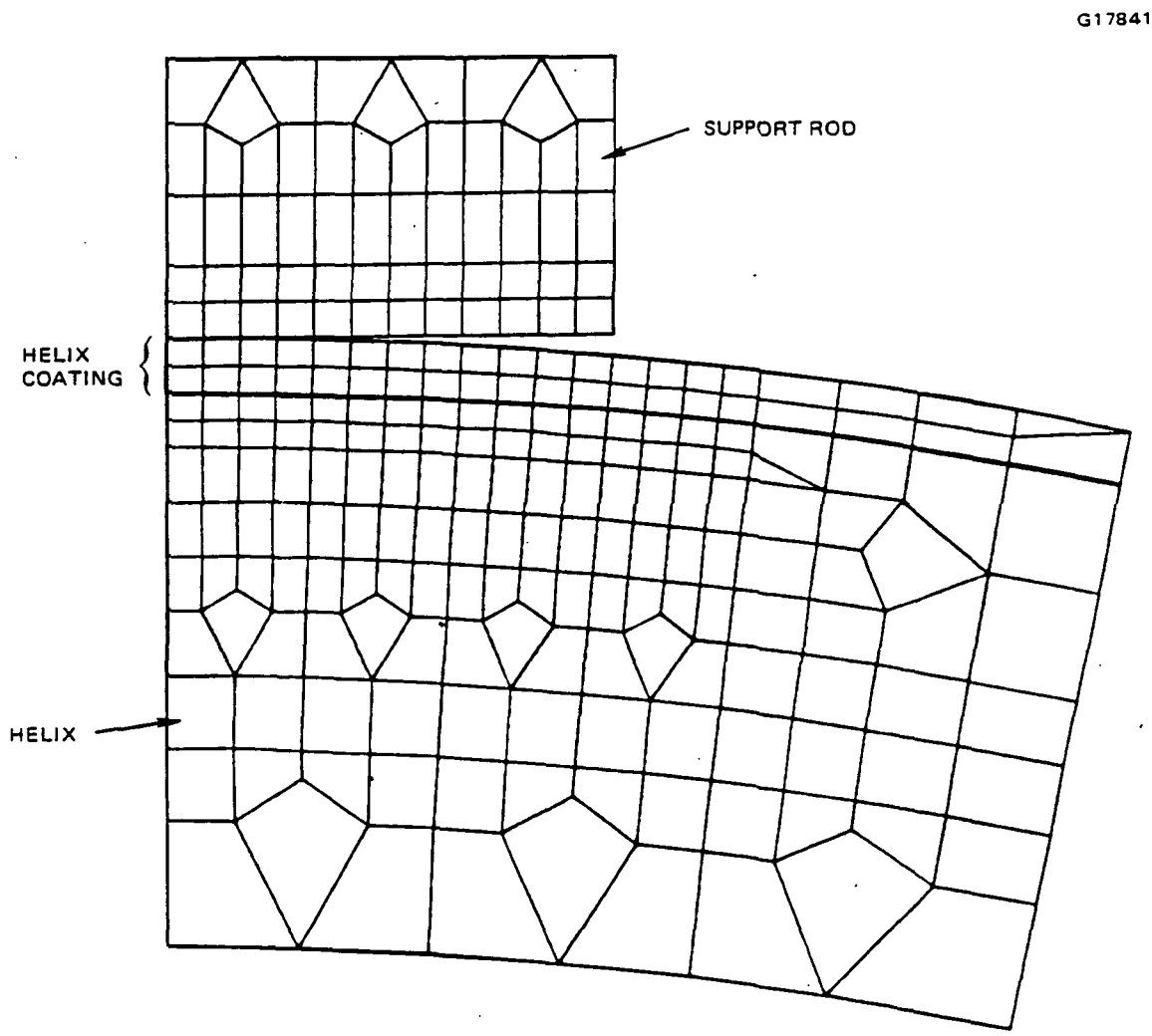

Figure 4 Close-up of the helix/rod interface.

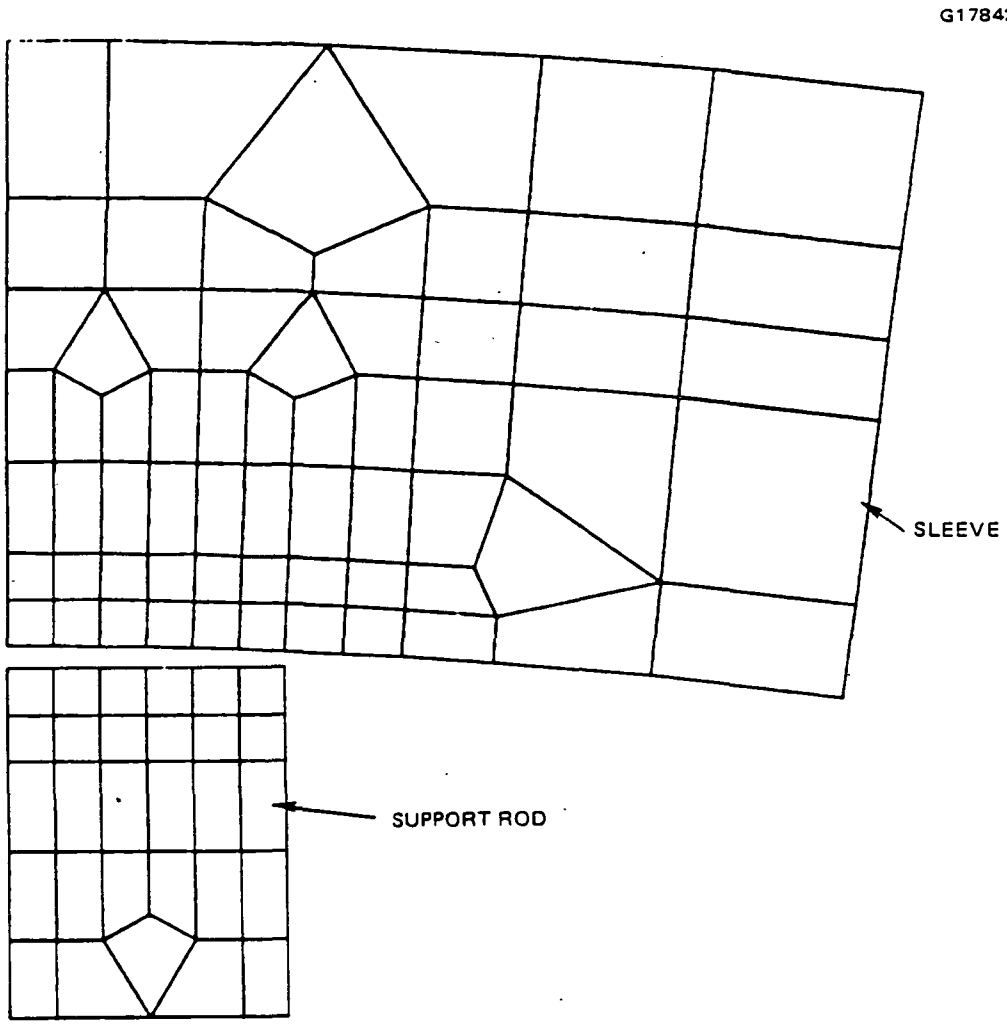

Figure 5 Close-up of the rod/sleeve interface.

TABLE 1
MATERIAL PROPERTIES USED IN STRUCTURAL ANALYSIS

Material	Temperature (°C)	Elastic Modulus (10^6psi)	Tangent Modulus (10^6psi)	Yield Strength (10^3psi)	Thermal Expansion Coefficient* (10^{-6} in/in-°C)	Poisson's Ratio
97% Tungsten/ 3% Rhenium	25	59	1.65	380	4.44	0.284
	200	59	1.65	310	4.5	0.284
	400	59	1.65	285	4.6	0.284
	600	59	1.65	214	4.7	0.284
Diamond IIA	25	153	–	–	1.05	0.20
	200	153	–	–	1.70	0.20
	400	153	–	–	2.39	0.20
	600	153	–	–	2.86	0.20
OFHC Copper	25	18.0	0.378	6	14.3	0.33
	200	17.5	0.368	6	15.4	0.33
	400	15.7	0.330	5	17.3	0.33
	600	13.2	0.277	3	18.8	0.33
GlidCop AL–15	25	16.0	0.448	47	18.1	0.33
	200	15.6	0.437	47	18.1	0.33
	400	14.0	0.392	39	18.1	0.33
	600	11.7	0.328	24	18.1	0.33
Barrel **	25	26.7	0.748	20.6	13.2	0.29
	200	25.2	0.706	23.7	14.3	0.29
	400	22.9	0.641	18.3	15.8	0.29
	600	20.0	0.560	11.0	16.5	0.29

* Based on a reference temperature of 25°C.
** Combination of electrolytic iron and Monel 404.

2.1 COINING OPERATION

The coining operation is the process by which the helix/rod and rod/sleeve interfaces are put into compression. The helix and support rods are first inserted into the sleeve. The sleeve is then placed in the die and compressed with a force of approximately 20 tons.

The 2–D plane strain assumption was used for the analysis of the coining operation. This caused the axial motion of the elements to be constrained in the out-of-plane (axial) direction. This assumption is reasonable because the friction between the die and the sleeve should tend to restrain the axial motion. One disadvantage of using a 2–D model is that it represented the helix as a hollow cylinder. In an attempt to account for the 3–D effect of the helix, the resultant rod/sleeve contact pressures were scaled by one half. This was based on a helix width of 0.015 inch and an initial pitch estimate of 0.030 inch.

At this stage of the analysis, the sleeve was assumed to be made of copper. Preliminary coining experiments indicated that the load imposed by the die was essentially axisymmetric. Since the die is very stiff in comparison to the sleeve, the loading was treated in the analysis as a uniform enforced radial displacement at the outer diameter of the sleeve. The nodes in the model representing the outer diameter were connected to dummy nodes by interface (gap) elements. These elements act as stiff radial springs in compression, but carry essentially no load in tension. The loading by the die was implemented by incrementally increasing enforced displacements on the dummy nodes up to a final value of 0.00105 inch. This incremental approach was necessary because of the use of nonlinear stress-strain curves for the metallic components. Plasticity is a nonconservative phenomenon that requires a reasonably accurate description of the load history. During unloading, the enforced displacements were incrementally decreased until the compression was removed from all of the interface elements. At this point, the model represented the coined assembly after removal from the die.

Gap elements were also used between the pairs of nodes at the component interfaces. The resultant contact areas were found by determining which gaps had closed. The compressive loads carried by the individual gap elements were summed to determine the total interface forces. The reported contact pressures represent average values for each interface.

The kinematic hardening rule was used for the metallic components in a preliminary analysis of the coining operation. During the loading phase of the coining, very large plastic strains developed in the helix coating and sleeve. The tangent modulus of copper decreases a great deal as the strain increases, so the use of a bilinear stress-strain curve led to results that underestimated the strain and overestimated the stress. Although the use of a lower tangent modulus was considered, it was rejected because of the difficulty in reaching a

converged solution. Since the stress was well above twice the yield strength in many elements, the use of the kinematic hardening rule led to a prediction of additional plastic strain upon unloading. The resultant interface force was also unreasonably low. These results were not considered to be physically realistic, so a switch was made to isotropic hardening in the coating and sleeve for unloading. This prevented the development of additional plastic strain and led to a more reasonable final solution. Since the actual hardening behavior of most metals falls between the kinematic and isotropic assumptions, the use of either can be justified. The advantage of the kinematic hardening rule in ANSYS is that it can account for the temperature-dependence of all the material properties. With isotropic hardening, the yield strength and tangent modulus are assumed to be constant with temperature. This limitation was considered acceptable since most of the important physical phenomena occur below 300°C and the values for copper vary by less than 10 percent over this range.

The results of the final coining analysis are given in Table 2. The helix/rod contact area is reported in square inches for each contact point. The maximum possible contact area is 7.5×10^{-5} in^2 (based on a 0.005-inch rod width and a 0.015-inch helix tape width). The reported values are conservative because the high localized plastic strains that occur during the coining process are not fully developed in this finite element analysis. The rod/sleeve contact area is reported in square inches per inch of length of each rod. Even with the conservative nature of this analysis, the reported values are at the maximum possible, 5.0×10^{-3} in^2/in. The interface force is given in terms of pounds per inch of length of each rod.

TABLE 2
RESULTS OF COINING ANALYSIS

Quantity	Under Full Load From Die	Removed From Die
Helix/rod contact area (in^2/contact point)	5.1×10^{-5}	2.4×10^{-5}
Helix/rod pressure (ksi)	194	115
Rod/sleeve contact area (in^2/in/rod)	5.0×10^{-3}	5.0×10^{-3}
Rod/sleeve pressure (ksi)	66	18
Interface force (lbs/in/rod)	329	92

2.2 BAKEOUT PROCESS

In the bakeout process the vacuum assembly is slowly raised from room temperature to 500°C, held there for two to three days, then slowly brought back to room temperature. Since this loading causes thermal expansion, the constrained axial motion of the plane strain assumption is inappropriate. Therefore, the 2–D plane stress assumption, in which axial motion is unrestrained, was required for the bakeout analysis. An attempt was made to analyze the bakeout process as a continuation of the coining analysis by switching assumptions midstream, but the results were unrealistic and unacceptable. This difficulty arose from the limitation of using a 2–D model to describe all of the physical phenomena associated with the manufacture and operation of the output circuit. In addition, the inability of ANSYS to adequately handle the extremely high plastic strains developed in the coining process is responsible for additional inaccuracy in the subsequent load steps.

In light of this development, the best alternative was to treat the bakeout process as the beginning of a separate analysis. The assembly was assumed to begin stress-free at 500°C with the interfaces barely in contact. This was considered to be a reasonable starting point because of the high creep rate of the copper sleeve and coating. Holding the assembly at 500°C for two to three days should be sufficient to cause the stresses to be very low throughout. The disadvantage of this approach is that it does not account for the flat indentations in the helix coating and sleeve caused by the rods during coining. As a result, the predicted interface areas are probably smaller than the actual areas.

The cooldown to room temperature was simulated by applying uniform temperatures in successive load steps: 450, 400, 325, 250, 175, 100, and 25°C. The temperature gradients within the assembly were ignored because the actual cooling is very slow.

After the completion of the coining analysis, an improvement in the analytical technique was developed. It was found that the 3–D effect could be better represented by modifying the stiffness of the helix. With a helix tape width of 0.015 inch and a pitch of 0.030 inch, the helix should behave as if it is half as stiff as a continuous tube. Therefore, the stress-strain curves for the helix and helix coating materials were scaled down by one half. This change was incorporated into the bakeout analysis. As before, the isotropic hardening rule was used for the helix coating and sleeve while kinematic hardening was used for the helix and barrel.

After analyzing the original design with a copper sleeve, the use of GlidCop as the sleeve material was considered. GlidCop has a much higher yield point than copper and a much lower creep strain rate. These facts suggested that its use would improve the design because the interface forces during operation would be higher and they would be maintained better over a long period of time. The previously mentioned assumptions were also used for the analysis

of the GlidCop sleeve. However, the stress-free initial condition is not as good in this case because of the low creep rate for the sleeve. This assumption makes the analysis more conservative because the interface forces at 500°C are probably quite significant.

The results of the bakeout analysis are given in Table 3. The values represent the condition of the output circuit at room temperature. The use of the GlidCop sleeve results in a much higher interface force, which is responsible for the larger contact area at the helix/rod interface. Despite the higher force, the rod/sleeve contact area with the GlidCop sleeve is below the maximum value. This conflicts with a destructive physical analysis of a thermal test circuit that showed that full contact existed at room temperature. This discrepancy is most likely attributable to the inability to account for the strain history of the sleeve in the coining process.

2.3 INITIAL OPERATING CONDITION

The analysis of the initial operating condition continued from the bakeout analysis. Estimates of the expected operating temperatures were used as loads to the model. To assure proper treatment of the change in load direction, two load steps were used to reach the final temperatures. The applied temperatures were uniform over each component. This was reasonable since the radial temperature gradient within each component should be small. The copper sleeve and GlidCop sleeve cases were both considered.

TABLE 3
RESULTS OF BAKEOUT ANALYSIS
(ROOM TEMPERATURE)

Quantity	With Copper Sleeve	With GlidCop Sleeve
Helix/rod contact area (in^2/contact point)	5.1×10^{-5}	6.6×10^{-5}
Helix/rod pressure (ksi)	72	119
Rod/sleeve contact area (in^2/in/rod)	5.0×10^{-3}	3.4×10^{-3}
Rod/sleeve pressure (ksi)	25	77
Interface force (lbs/in/rod)	123	263

Figure 6 shows empirical data for thermal interface coefficients as a function of pressure. The data for the polished diamond/copper-plated ground tungsten pair was used for the rod/helix interface. The data covers the range from just under 1,000 psi up to 23,000 psi.[2] The interface coefficient seems to approach an asymptote of approximately 50 $W/cm^2-°C$ (323 $W/in^2-°C$). The data for the polished diamond/ground copper pair was used for the rod/copper sleeve interface. This data covers the range from just under 1,000 psi up to 6,000 psi.[3] Linear extrapolation beyond 6,000 psi seems appropriate for moderate pressures. There is no data available for the interface coefficient between polished diamond and Glid-Cop. Since the thermal conductivity of GlidCop is similar to that of copper and the surface roughness is expected to be similar, the hardness is the only significant difference between the two materials. Therefore, the diamond/GlidCop interface coefficient was estimated from the diamond/ground copper data by scaling the pressure axis by the ratio of the yield strengths (47/6). This estimate is very rough, but it is the best available.

The resultant contact pressures from the structural analysis were used to determine the thermal interface coefficients from the empirical data. These coefficients and the resultant

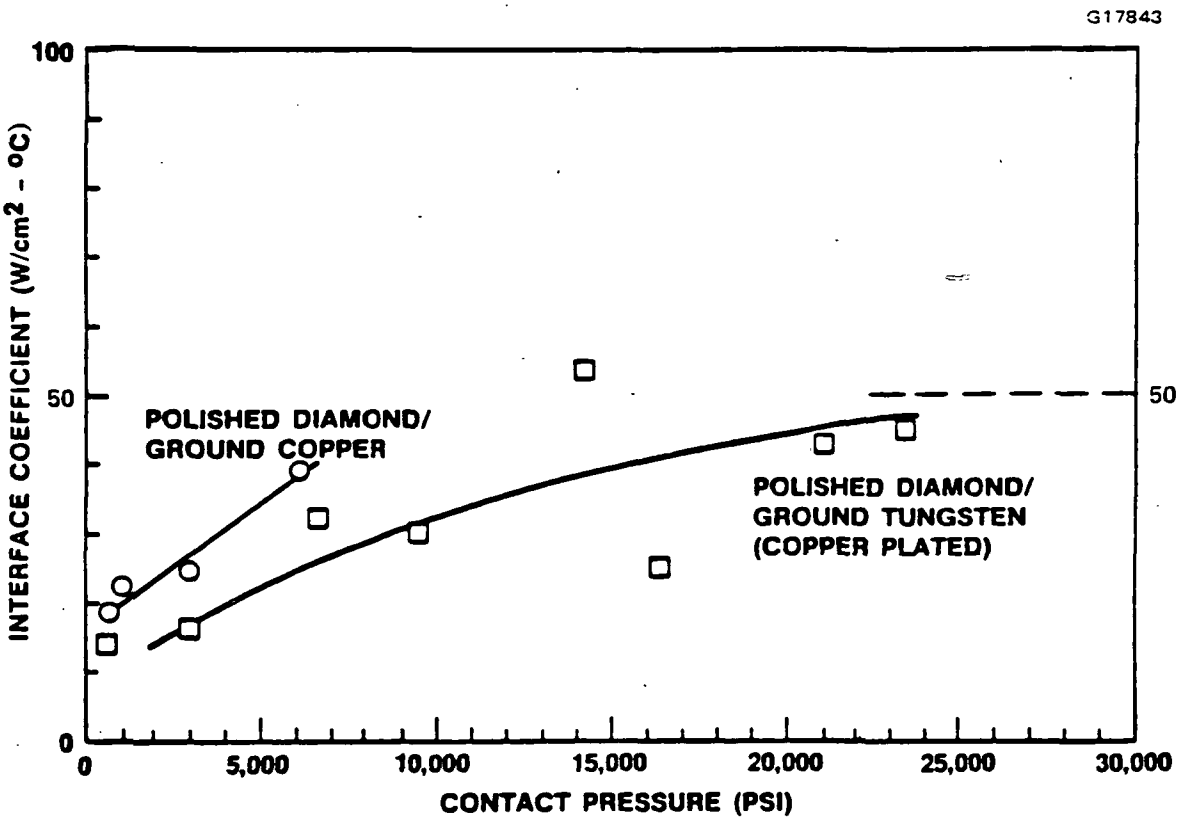

Figure 6 Thermal interface coefficients.

contact areas from the analysis were used as inputs to the thermal analysis (see Section 3.0). The resultant temperatures were then applied to the structural model again (starting from the point representing the end of bakeout, 25°C). This iterative process was repeated until the temperatures from the thermal analysis were consistent with the pressures and areas from the structural analysis.

The peak helix temperature occurs near the end of the rods for both the copper sleeve and GlidCop sleeve cases. Therefore, the component temperatures at the cross section at the end of the rods were chosen as the inputs to the structural runs. The inputs and results for the converged cases are given in Table 4. The derivation of the temperature inputs is described more fully in Section 3.0. The results show that a greater portion of the interface force is maintained when the GlidCop sleeve is used. This causes the contact area and pressure at the helix/rod interface to be much higher than in the copper sleeve case. In both cases, the asymptotic limit was used for the thermal interface coefficient. At the rod/sleeve interface, the contact area remained at the maximum value for the copper sleeve. However, the area for the GlidCop sleeve decreased slightly from the room temperature value. Although the rod/sleeve pressure is much higher with the GlidCop sleeve than with the copper sleeve, the interface coefficient is slightly lower.

TABLE 4

INPUTS FOR STRUCTURAL ANALYSIS (OPERATION)

Component	Temperature (°C)	
	Copper Sleeve	GlidCop Sleeve
Helix	192	189
Rod	161	168
Sleeve	152	153
Barrel	129	129

RESULTS OF STRUCTURAL ANALYSIS (OPERATION)

Quantity	Copper Sleeve	GlidCop Sleeve
Helix/rod area (in^2 /contact point)	3.2×10^{-5}	5.1×10^{-5}
Helix/rod pressure (ksi)	42	99
Helix/rod interface coefficient ($W/cm^2 - °C$)	50	50
Rod/sleeve area (in^2/in/rod)	5.0×10^{-3}	3.0×10^{-3}
Rod/sleeve pressure (ksi)	9	56
Rod/sleeve interface coefficient ($W/cm^2 - °C$)	50	45
Interface force (lbs/in/rod)	44	168

3.0 THERMAL ANALYSIS

A 3–D finite element model was used for the thermal analysis of the output circuit. This was necessary because of the asymmetry of the design and the importance of the axial component of heat transfer. The use of a 3–D model was practical because the thermal analysis did not require the same level of detail as the structural analysis. The thermal analysis was carried out for both the copper sleeve and GlidCop sleeve cases.

A cross section (top view) of the model is shown in Figure 7. The TWT is modeled from the collector face to a point approximately 2.4 inches from the helix termination. The model consists of 4278 nodes and 3724 elements. The thermal conductivities of the materials used in the analysis are shown in Table 5. The helix was modeled with thermal bars that were given an equivalent conductivity to account for the copper coating on the tungsten/rhenium wire. The conductivity of tungsten/rhenium was assumed to be the same as that of pure tungsten. The taper of the helix was approximated by using uniform pitches over increments about one half inch long. Plate elements were used to represent the diamond rods as if they were continuous. Since the rods are actually segmented, the conductivity in the axial direction was set to zero. Preliminary runs showed that this approach was reasonable because the use of the full value for the conductivity (a very optimistic assumption) only lowered the peak helix temperature by 5°C. The sleeve was modeled with a single layer of solid elements, each encompassing a 30-degree arc. Two layers of elements were used for the iron pole pieces, monel spacers, and samarium cobalt magnets. These elements also encompassed 30-degree arcs. An equivalent conductivity was used for the magnets because they are held in place by epoxy. The copper helix termination was modeled with plate elements while the Kovar collector face is a combination of plates and solids.

There are three copper heatsinks on the collector side of the waveguide and eight on the gun side. The heatsinks are brazed to the outer diameter of the pole pieces and were represented by thermal bars. The heatsink design considered in the analysis is shown in Figure 8. Preliminary runs showed that the use of eight additional heatsinks on the gun side would only lower the peak helix temperature by about 4°C. Therefore, this proposed design modification was deemed unnecessary.

The interfaces between nonbonded components were modeled with thermal interface conductance elements. One element was used at each helix/rod contact point. Since the rod/sleeve contact regions are continuous, elements were used at every coincident node pair. The determination of the contact areas and heat transfer coefficients for these interfaces was discussed in Section 2.3. The sleeve/barrel contact area was assumed to be 20 percent of the circumference and the interface coefficient was 8.0 $W/in^2-°C$. The interface elements were connected at the three lines of node pairs 60 degrees from the rods. This was expected to be

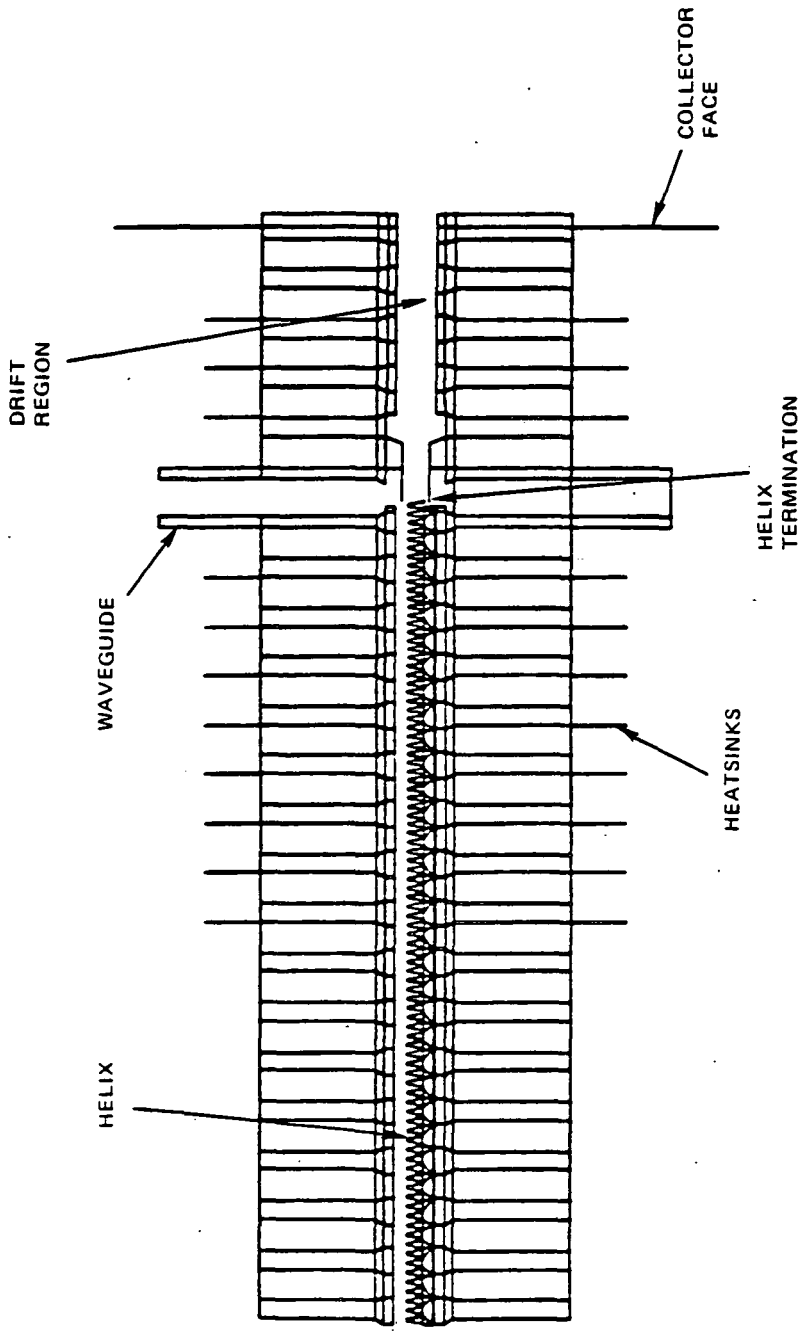

Figure 7 Cross section (top view) of the 3-D finite element model of the output circuit.

TABLE 5
THERMAL CONDUCTIVITIES

Material	Thermal Conductivity (W/in-°C)		
	25°C	200°C	400°C
97% Tungsten/3% Rhenium*	4.22	3.88	3.45
Equivalent value for helix	4.7	4.3	3.9
OFHC Copper	9.9	9.1	8.5
GlidCop AL-15	9.0	8.3	8.0
Diamond IIA	52.1	31.5	19.1
Electrolytic Iron	1.84	1.56	1.30
Monel 404	0.41	0.55	0.71
Samarium Cobalt	0.262	0.262	0.262
Epoxy	0.053	0.053	0.053
Equivalent value for magnet/epoxy			
(axial)	0.232	0.232	0.232
(radial and circumferential)	0.175	0.175	0.175
Kovar	0.42	0.48	0.56

*Conductivities for pure tungsten were used.

a conservative representation of this interface. The coefficient for the heatsink/baseplate interface was set at 8.0 W/in^2-°C. This value was used in the 918H analysis and is consistent with the 918H test results.

Although the specification for the mounting platform temperature is 50°C, this analysis was based on an 85°C temperature to account for possible future uses of this design. The boundary conditions were scaled from the 918H analysis and test results. The outer diameter of the collector face was fixed at 125°C. It is known that the results are not sensitive to this

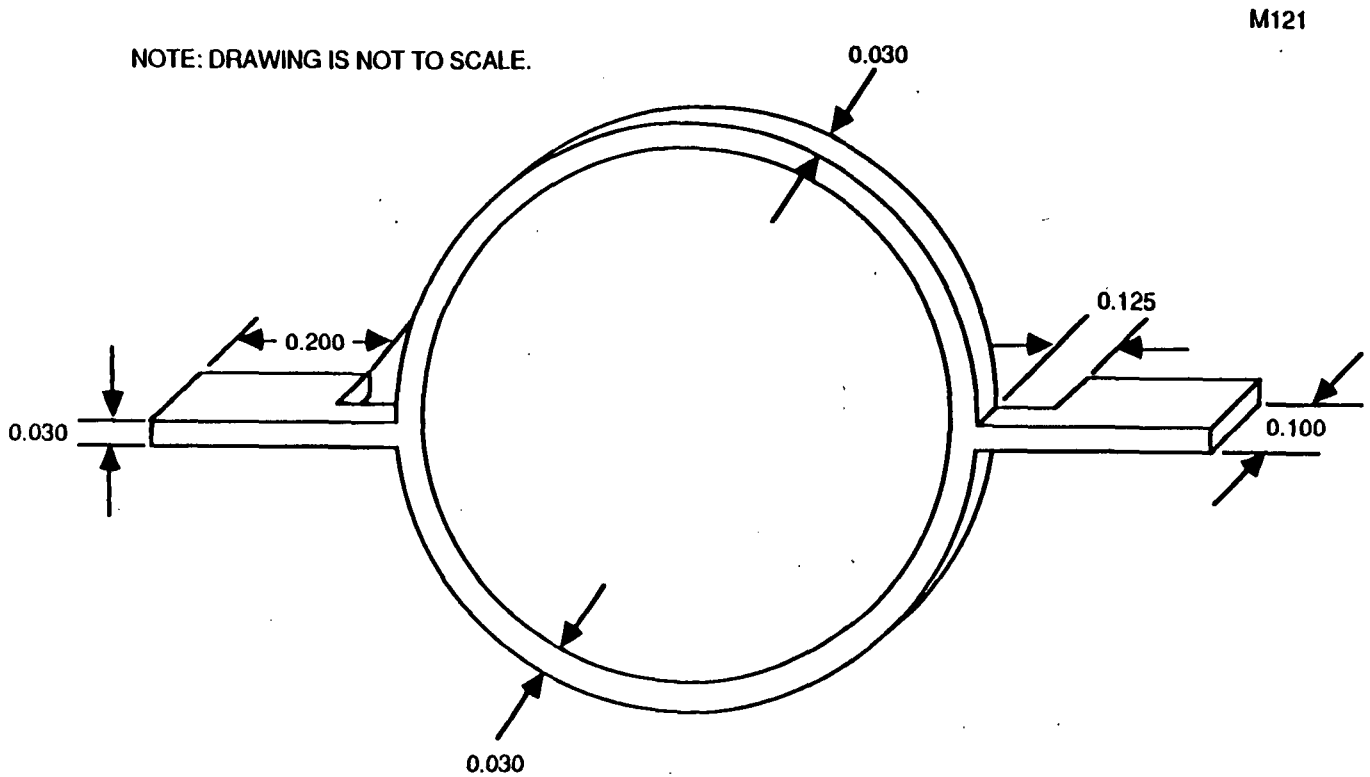

Figure 8 Heatsink design.

assumption because preliminary runs showed that a 10°C change in this value caused only a 2°C change in the peak helix temperature. The baseplate temperature at the heatsink interface was fixed at 100°C. The end of the model (gun side) was adiabatic.

The distribution of the power shown in Figure 9 indicates a total of 14.1 watts to be dissipated on the last inch of the helix. For this analysis, the distribution has been assumed to be uniform over each quarter inch with the power applied directly to each node of the helix. The drift region was assumed to intercept 2.5 watts distributed uniformly over its length. The power was applied to the nodes at the inner diameter of the barrel between the waveguide and the collector face. Finally, 2.5 watts were distributed uniformly over the area of the collector face up to a 0.75-inch diameter.

The results of the analysis of the copper sleeve case showed that the peak helix temperature was 194°C. This occurred just beyond the last helix/rod contact point at the end of the rods. The temperature distribution through the cross section at the end of the rods is shown in Figure 10. This illustrates the temperature drop from the helix to the inner diameter of the barrel. There is a 30°C drop across the helix/rod interface and an 8°C drop across the rod/sleeve interface. Due to the high thermal conductivity of diamond, there is only a 2°C drop between the inner and outer edges of the rod. The temperature drop between the inner and outer diameters of the copper sleeve is insignificant, but the drop at the sleeve/barrel interface is over 20°C. This conflicts with the circuit thermal test results, which show that the actual drop across this interface is very small. It is believed that the presence of the gold plating on the outer diameter of the sleeve may be responsible for the formation of a bond at this interface.* Therefore, the assumption used in the thermal analysis was overly conservative. If a more realistic assumption had been used, the predicted sleeve temperature would have been lower. This would have caused slightly higher helix/rod and rod/sleeve contact areas and pressures in the structural analysis and, consequently, lower temperature drops in the thermal analysis.

Table 6 shows the axial temperature distribution in the circuit by giving the temperatures at four cross sections. Structural runs for the operating condition were made using these four sets of temperatures. The resultant areas and pressures for the cross section at the end of the rods were reported in Section 2.3. The results for the other three cross sections were also quite similar.

The results of the GlidCop sleeve case showed that the peak helix temperature was 192°C. As in the copper sleeve case, this occurred just beyond the last helix/rod contact point. The temperature distribution through the cross section at the end of the rods is shown in Figure 11. The axial temperature distribution is shown in Table 7. The predicted temperatures

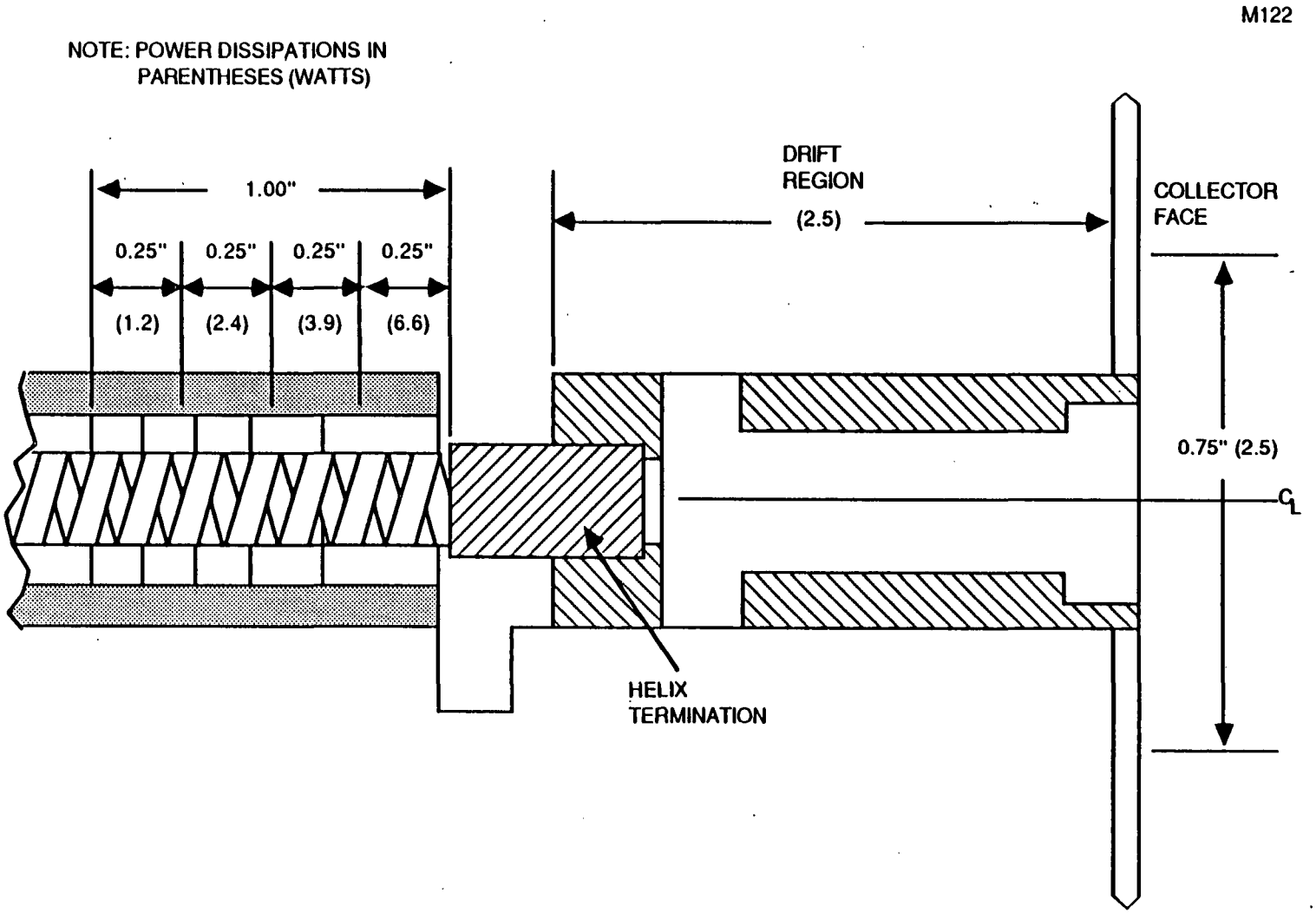

Figure 9 Power distribution for thermal analysis.

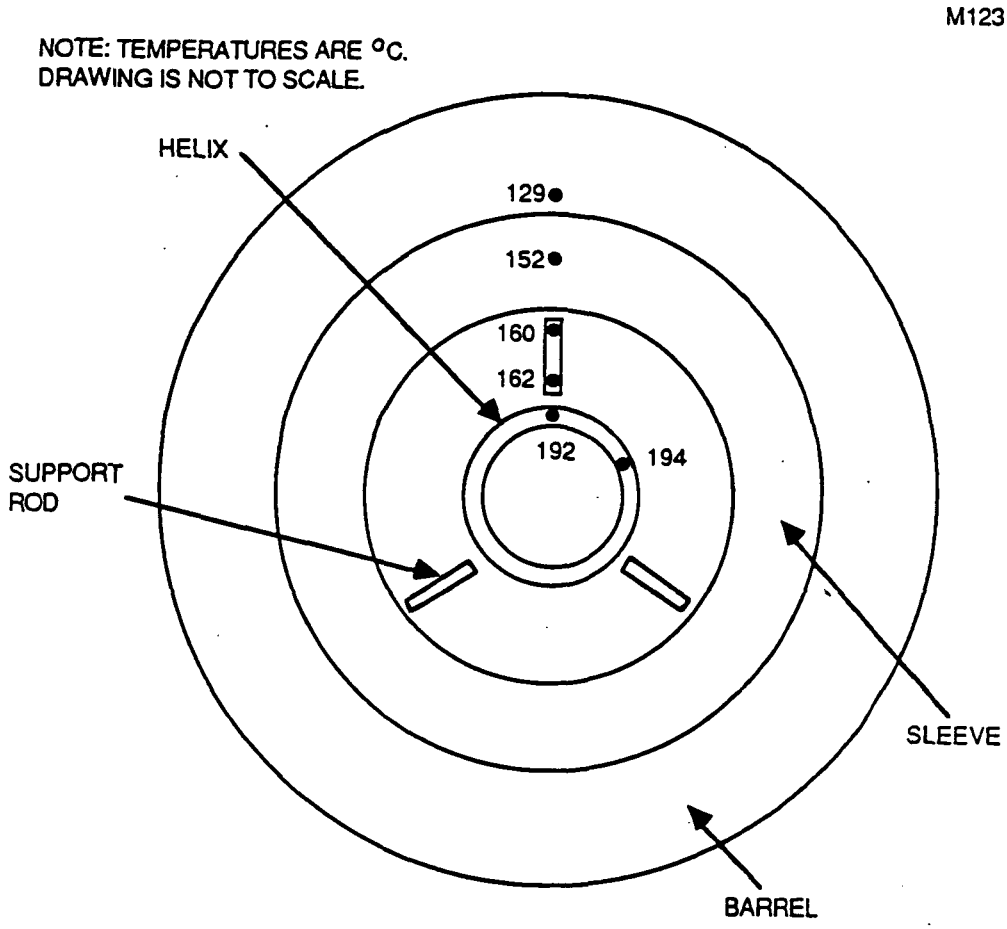

Figure 10 Temperature distribution through cross section at end of rods (copper sleeve case).

TABLE 6

TEMPERATURE DISTRIBUTION FOR COPPER SLEEVE CASE (°C)

Radial Location	Axial Location (inches from end of rods)			
	0.0	0.2	0.5	1.0
Helix	192	180	156	131
Rod, inner edge	162	157	146	131
Rod, outer edge	160	155	145	131
Sleeve, inner diameter	152	150	142	130
Sleeve, outer diameter	152	150	142	130
Barrel, inner diameter	129	129	127	122
Barrel, outer diameter	126	125	124	121

TABLE 7

TEMPERATURE DISTRIBUTION FOR GLIDCOP SLEEVE CASE (°C)

Radial Location	Axial Location (inches from end of rods)			
	0.0	0.2	0.5	1.0
Helix	189	178	155	131
Rod, inner edge	169	163	149	131
Rod, outer edge	167	161	148	131
Sleeve, inner diameter	153	151	143	130
Sleeve, outer diameter	153	151	143	130
Barrel, inner diameter	129	129	127	122
Barrel, outer diameter	126	125	124	121

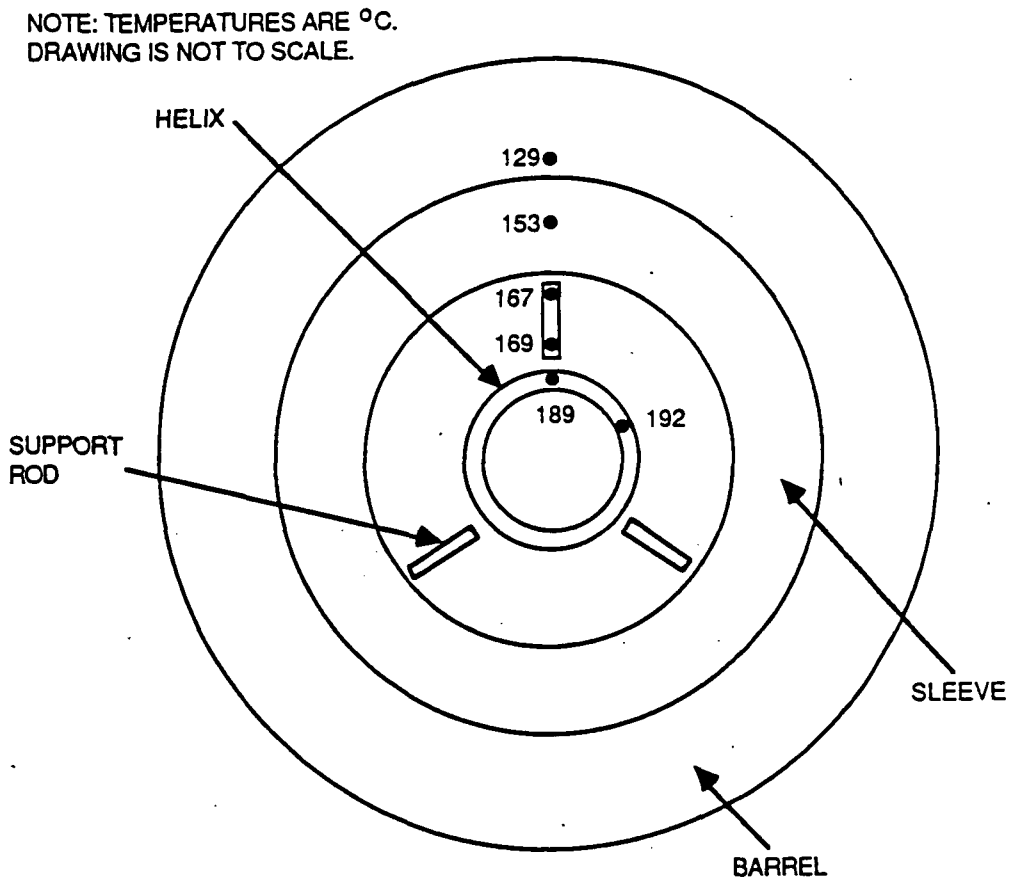

Figure 11 Temperature distribution through cross section at end of rods (GlidCop sleeve case).

for the GlidCop sleeve case are similar to those for the copper sleeve case except that the helix/rod temperature drop is lower and the rod/sleeve drop is higher. The helix/rod drop at the end of the rods is only 20°C because the higher interface force increased the contact area. The rod/sleeve drop is 14°C because the predicted area is smaller despite the higher force. As in the copper sleeve case, the contact areas and pressures predicted by the structural model were similar at the four different cross sections.

In both cases the predicted peak helix temperature is well below the design limit of 300°C. The temperatures in the magnets and epoxy are also important. Magnet temperatures above 200°C can lead to defocussing of the electron beam. The epoxy may begin to gradually degrade above 150°C. The predicted barrel temperatures are below 130°C, so these limits are satisfied.

4.0 LONG-TERM OPERATION

The 953H TWT must be able to perform for a long period of time without a degradation in performance. If the helix temperature were to rise above 300°C during operation, the probability of an observable change in electrical performance would increase rapidly. Such a temperature rise could be attributable to creep strain in the output circuit. Therefore, an estimate was made of the effect of creep on the thermal performance of the circuit after 100,000 hours (11.4 years) of operation. This was assumed to be the end-of-life condition. Both the copper sleeve and GlidCop sleeve cases were considered.

Creep is a continuous increase in deformation (strain) with time under a constant load (stress). Material creep rates are highly dependent upon temperature. Relaxation is a related phenomenon in which the load continuously decreases with time under a constant deformation. In many applications, both phenomena occur simultaneously and are referred to as "creep". In the output circuit, the compressive forces that hold the components together will gradually decrease during operation. Local deformation may also cause the contact areas at the critical interfaces to change.

A structural analysis for the long-term operating condition of a copper-sleeved circuit was performed. This analysis continued from the results of a preliminary analysis of the initial operating condition. The initial operating temperatures had been estimated as follows: helix, 180°C; rods, 130°C; sleeve, 120°C; barrel, 115°C. The applied temperatures remained constant throughout the analysis. Creep strain was allowed only in the copper sleeve and helix coating because the creep rates in the other materials would be insignificant at these temperatures.

Primary creep refers to the strain that occurs soon after the application of a load. Since the primary creep rate decreases rapidly, it is of most importance for short-term effects. Following primary creep, the secondary creep rate is essentially constant over a long period of time. Therefore, the secondary creep rate of copper was used in the analysis for the long-term operating condition. The secondary creep rates of copper and GlidCop are given in Table 8. The data from Jenkins and Digges[4] and Davis[5] are from uniaxial tension creep tests. The values for GlidCop were derived from uniaxial tension relaxation tests presented by SCM.[6]

In the finite element analysis, the multidimensional creep effects were extrapolated from the uniaxial test data in the same way as the plasticity effects. The test data near 120°C was used to develop the equation governing the creep strain in the copper sleeve:

$$\dot{\epsilon} = (4.0 \times 10^{-16}) \exp(-6000/T)\, \sigma^4$$

TABLE 8
SECONDARY CREEP STRAIN RATES

Material	Source	Temperature (°C)	Stress (ksi)	Creep Rate (in/in/hour)
Copper	Jenkins and Digges (Reference 4)	120	18	1.0×10^{-5}
		120	22	1.0×10^{-4}
		120	24	1.0×10^{-3}
		150	16	1.0×10^{-5}
		150	19	1.0×10^{-4}
		150	22	1.0×10^{-3}
Copper	Davis (Reference 5)	130	16.0	3.6×10^{-7}
		130	10.0	8.0×10^{-8}
		130	5.0	3.0×10^{-8}
		165	10.0	3.2×10^{-7}
		165	4.0	7.2×10^{-8}
		200	6.4	6.6×10^{-7}
		200	4.5	4.2×10^{-7}
		235	7.0	2.3×10^{-6}
		235	4.0	8.2×10^{-7}
GlidCop AL-15	SCM (Reference 6)	250	27	1.2×10^{-8}
		250	30	1.7×10^{-8}
		250	35	3.1×10^{-8}

where

$\dot{\epsilon}$ is the equivalent creep strain rate (in/in/hr)

T is the temperature (K)

σ is the stress (psi).

The equation for the copper helix coating was

$$\dot{\epsilon} = (9.6 \times 10^{-18}) \exp(-6000/T)\, \sigma^5$$

This equation was based on the data near 180°C. It also accounts for the use of the modified stress-strain curve in the analysis. The use of these equations imply that creep and relaxation are governed by a single, unified theory. Although this is not true, it is the best available approach.

The results for the preliminary initial operation analysis and the end-of-life condition are given in Table 9. These show that the contact pressures of the critical interfaces will decrease a great deal over the life of the TWT. The predicted helix/rod contact area increases due to localized creep before significant relaxation occurs. The predicted rod/sleeve contact area decreases due to relaxation.

The interface areas and force for the actual end-of-life condition were scaled from the final results for the initial operating condition by using ratios derived from the preliminary analytical results. This approach is reasonable since the final results for the initial operating condition are similar to the preliminary results. The scaled values for the end-of-life condition are shown in Table 9. The resultant helix/rod thermal interface coefficient is 14 $W/cm^2-°C$ and the rod/sleeve coefficient is 21 $W/cm^2-°C$.

TABLE 9
INTERFACE VALUES FOR END-OF-LIFE ESTIMATE
(COPPER SLEEVE)

Quantity	Preliminary Analysis		Final Analysis	
	Initial	End–of–Life	Initial	End–of–Life*
Helix/rod area (in^2/contact point)	3.3×10^{-5}	5.7×10^{-5}	3.2×10^{-5}	5.5×10^{-5}
Helix/rod pressure (ksi)	46	2.6	42	2.4
Helix/rod interface coefficient ($W/cm^2-°C$)	–	–	–	14
Rod/sleeve area (in^2/in/rod)	5.0×10^{-3}	4.2×10^{-3}	5.0×10^{-3}	4.2×10^{-3}
Rod/sleeve pressure (ksi)	10	1.2	9	1.0
Rod/sleeve interface coefficient ($W/cm^2-°C$)	–	–	–	21
Interface force (lbs/in/rod)	50	4.9	44	4.3

*Based on scaling of interface areas and force.

These contact areas and interface coefficients were used in the thermal model to determine the temperature distribution for the end-of-life condition. The results showed that the peak helix temperature was 220°C and occurred between the last two contact points at the end of the rods. This is only 26°C higher than the peak temperature in the initial operating condition and is well below the design limit of 300°C. The temperature distribution through the cross section at the end of the rods is shown in Figure 12. Table 10 shows the axial temperature distribution in the circuit. The temperatures of the magnets and epoxy were essentially the same as in the initial operating condition.

To estimate the end-of-life condition of the GlidCop sleeve circuit, several assumptions had to be made. Since the initial contact force will be high, it is expected that full contact at the helix/rod interface will be achieved. The contact force at the end-of-life was assumed to be about 50 percent higher than the copper sleeve case. It is possible, however, that the force

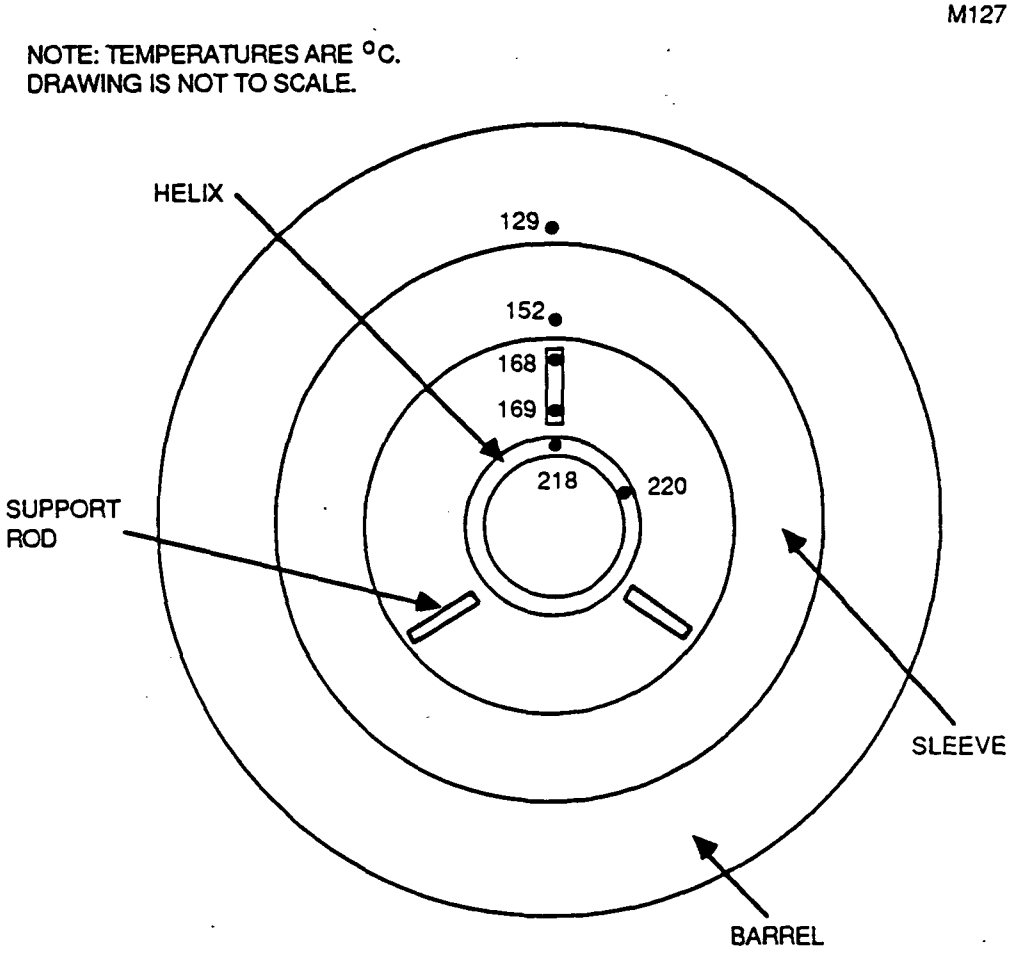

Figure 12 Temperature distribution through cross section at end of rods (copper sleeve case) for end-of-life condition.

TABLE 10
TEMPERATURE DISTRIBUTION FOR END-OF-LIFE WITH COPPER SLEEVE (°C)

Radial Location	Axial Location (inches from end of rods)			
	0.0	0.2	0.5	1.0
Helix	218	212	171	133
Rod, inner edge	169	166	151	131
Rod, outer edge	168	164	150	131
Sleeve, inner diameter	152	150	142	130
Sleeve, outer diameter	152	150	142	130
Barrel, inner diameter	129	129	127	122
Barrel, outer diameter	126	125	124	121

could be a great deal higher because of the creep resistance of GlidCop. The rod/sleeve contact area was assumed to be two-thirds of the initial area because of the reduction in force. The GlidCop/diamond interface coefficient is very uncertain. Scaling of the pressure axis for the copper/diamond empirical curve puts the estimated pressure below the available data. An approximation of 10 $W/cm^2-°C$ was used for the interface coefficient. The interface areas, pressures, coefficients, and force arising from these assumptions are given in Table 11.

These interface values were used in the thermal model and the results showed that the peak helix temperature was 255°C. This occurred approximately 0.07 inch from the end of the rods. Although this temperature is 63°C higher than the peak temperature in the initial operating condition, it is still below the design limit of 300°C. The temperature distribution through the cross section at the peak helix temperature location is shown in Figure 13. This shows how the helix temperature is driven by the large drop across the rod/sleeve interface. In light of the discussion in Section 2.2, the contact area assumed at this interface is probably quite conservative. If a larger area had been used, the peak helix temperature would be significantly lower. Table 12 shows the axial temperature distribution in the circuit. The temperatures of the magnets and epoxy were essentially the same as in the initial operating condition.

TABLE 11

INTERFACE VALUES FOR END-OF-LIFE CONDITION
(GLIDCOP SLEEVE)

Quantity	Value
Helix/rod area (in^2/contact point)	7.5×10^{-5}
Helix/rod pressure (ksi)	2.6
Helix/rod interface coefficient ($W/cm^2-°C$)	15
Rod/sleeve area (in^2 /in/rod)	2.0×10^{-3}
Rod/sleeve pressure (ksi)	3.2
Rod/sleeve interface coefficient ($W/cm^2-°C$)	10
Interface force (lbs/in/rod)	6.4

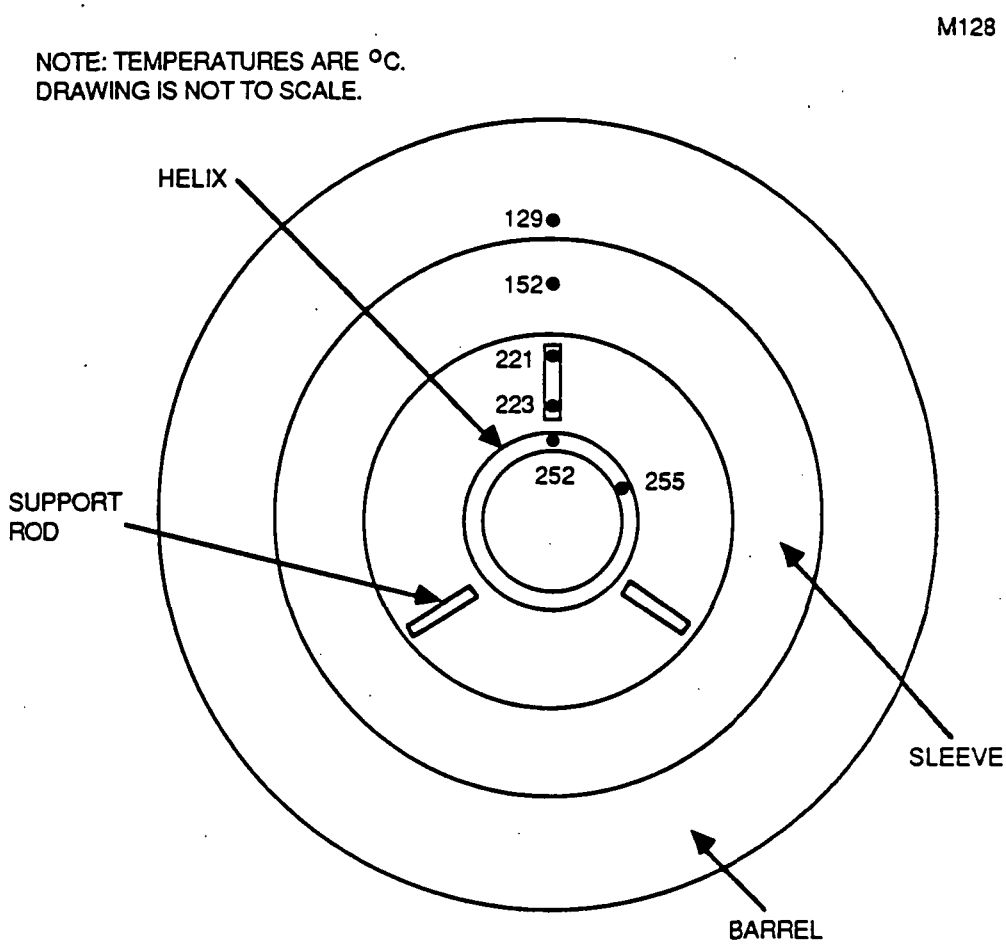

Figure 13 Temperature distribution through cross section at peak helix temperature (GlidCop sleeve case) for end-of-life condition.

TABLE 12

TEMPERATURE DISTRIBUTION FOR END-OF-LIFE
WITH GLIDCOP SLEEVE (°C)

Radial Location	Axial Location (inches from end of rods)			
	0.0	0.2	0.5	1.0
Helix	241	243	188	134
Rod, inner edge	216	215	174	134
Rod, outer edge	214	213	173	133
Sleeve, inner diameter	152	151	143	130
Sleeve, outer diameter	152	151	143	130
Barrel, inner diameter	129	129	127	122
Barrel, outer diameter	126	125	124	121

5.0 CONCLUSION

The combined structural and thermal analysis of the 953H output circuit has shown that it will be able to handle the required thermal loads. The predicted peak helix temperatures during the initial operating condition were 194°C for the copper sleeve design and 192°C for the GlidCop sleeve design. The estimates for the long-term operating condition predicted peaks of 220°C for the copper sleeve and 255°C for the GlidCop sleeve. Since these temperatures are below the design limit of 300°C, both configurations are considered to be satisfactory.

It should be noted that the purpose of the analysis was to judge both configurations by the design limit rather than providing a comparison between designs. Conservative assumptions were made throughout this analysis because the final results were to be compared to an absolute limit. The analytical approaches used in the bakeout analysis and the long-term operation estimates were much more conservative for the GlidCop sleeve design than the copper sleeve design. Due to this inequity, a direct comparison between the two sets of results could lead to misleading conclusions. It is likely that the actual temperatures for the GlidCop design will be considerably lower than predicted. In fact, it is possible that the temperatures could be lower than those for the copper sleeve design.

To improve the understanding of the GlidCop design, experiments should be conducted to determine the GlidCop/diamond thermal interface coefficient as a function of pressure. Extending the existing curves for the other interfaces into the low and high pressure regions would also be useful in future analyses. In addition, better definition of the other GlidCop properties would be helpful.

6.0 REFERENCES

1. P.C. Kohnke, ANSYS Theoretical Manual, Swanson Analysis Systems, Inc., March 1, 1986.
2. O. Sauseng, "Heat Transfer Data for Helix Circuit Materials," Hughes EDD Report, p. 19, August 1984.
3. Ibid., p. 23.
4. W.D. Jenkins and T.G. Digges, "Creep of Annealed and Cold-Drawn High Purity Copper," J. Research National Bureau of Standards, Vol. 47, 1951, p. 272–287.
5. E.A. Davis, "Creep and Relaxation of Oxygen-Free Copper," Trans. Am. Soc. Mech. Engrs. 65, [A]101 (1943).
6. SCM Metal Products, Vendor-supplied data, 1985.

NASA
National Aeronautics and Space Administration

Report Documentation Page

1. Report No.	2. Government Accession No.	3. Recipient's Catalog No.
NASA CR-187160		

4. Title and Subtitle	5. Report Date
Final Report for NAS3-24897 "High-Efficiency 20 GHz Traveling Wave Tube Development"	October 1991
	6. Performing Organization Code 96-31-23
7. Author(s) S. L. Aldana R. N. Tamashiro	8. Performing Organization Report No.
	10. Work Unit No. 650-60-22
9. Performing Organization Name and Address Hughes Aircraft Company, Electron Dynamics Division 3100 W. Lomita Blvd. Torrance, CA	11. Contract or Grant No. NAS3-24897
	13. Type of Report and Period Covered Contractor Report
12. Sponsoring Agency Name and Address National Aeronautics and Space Administration Washington, D.C. 20546-0001	14. Sponsoring Agency Code

15. Supplementary Notes

Project Manager, Kurt Shalkhauser
NASA Lewis Research Center
Cleveland, Ohio 44135

16. Abstract

A 75 Watt CW high efficiency helix TWT operating at 20 GHz was developed for satellite communication systems. The purpose behind this effort was to extend the performance capabilities of helix TWTs by utilizing recent technology developments.

The TWT described in this paper in a unique tube design because high overall efficiency is obtained with a low perveance beam. In the past, low perveance designs resulted in low beam efficiencies. However, due to recent breakthroughs in diamond rod technology and in collector electrode materials, high efficiencies can now be achieved with low perveance beams.

The advantage of a low perveance beam is a reduction in space charge within the beam which translates to more efficient collector operation. In addition, this design incorporates textured graphite electrodes which further enhance collector operation by suppressing backstreaming secondaries.

(Continued on back)

17. Key Words (Suggested by Author(s))	18. Distribution Statement
Traveling Wave Tube, Diamond Support Rods, Multistage Depressed Collectors, Graphite Electrodes, Tapered Helices	Unclassified - Unlimited Subject Category 32

19. Security Classif. (of this report)	20. Security Classif. (of this page)	21. No of pages	22. Price*
UNCLASSIFIED	UNCLASSIFIED	91	

*For sale by the National Technical Information Service, Springfield, Virginia 22161

16. Abstract (Continued)

The diamond supported helix circuit features low rf losses, high interaction impedance, good thermal handling capability and has been designed to compensate for the low perveance beam. The circuit incorporates five mil (0.005 in.) wide diamonds as the helix support rod material. A non-bonded non-brazed diamond rod fabrication technique has eliminated the losses previously encountered with brazed diamond/helix interfaces without sacrificing thermal handling requirements. In this application, the circuit cold loss is measured to be 0.3 dB/in at 20 GHz. In comparison, the cold loss for an identical circuit incorporating 0.020 in. wide BeO rods is 1.5 dB/in.

One more feature of the tube design that will be discussed is the utilization of a velocity taper in the output helix that achieves low signal distortion while maintaining high efficiency.

Three breadboard units were fabricated under this program. One unit demonstrated 100 watts RF output power, with excellent repeatability and no sign of degradation. The same TWT achieved 16.9 percent basic and 54.6 percent overall efficiency setting a new bench mark in TWT technology for K-band devices. In contrast, 12 percent basic and 48 percent overall was the best K-band TWT efficiency achieved in the past.

The structural, thermal and electrical properties of diamonds are becoming increasingly attractive with higher TWT operating frequencies. The techniques used to fabricate the present circuit are compatible with TWT electrical design requirements up to 60 GHz.